Improving Attitude Determination and Control of Resource-constrained CubeSats Using Unscented Kalman Filtering

by

Weston Alan Navarro Marlow

B.F.A. Graphic Design
New Mexico State University (2005)

B.S. Aerospace Engineering
New Mexico State University (2011)

Submitted to the Department of Aeronautics and Astronautics
in partial fulfillment of the requirements for the degree of

Master of Science in Aeronautics and Astronautics

at the

MASSACHUSETTS INSTITUTE OF TECHNOLOGY

June 2016

Author ..... Signature redacted
Department of Aeronautics and Astronautics
May 19, 2016

Certified by ..... Signature redacted
Kerri L. Cahoy
Assistant Professor of Aeronautics and Astronautics
Thesis Supervisor

Accepted by ..... Signature redacted
Paulo C. Lozano
Associate Professor of Aeronautics and Astronautics
Chair, Graduate Program Committee

Improving Attitude Determination and Control of Resource-constrained CubeSats Using Unscented Kalman Filtering

by

Weston Alan Navarro Marlow

Submitted to the Department of Aeronautics and Astronautics
on May 19, 2016, in partial fulfillment of the
requirements for the degree of
Master of Science in Aeronautics and Astronautics

Abstract

CubeSats are a specific subset of nanosatellites, and their common form factor and canisterized deployers have made it possible to undertake higher risk, lower cost missions that can supplement the current generation of large, monolithic, expensive satellites. Our objective in this thesis is to improve attitude estimation on CubeSats using Unscented Kalman filters. CubeSats have evolved from their relatively low complexity and low computational power beginnings. This progression motivates us to revisit attitude determination estimation approaches commonly used for CubeSats, and to implement an alternative Kalman filtering method.

Our goal is to improve the current state of the art in attitude estimation on previous MIT Space Systems Laboratory CubeSats by at least two orders of magnitude from about 1-5° attitude knowledge error down to 0.05° or better. This improvement benefits applications that require precise pointing, such as imaging and active tracking of specific targets, laser communications, and coordinated activity and observations among multiple CubeSats.

We were able to achieve better than our pointing error goal of 0.05°, and found that the proposed Unscented Kalman filter performed significantly better at high angular rate estimation than the Extended Kalman filter (already implemented on some CubeSats). The quaternion estimates were converted to Euler angles to improve ease of interpretation. For the majority of the missions, the mean total Euler angle estimation error improvement ranged from 83% - 98% with error variance decreased by as much as 98%. One implementation had more than a two order of magnitude improvement, to achieve 0.01° mean error, better than the desired pointing accuracy. We present a detailed assessment of these estimation errors, along with changes in quaternion error that accompany varying the unscented filter parameters.

Thesis Supervisor: Kerri L. Cahoy
Title: Assistant Professor of Aeronautics and Astronautics

Acknowledgments

This material is based upon work supported by the United States Air Force under Air Force Contract No. FA8721-05-C-0002 and/or FA8702-15-D-0001. Any opinions, findings and conclusions or recommendations expressed in this material are those of the author(s) and do not necessarily reflect the views of the United States Air Force.

I would like to thank my thesis advisor, Professor Kerri Cahoy for believing in me and being supportive through my growth and pain as a new graduate student. Your guidance and encouragement have allowed me to push the limits of what I thought I was capable of achieving.

I would like to attempt to capture the gratitude I feel towards my family. Although simple words on a page cannot do this justice, I want to say thank you to my amazing parents for always believing in me and being so supportive through all of my endeavors, no matter how difficult or seemingly foolish along the way. I simply couldn't have done this without you. And a warm thank you to my sister. You are someone I will always look up to. Thank you for your strength and for putting up with your annoying little brother all these years.

Two roads diverged in a wood, and I—
I took the one less traveled by,
And that has made all the difference.
— Robert Frost, from *The Road Not Taken*

Contents

List of Figures

List of Tables

Key Nomenclature

ADCS Attitude Determination and Control System

COTS Commercial Off the Shelf

CSS Coarse Sun Sensor

EHS Earth Horizon Sensor

EKF Extended Kalman Filter

GPS Global Positioning System

HIL Hardware In the Loop

IGRF International Geomagnetic Reference Field

IMU Inertial Measurement Unit

ISS International Space Station

KF Kalman Filter

LEO Low Earth Orbit

MEMS microelectromechanical systems

MicroMAS Microsized Microwave Atmospheric Satellite

MIT Massachusetts Institute of Technology

MIT/LL Massachusetts Institute of Technology Lincoln Laboratory

MTM Magnetometer

MTQ Magnetorquer

NASA National Aeronautics and Space Administration

RSS root sum square

RWA Reaction Wheel Assembly

SSA Space Situational Awareness

SSL Space Systems Laboratory

SSO Sun-synchronous Orbit

STAR Lab Space, Telecommunications, Astronomy, and Radiation Laboratory

SWaP size weight and power

U unit

UKF Unscented Kalman Filter

Chapter 1

An Introduction to CubeSats and Motivation for Studying Their Applications to Lasercomm and SSA

1.1 Introduction and Overview of CubeSats

1.1.1 Nanosatellites and the CubeSat

Earth-sensing and communication satellites are usually large, high-value systems that are difficult to replace in the event of launch failures or on-orbit failures. The inherent uniqueness of these systems drives high development costs to account for high reliability, redundancy of critical components, and extensive verification and validation cycles. These large satellites are fairly rigid in their utility and mission scope. To potentially help ease the burdens of cost and inflexible mission scope, there exist relatively new satellite designs and mission architectures that have a different approach. Since 1999[16], the CubeSat category of spacecraft has emerged and has gained widespread adoption as a science and technology demonstration platform. Initially popular at universities and academic research institutions, CubeSats are gaining traction in the commercial and government sectors. In the category of small spacecraft (less than 500 kg[33]), there are further designations of micro, nano and pico

satellites.

We focus on nanosatellites, small satellites that are less than 10 kg[33]. The reason for such limited mass is not only because they are small, but also because they are in canisterized dispensers that are low-risk to the host launch vehicle and primary payload(s). Within the nanosatellite category, spacecraft can vary in size and shape. We focus on a specific form factor of satellite, called a "CubeSat". There is a CubeSat specification document developed by the California Polytechnic State University beginning sixteen years ago, and it defines a CubeSat unit (U) as the volume of a cube with 10 cm on a side and a mass of 1.33 kg per U.[16] A single unit, or 1U, CubeSat is shown in Figure 1-1.

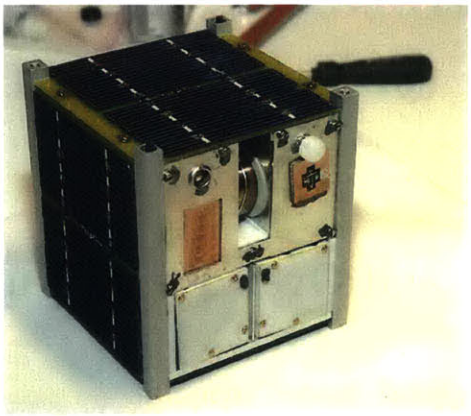

Figure 1-1: The Norwegian satellite, nCube2, is an example of a 1U CubeSat. Source: `https://en.wikipedia.org/wiki/NCube_(satellite)`. Accessed March 30, 2016.

The CubeSat Design Specification (CDS) standardized nanosatellite bus sizes[16]. This standardization has resulted in an increase in the availability of Commercial Off the Shelf (COTS) components built for easy integration into CubeSat platforms. The CubeSat units can be stacked or combined in a modular fashion, and can be packed into single or multiple CubeSat deployers and manifest as auxiliary payloads on larger commercial or National Aeronautics and Space Administration (NASA) launches to Low Earth Orbit (LEO) and beyond. The COTS components now available for these satellites include miniaturized electronics and microelectromechanical systems (MEMS) that have been designed for tech-demonstration-grade space applications. Such components are available for purchase at lower cost compared with

highly specialized, high-performance, one-of-a-kind spacecraft components for much larger systems, albeit with a reduction in overall performance.

As CubeSat capabilities continue to improve, for example in processing power and pointing control, mission applications are transitioning from academic and scientific proof-of-concept missions[14, 74] to missions with valuable operational objectives[23, 29, 51]. This trend can be seen clearly in Figure 1-2[64] with the increase in military, civil government, and commercial CubeSat missions. The ability for large numbers of CubeSats to be fielded at relatively low cost, and the resulting improvement in geospatial and temporal coverage, has spurred commercial entities like Planet Labs[51] as well as the United States military investment into nanosatellite development[11]. As the industry adapts to these new platforms, so must the traditional subsystems that comprise spacecraft.

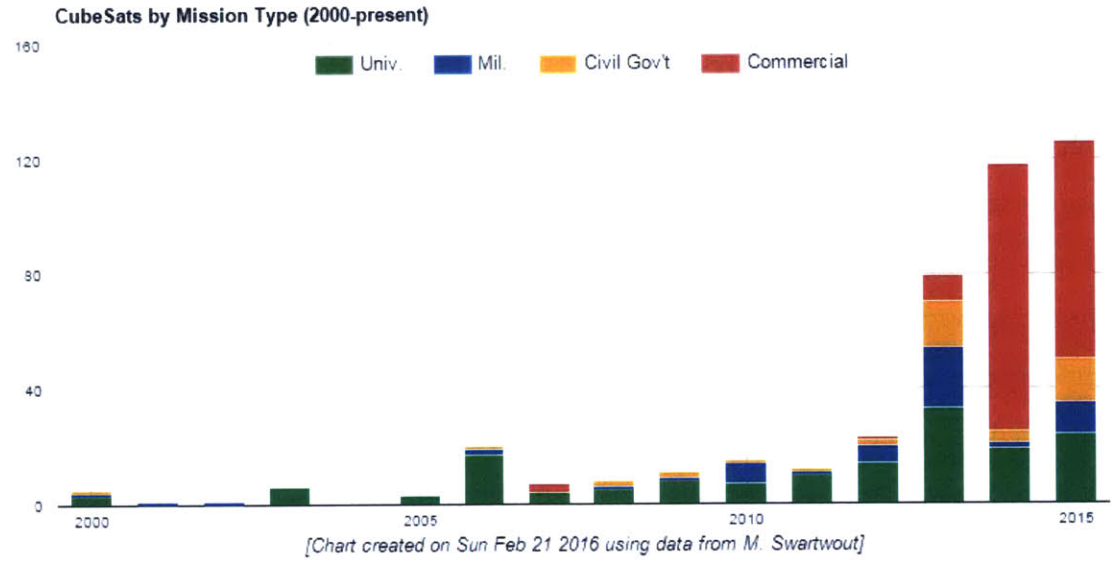

Figure 1-2: Plot of CubeSat launches since 2000. Data is from the Saint Louis University CubeSat Database. The data show a marked recent increase in utility of CubeSats for missions beyond university uses.[64]

The role of the Attitude Determination and Control System (ADCS) has become increasingly critical for CubeSat mission success with the increasing complexity of missions. With CubeSats pushing into sub-degree pointing accuracy, the development of relatively high-performance hardware for CubeSat attitude sensing and control is a major need and is being addressed by several commercial entities. We describe

developments in sensors and actuators for CubeSats in detail in Sections 1.1.2 and 1.1.3. The other side of CubeSat attitude estimation and control is on software development.

We investigate the increases in pointing performance that can be gained by improving the attitude estimation techniques currently used for CubeSats [48, 74]. In Section 1.1.4 we also provide background on the current approach for modeling the spacecraft environment and disturbances, as this provides relevant detail about the parameters and performance metrics that we use in our models and mission simulations. In Chapter 2, we review the literature in CubeSat attitude estimation to determine the current state-of-the-art and discuss the importance of using advanced filtering techniques to help bridge this gap and improve CubeSat attitude estimation performance.

1.1.2 CubeSat Actuators

The selection of attitude control components is considered during early design phases for missions with the need for pointing control. Just as budgets for power, mass, and volume are considered during early design phases and throughout the mission life cycle, pointing budgets are critical to ensure designs meet performance requirements. Pointing requirements are usually derived from the mission objectives, often from "payload" requirements, and they drive the design or selection of control actuators and sensors. Unlike large spacecraft, most current CubeSats do not have on-board propulsion for trajectory changes or attitude control. This is due to the lack of volume and power available to enable a propulsion system and the low maturity level of propulsion technologies available for CubeSats.

This means that attitude control for these systems is typically done with either magnetorquers (MTQ) (also known as magnetic torque rods) or with miniaturized reaction wheels and MTQs. Due to the volume constraints on CubeSats, these actuators are typically non-redundant, meaning that a CubeSat with a full set of attitude control actuators has a set of three orthogonally-mounted reaction wheel assemblies and three orthogonally-mounted magnetorquers (one of each actuator for each axis).

A COTS use philosophy has redefined the role of the ADCS engineer for many CubeSat missions. These tightly-constrained programs devote some of their important resources to Hardware In the Loop (HIL) testing and software development (discussed further in Chapter 3) rather than RWA and MTQ design, development, and rigorous testing, as these tasks are taken on by the actuator vendors. It is worth noting that acceptance and performance testing of hardware is still a critical step that should be taken on by the ADCS subsystem engineers[49].

RWA Miniaturized reaction wheels have been developed for CubeSats and are commercially available. A Reaction Wheel Assembly is a fairly simple mechanism. It is a cylindrical rotor of high density metal (typically stainless steel or tungsten) that is commanded to spin over a range of speeds in both positive and negative directions. The wheels are nominally biased at some non-zero speed [72] and can be commanded to several thousand rotations per minute (RPM)[12, 34, 61] to exchange momentum from the spacecraft body to the wheels from external force build-up, or to provide torque for attitude maneuvering. Reaction wheels are becoming commonly used mechanisms on CubeSats, since a full set can provide stabilization about all three body axes.

Reaction wheels are often critical actuators for more complex mission profiles, especially in the case of 3-axis stabilized CubeSats [48, 49]. Reaction wheels do not change the overall momentum of the system; they are merely momentum exchange devices. Momentum budgets should be included in the design of an ADCS subsystem that contains RWAs. An example momentum budget is shown in Table 1.1. The wheels must be capable of storing the momentum needed for maneuvering, pointing, and momentum build-up from external disturbance torques. In LEO, these torques come from atmospheric drag, solar radiation pressure, gravitational harmonics, and residual magnetic dipoles in the spacecraft interacting with the Earth's magnetic field. These disturbances impart small (see Figure 1-4) periodic or secular accelerations that build excess momentum over time and must be accounted for in the momentum budget. The only way for systems without propulsion to remove this excess momentum

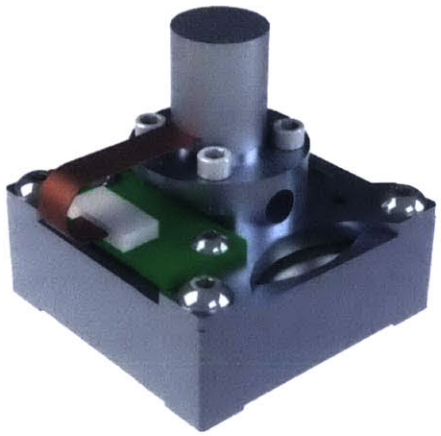

Figure 1-3: Example miniaturized reaction wheel for CubeSats. An example of a miniaturized reaction wheel from Maryland Aerospace, Inc. is shown. 3-axis stabilized CubeSats often have one RWA for the X, Y, and Z axes. Source: `http://d6110363.ozt807.onezerotech.com/wp-content/uploads/2015/08/MAI_Single_Axis_Assembly_Brochure-20150827.pdf`, accessed March 30, 2016.

from the satellite is by interacting with the external environment. In this work, 'momentum dumping' is done using actuation from magnetorquers. The RWA may also have the requirement to provide adequate torque to execute maneuvers in a timely manner or at a specified rate. We discuss the state-of-the-art for CubeSat slewing in Section 2.2.4.

Magnetorquer As the spacecraft encounters external torques from environmental disturbances, the control system must continually counter momentum build-up by storing this in the reaction wheels. This is only useful for a finite amount of storage. When the wheels reach maximum or near-maximum speed and can no longer deliver added torque or store additional momentum, this is referred to as 'wheel saturation'. The magnetorquers on spacecraft can be used to dump this excess momentum, since interaction with the local magnetic field will allow for this exchange and reduce the load on the wheels. This operation must be running continuously during normal ADCS operations[48, 73].

Magnetic interaction with the local field is also critical for detumbling CubeSats

Example Momentum Budget		
Mode	Min [mNs]	Max [mNs]
Environmental	0.04	0.08
LVLH	0.15	0.18
Coarse Pointing	0.1	0.11
Fine Pointing	0.015	0.017
Comm Pass	0.25	0.37
Slew	0.77	0.89
Total	**1.325**	**1.647**

Table 1.1: Example CubeSat momentum budget. The reaction wheels and magnetorquers for such a CubeSat mission would need to be able to store and dispose of these momenta.

after deployment. CubeSat MTQs enable the spacecraft to slow rotation rates by performing a simple attitude control law called B-dot. Papers have been written on the matter[63], but the law simply uses electromagnets to oppose the spacecraft rotation rate. This control law has been used by a previous MIT flight program[48, 49].

Capabilities of the MAI-400 and BCT XACT			
Component	Capability	Value	Units
MAI-400 RWA	Momentum Storage	9.35	mNms
MAI-400 RWA	Maximum Torque	0.64	mNm
MAI-400 MTQ	Magnetic Dipole	0.11	Am^2
BCT XACT RWA	Momentum Storage	15	mNms
BCT XACT RWA	Maximum Torque	0.6	mNm
BCT XACT MTQ	Magnetic Dipole	unlisted	Am^2

Table 1.2: Sample CubeSat actuator capabilities. Source for MAI values: `http://maiaero.com/products/s/mai-400/`. Accessed March 31, 2016. Source for BCT values: `http://bluecanyontech.com/wp-content/uploads/2016/01/XACT-Data-Sheet_2.0.pdf`. Accessed March 31, 2016. For clarification, the maximum torque numbers listed for the BCT XACT reaction wheels were found through secondary public sources[9].

Some sample reaction wheel and magnetic torque rod momentum and dipole properties are shown in Table 1.2. These are for two ADCS all-in-one units from established companies Maryland Aerospace, Inc. in Crofton, MD and Blue Canyon Technologies in Boulder, CO[12, 34].

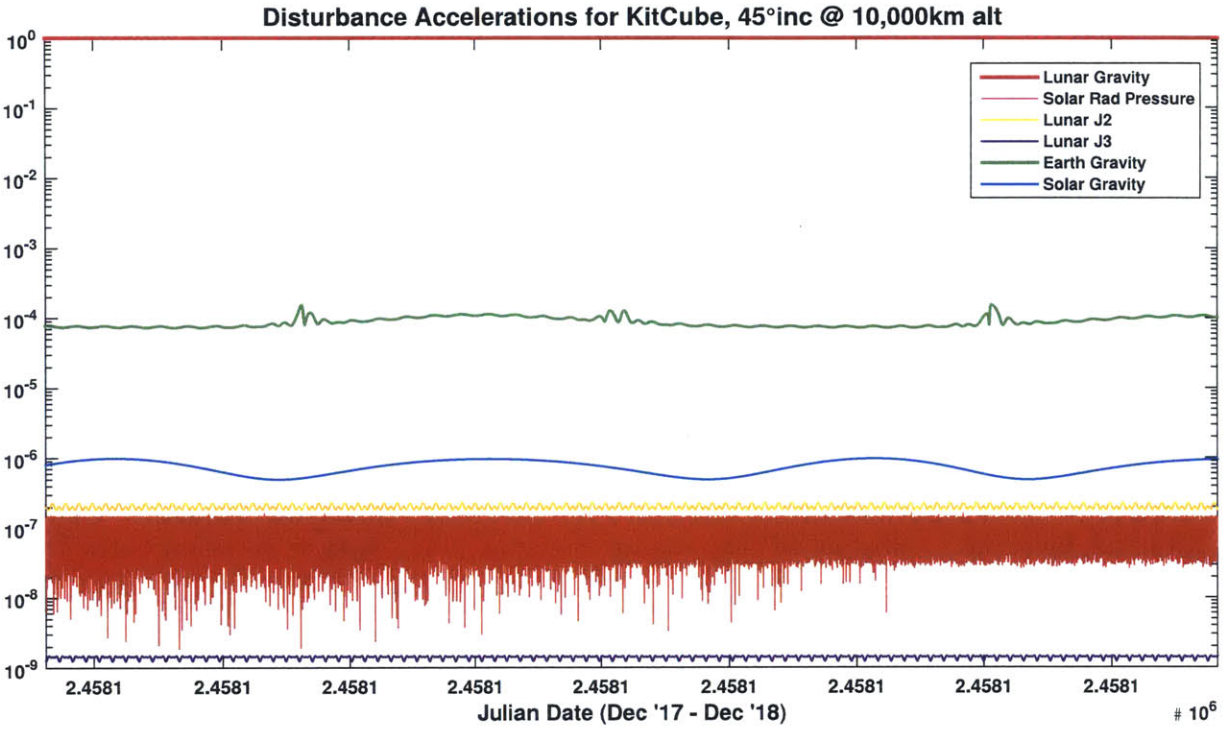

Figure 1-4: Example disturbance torque magnitudes for a 6U lunar CubeSat mission (KitCube), normalized to lunar gravity in a 10,000 km circular lunar orbit. *Image credit: W. Marlow*

1.1.3 CubeSat Sensors

Several attitude sensors are commercially available in miniature form that will fit on CubeSats. These range from micro-sized magnetometers that are simple, surface-mount circuit board components, to more specialized infrared devices using thermopiles that can measure the Earth's limb relative to cold space, and even miniaturized star trackers for high-accuracy attitude determination. Whether measuring Earth's magnetic field, the apparent horizon, or the relative sun vector, the objective is to use these sensors to deliver vector solutions to the ADCS software for fusion into estimation algorithms for determining the satellite's relative pointing and rotation rates. We briefly introduce Earth horizon sensors, sun sensors, magnetometers, inertial measuring devices, star trackers, and global positioning system receivers (for absolute relative position and velocity determination).

Earth Horizon Sensor (EHS) We use the static variety of these sensors for the mission simulations, as opposed to a scanning EHS head. The static sensors use a set of infrared thermopile detectors to sense Earth's limb via the relatively warm infrared radiation that the Earth's limb emits, in contrast to the cold background of space. This measurement is used to build an estimate of the location and direction of Earth's limb and using that, provide a nadir vector estimate. Our spacecraft model uses two EHS sensor heads mounted orthogonally to provide two Earth limb vectors, such that the EHS algorithms infer the nadir vector by completing the vector triad. These sensors can provide better than 0.5° of attitude knowledge when properly calibrated[39].

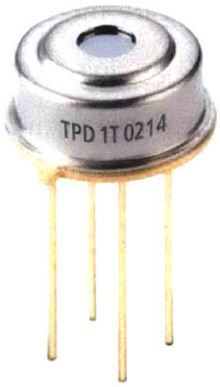

Figure 1-5: Example thermopile found in an Earth horizon sensor. Source: `http://www.excelitas.com/downloads/TPD%201T%200224%20TPD%201T%200524%20TPD%201T%200624%20-%20General-Purpose%20Thermopile.pdf`. Accessed March 1, 2016.

Coarse Sun Sensor (CSS) These sensors are the simplest attitude sensing devices used in the models. While there exist more complex sun sensing devices that provide higher accuracy (down to 0.1 degree) and digital output[42], CubeSats equipped with more sensitive devices like the EHS heads and star trackers use CSS for only coarse pointing knowledge (down to 1 degree, see Table 2.2). The sensors are small, analog photodiode detectors sensitive to the visible spectrum that output an expected analog voltage based on the intensity of the sunlight incident upon the detector; they are essentially small solar cells. The CSSs are modeled as mounted to their respective body panel, with a sensor acting as reference for each face of the cube (six in total).

Figure 1-6: Example of a Silonex sun sensor. Source: `https://octopart.com/slsd-71n800-silonex-8060378`. Accessed May 15, 2016.

The photodiodes used in the spacecraft models that are part of this work have flight heritage. They are SLSD-71N800 analog photodiode sensors manufactured by Advanced Photonix[58]. The sun sensors have been tested for temperature-dependent biases during thermal vacuum testing of the MicroMAS program. This characterization data has been included in the model for completeness, along with included sensitivity to some of Earth's albedo.

3-Axis Magnetometer (MTM) Most CubeSat missions have operated in LEO. As previously mentioned, this is a useful source for attitude control actuation with MTQs below geostationary altitudes (35,786 km). The Earth's magnetic field can be measured using on-board sensors to give a coarse sense of what the instantaneous field direction and intensity are. Using these measurements in combination with the on-board magnetic field model, we can infer satellite attitude motion. The spacecraft models used in our pointing simulations use PNI Sensor Corporation's RM3000 3-axis geomagnetic sensor suite magnetometers. These MEMS sensors consists of a magnetic sensor for the X, Y, and Z axes. Aside from providing knowledge about spacecraft motion, the measurements of the magnetic field around the spacecraft can be compared with the International Geomagnetic Reference Field (IGRF) model to help determine an estimate of the spacecraft's position in orbit.

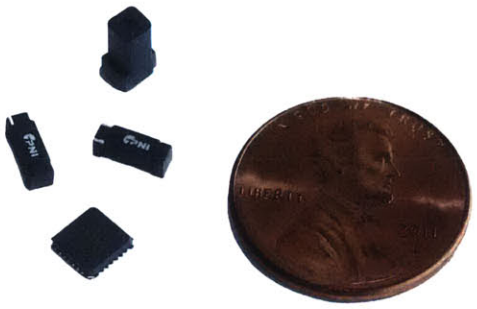

Figure 1-7: Three-axis miniaturized MEMS magnetometer. The sensor suite shown is the PNI Sensor Corporation RM3000 surface mount magnetometer set. source: `http://www.willow.co.uk/html/components/com_virtuemart/shop_image/product/Heading/images/RMSS_07-30-12.jpg`. Accessed March 30, 2016.

6-Degree of Freedom Inertial Measurement Unit (IMU) Most IMU packages contain a 3-axis MEMS gyroscope and MEMS accelerometer. Each spacecraft is also modeled with an IMU to determine rotation rates. The sensors are also capable of measuring accelerations, but will not be utilized in this manner for the simulated missions since this iteration of the work does not include propulsion and associated thrust accelerations. We use the Analog Devices ADIS 16334 tri-axis digital MEMS gyroscope and accelerometer in our attitude estimation simulation since we have previous experience with these components. The ADIS 16334 consists of three orthogonal MEMS gyroscopes and three orthogonal linear accelerometers. Well-known complications with IMUs is they tend to drift with time and are susceptible to purges of the launch vehicle fairing with Helium or Nitrogen. This drift is also modeled and accounted for in the estimation software, as will be discussed in Chapter 3.

On-board Global Positioning System (GPS) Frequent updates in spacecraft position and velocity will be accomplished with GPS positioning, navigation, and time (PNT). GPS receivers are only reliable below the orbital altitude of the GPS satellites being used. The use of the full the GPS signal (beyond civilian-only band) for precision navigation must be unlocked or authorized. These absolute PNT updates are used to mitigate the on-board navigation drift, which can induce attitude errors.

Star Trackers Miniaturized star trackers are a critical enabling technology for high precision pointing missions on CubeSats. These imaging devices use algorithms to match stars in the field of view with known star catalogs to give attitude solutions that can be accurate down to tens of arcseconds or better[12, 60]. As such high-accuracy sensors, they have the ability to replace sensors like the EHS for fine attitude sensing. Our spacecraft models do not incorporate the use of star trackers.

1.1.4 Developing an ADCS Simulation for CubeSats

One challenge for the ADCS engineer is in fusing the input from the many different sources of attitude and position information. These sources are inherently noisy and will produce attitude solutions or vectors that may be in conflict with those from other sensors.

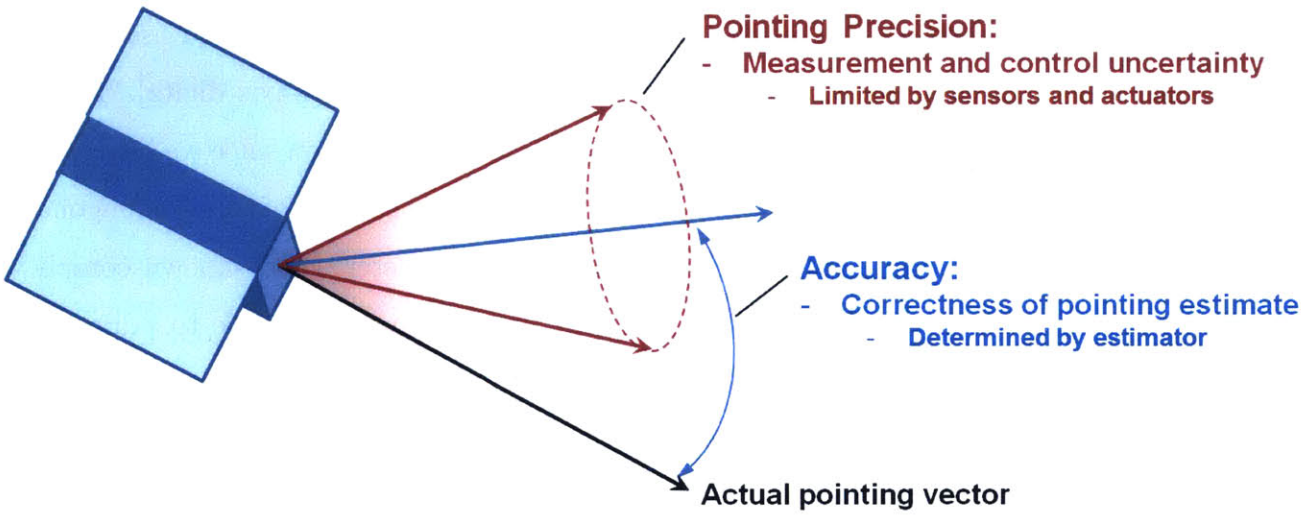

Figure 1-8: Pointing precision and accuracy. The figure illustrates the different sources of precision and accuracy errors in attitude estimation and control (greatly exaggerated). The example satellite shown is a 3U bus with two double-deployed solar panels in lighter blue. *Image credit: W. Marlow.*

The satellites that have been modeled are 3U and 6U buses. The 3U size comprises the majority of the CubeSats that have been launched to-date[64] and 6Us are on the

horizon for launch. Our 3U bus models house all of the sensors described above except the star trackers, and we assume roughly 1.5U for payload reserve. Reaction wheels and magnetorquers are used for actuation with enough remaining volume and power support a payload for technology demonstration or operation. Our CubeSat spacecraft models contain the following attitude control sensors and actuators:

Sensors and Actuators in the Spacecraft Models, 3-σ values		
Component	Description	Capability
Reaction Wheels[12, 34, 61]	Precision pointing control	0.003°
Earth Horizon Sensors[34]	Coarse attitude sensing	0.5°
Sun Sensors[48, 49]	Coarse attitude sensing	1°
MEMS Magnetometers[23]	Coarse attitude sensing	1-5°
Magnetic Torque Rods	Coarse pointing, momentum control	5°
MEMS Inertial Meas. Unit	Body rates and accelerations	–

Table 1.3: CubeSat sensors and actuators used in the simulations presented in this work.

Many attitude sensors and actuators have been miniaturized and some vendors have built these into all-in-one packages that contain most of the functionality listed above. A photo of an all-in-one ADCS package is shown in Figure 1-9 that takes up about 1/2U of volume.

Future work will include two star trackers mounted orthogonally. This allows for even finer attitude determination by minimizing the ambiguity of around-boresight measurements.

Disturbance Force Models: Models in MATLAB code exist for the disturbance forces that a typical LEO mission can expect to encounter. The different models used in this work, along with their governing equations, consist of:

- Gravity gradient torque code[71], and standard gravity gradient equation[72]

$$\mathbf{T}_g = \frac{3\mu}{R_0^3}\mathbf{u}_n \times (\mathbf{I} \cdot \mathbf{u}_n) \tag{1.1}$$

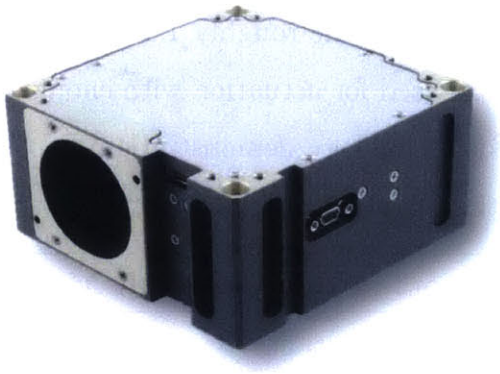

Figure 1-9: Blue Canyon Technologies XACT all-in-one ADCS package[12]. This 1/2 U system is one of several all-in-one solutions available from commercial vendors. It contains a star tracker, three RWA, three MTQ, and several sensors. Source: `http://bluecanyontech.com/wp-content/uploads/bfi_thumb/BCT_product-004-m7fww25vzhvqkas6ie40mzqrarxys6hpqp0430p7cs.jpg`. Accessed May 15, 2016.

  - $\mathbf{T}_\mathrm{g}$ is the resultant gravity torque (N·m)
  - μ is Earth's gravitational parameter (3.986×10^{14} $\mathrm{m}^3/\mathrm{s}^2$)
  - R_0 is distance to center of Earth (m)
  - $\mathbf{I}$ is the spacecraft moment of inertia matrix (3×3 matrix, kg·m^2)
  - $\mathbf{u}_\mathrm{n}$ is the unit vector towards nadir (unitless)

- Atmospheric density model[66], and the standard drag torque equation[72]

$$\mathbf{T}_\mathrm{d} = \frac{1}{2}\rho V^2 C_\mathrm{d} A(\mathbf{u}_\mathrm{v} \times \mathbf{s}_\mathrm{cp}) \tag{1.2}$$

  - $\mathbf{T}_\mathrm{d}$ is the resultant drag torque (N·m)
  - ρ is the atmospheric density at altitude (kg/m^3)
  - V is the spacecraft velocity (m/s)
  - C_d is the coefficient of draft for satellites (unitless, typically 2-2.5 [18, 72])
  - A is the surface area normal to the velocity vector (m^2)

- $\mathbf{u}_v$ is the unit vector along the spacecraft velocity (unitless)
- $\mathbf{s}_{cp}$ is the vector offset from spacecraft center of gravity to the acting center of pressure for the drag force (m)

- International Geomagnetic Reference Field (IGRF) for magnetic field strength and direction [41]

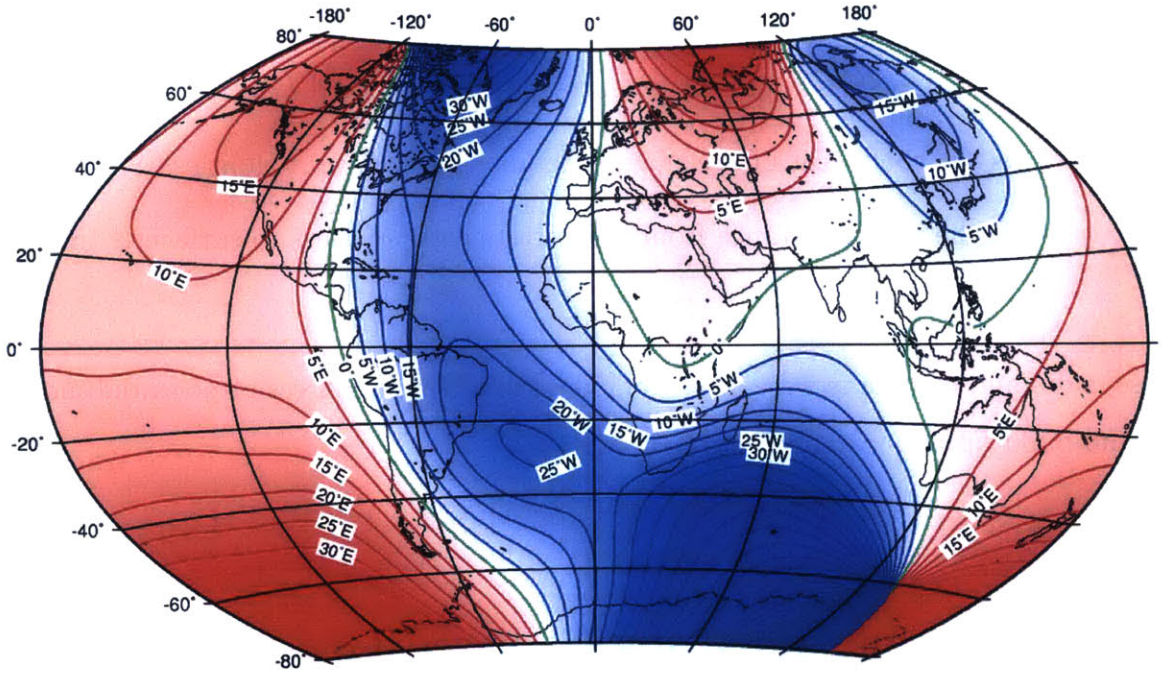

Figure 1-10: Earth's magnetic field depiction. Source: `http://www.geomag.bgs.ac.uk/research/modelling/IGRF.html`. Accessed May 15, 2016.

$$\mathbf{T}_m = \mathbf{m} \times \mathbf{B} \tag{1.3}$$

- $\mathbf{T}_m$ is the resultant magnetically-induced torque (N·m)
- $\mathbf{m}$ is the spacecraft magnetic moment (A·m^2)
- $\mathbf{B}$ is the local magnetic flux density (Wb·m)

- Solar radiation pressure model code[71], and the associated equation[72]

$$\mathbf{T}_s = K_s(\mathbf{u}_s \cdot \mathbf{u}_n)A\left[\mathbf{u}_s(\alpha + r_d) + \mathbf{u}_n\left\{2r_s + \frac{2}{3}r_d\right\}\right] \times \mathbf{s}_c \tag{1.4}$$

- $\mathbf{T}_s$ is the resultant solar radiation torque (N·m)
- K_s is the solar pressure constant at Earth (4.644×10^{-6} N/m^2)
- $\mathbf{u}_s$ is the unit vector towards the Sun (unitless)
- $\mathbf{u}_n$ is the unit vector perpendicular to the area (unitless)
- A is the area receiving solar radiation (m^2)
- α is the coefficient of absorptivity for surface A (unitless)
- r_d is the coefficient of diffuse reflectance for surface A (unitless)
- r_s is the coefficient of specular reflectance for surface A (unitless)
- $\mathbf{s}_c$ is the vector distance from spacecraft center of mass to surface A (m)

These codes and equations were used to model the different sources of potential momentum build up in our analysis.

1.2 Motivations for CubeSat-based Low-cost Space-based Imaging and Lasercomm

1.2.1 The Case for CubeSats

Here we consider several examples of advanced payloads that require advanced attitude control on CubeSats.

Weather Sensing We first look at an example application of weather sensing satellites. Typical state-of-the-art for weather sensing satellite payloads are still large sensors requiring high power for operation. The Advanced Technology Microwave Sounder (ATMS) developed by NASA Goddard and built by Northrup Grumman Electronic Systems[15] is a reduced-size atmospheric sounder for advanced weather

sensing. The payload is housed on GOES-15 (Geostationary Operational Environmental Satellite), pictured in Figure 1-11. This payload represents a volume reduction from the previous SOA for atmospheric sounding (the Advanced Microwave Sounding Unit) by as much as three-fold. Even with large size weight and power (SWaP) savings, the ATMS is still 70 cm × 40 cm × 60 cm, requires 110 W and has a mass of 85 kg. A payload this size represents the SWaP of several whole CubeSats.

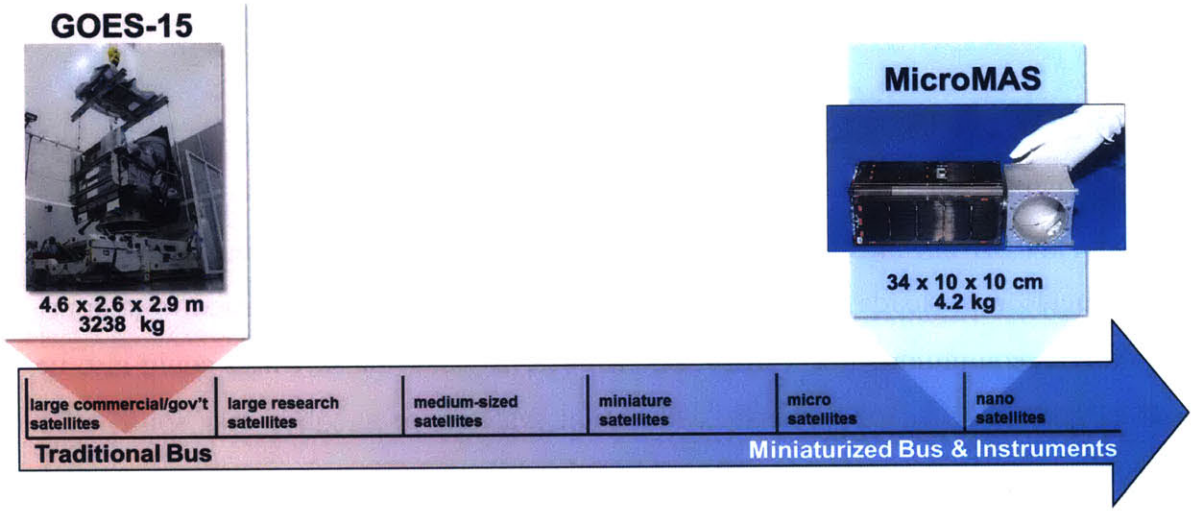

Figure 1-11: Miniaturization trends of instruments and satellite buses. An image of the GOES-15 weather satellite, which houses the ATMS state-of-the-art microwave sounder is shown on the left in contrast to the MicroMAS weather sensing CubeSat, which also has a microwave sounder payload. GOES image source: `https://en.wikipedia.org/wiki/GOES_15#/media/File:GOES-P.jpg`. Accessed December 7, 2015. MicroMAS image source: `https://directory.eoportal.org/web/eoportal/satellite-missions/m/micromas-1`. Accessed December 7, 2015.

Massachusetts Institute of Technology Lincoln Laboratory (MIT/LL) has developed miniaturized microwave sounders for use in 3U CubeSats like the Microsized Microwave Atmospheric Satellite (MicroMAS)[74] for deployment in future CubeSat constellations that can enable fast revisit times for weather sensing, seen at the right side of Figure 1-11. Payloads like those on MicroMAS drive pointing accuracy requirements for these SWaP-constrained systems and present a challenge for the ADCS designer. MicroMAS was deployed from the International Space Station (ISS) in early 2015 and was designed to achieve about 1° of pointing accuracy[49].

The design and fabrication of weather sensing CubeSats is one area of work cur-

rently being done at the Massachusetts Institute of Technology (MIT) Space, Telecommunications, Astronomy, and Radiation Laboratory (STAR Lab) but another is the design and development of free-space optical communication (hereby referred to as *optical comm* or *lasercomm*) payloads for use on CubeSats[29]. Though the discussion of optical comm can warrant entire theses and books[20, 28], the author will give a brief overview of optical comm for the purposes of demonstrating the impacts on CubeSat ADCS design.

CubeSat Optical Communication Enabling optical comm on CubeSats is a desirable capability for these systems, as it would allow for high data rate transmission. Satellite programs in the MIT STAR Lab are actively developing laser communication payloads for CubeSats. Spacecraft crosslinks can be used to support a networked communications constellation. Laser payloads on satellites could also be used as ground-based photometric calbriation systems, or as guide star sources for ground-based adaptive optics systems [10, 35].

Given the very high gains (narrow beamwidths) required for lasercomm, three sigma pointing requirements are typically designed to be ten times smaller than the beamwidth diameter[20]. The receive power for optical communication is directly proportional to the photon flux at the received aperture[72]. This requirement is levied since the flux intensity drops off as a function of the beam spreading (such as point spread functions or Gaussian beam divergence). This means that satellite-to-satellite pointing or tracking of an optical receive ground station becomes challenging, needing pointing accuracies down to only tens of arcseconds [29]. NASA has demonstrated the use of laser communication at lunar distances on the Lunar Laser Communication Demonstration (LLCD) and the Optical Payload for Lasercomm Science (OPALS). Smaller systems like AeroCube-Optical Communication and Sensor Demonstration (OCSD) have set out to prove the capacity for CubeSats to enable lasercomm[23].

Space Situational Awareness (SSA) SSA is another example application where CubeSats may be valuable. With Earth orbits becoming increasingly con-

gested and space debris becoming a larger problem, the use of LEO to LEO imaging with CubeSats can be of benefit to the SSA community. CubeSats designed for LEO imaging can potentially be used to help increase the fidelity of the space debris catalog. High relative orbital speeds, as discussed previously with optical comm cross links, pose a challenge in this type of mission as well. These high relative speeds means the CubeSats must also be able to track a fast-moving object (greater than 1 degree per second slew rates, depending on orbital configurations) and maintain pointing accuracy during these fast slews. In order to avoid adding to the space debris problem, CubeSats launched from the ISS are useful platforms since their high surface area to mass ratio (resulting in low ballistic coefficient) means most missions deployed from the ISS will de-orbit within only a few months.

Higher pointing performance on CubeSats with advanced attitude estimation and filtering techniques is relevant for several applications. In order to address the pointing requirements of such missions, we perform ADCS simulations of representative 3U and 6U CubeSats to compare current approaches in attitude estimation algorithms with the more advanced techniques that have not yet been implemented on CubeSats, such as the unscented Kalman filter and several of its variations.

The organization of this thesis is as follows:

Chapter Two introduces the reader to filtering and estimation techniques used in satellite ADCS development, provides a review of literature on CubeSat attitude estimation and control, and describes the research gap. **Chapter Three** describes the approach taken to model three orbits each (ISS-orbit, 400 km sun-synchronous orbit, and an 800 km LEO orbit) for the 3U and 6U architectures framed in Chapter 1. Concept of operations for the two satellite configurations and the orbits are described. The simulations include models of: attitude sensors, attitude control actuators, main imaging sensor, environmental models, and platform rigid-body disturbances. **Chapter Four** describes the analyses performed with the models in Chapter 3 including a discussion of the results of our analyses. **Chapter Five** summarizes findings, discusses limitations of the current approach, and proposes future methods for improving the simulations and addressing limitations.

Chapter 2

Literature Review and Motivation

2.1 Overview

In this chapter, we discuss (i) high slew capability (ii) fine pointing and (iii) state of the art hardware and software techniques as they apply to CubeSats. This discussion will motivate the case for advanced attitude filtering. Following that, we describe the different filtering techniques that are currently used for CubeSat missions and propose using new or different techniques that could improve pointing accuracy.

2.1.1 A Brief Control System Overview

For context, the attitude of a craft is the orientation of its local coordinate frame system (typically a *body frame* axis triad is assigned to a system) with respect to some other reference frame (note we describe only three-axis attitude determination, rather than others like *single-axis attitude determination*[71]). For orbiting spacecraft, the body frame is often taken as the Earth-centered inertial frame, or ECI.[71] A simple diagram of the three-body attitude problem is shown in Figure 2-2. Here we can see that, without a clear method of description, there exists ambiguity between the orientations of the two different right-handed triads. The XYZ frame and uvw frame satisfy the constraints

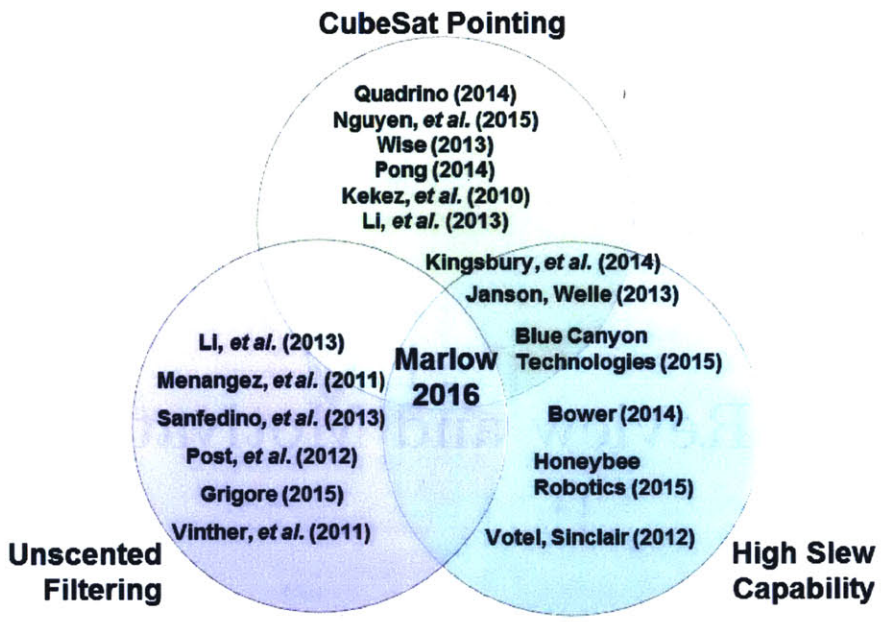

Figure 2-1: Venn diagram of relevant literature and main thrusts of research. *Image credit: W. Marlow.*

$$\hat{\mathbf{X}} \times \hat{\mathbf{Y}} = \hat{\mathbf{Z}} \tag{2.1}$$

and

$$\hat{\mathbf{u}} \times \hat{\mathbf{v}} = \hat{\mathbf{w}} \tag{2.2}$$

If we take the *uvw* frame to be representative of a spacecraft body coordinate frame (the spacecraft here is a point, O, at the origin of this triad), then the ADCS engineer is concerned with determining the relative orientation of the UVW spacecraft and how to control it.

There are a variety of ways to represent the attitude of a spacecraft. A partial list of alternatives is shown in Table 2.1.[56, 71] Beginning with the most basic of attitude representations, we look at the direction cosine matrix, or DCM, to eventually make our way to the quaternion method of attitude representation. The DCM is an intuitive matrix representation of the transformation between any two arbitrary axes (with one being chosen as a fixed axis and the other a rotating frame). The nine components

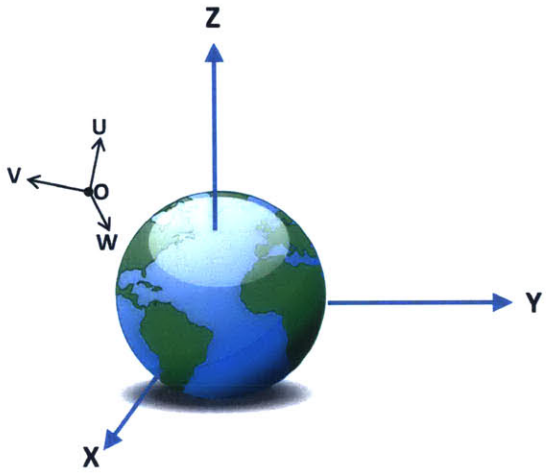

Figure 2-2: Simple diagram showing an ECI frame X,Y,Z and a satellite frame U,V,W. The frame X,Y,Z would typically be inertially fixed rather than earth-centered earth-fixed. *Image credit: W. Marlow.*

of the matrix relate the unit vectors of the rotating frame to one of the fixed frame axes by the cosine of their respective inner angles. For instance, the cosine of the angles between $\hat{\mathbf{u}}$ and the individual $\hat{\mathbf{X}}, \hat{\mathbf{Y}}, \hat{\mathbf{Z}}$ unit vectors, respectively, make up the first row of $[\mathbf{A_{3x3}}]$. Therefore, the fully populated DCM is

$$[\mathbf{A_{3x3}}] \equiv \begin{vmatrix} \cos\theta_{uX} & \cos\theta_{uY} & \cos\theta_{uZ} \\ \cos\theta_{vX} & \cos\theta_{vY} & \cos\theta_{vZ} \\ \cos\theta_{wX} & \cos\theta_{wY} & \cos\theta_{wZ} \end{vmatrix} \tag{2.3}$$

where θ_{mN} denotes the angle between unit vector m and non-rotating axis N.[56, 71] $[\mathbf{A_{3x3}}]$ also satisfies the constraint[71]

$$[\mathbf{A_{3x3}}][\mathbf{A_{3x3}}]^T = \mathbf{1} \tag{2.4}$$

Working with full three-axis transformations using only DCMs can become a cumbersome task given the number of redundant elements. It can be seen from Equations 2.5 to 2.9 that the quaternion method is without singularities, which makes it attractive for the ADCS engineer. Therefore, the typical standard for on-board attitude calculations is the quaternion.[71] This thesis work is concerned with attitude estima-

tion and filtering of quaternions (also known as Euler parameters). The quaternion method, though more abstract than an equivalent DCM, is related to the DCM by the simple constraints[56]

$$q_0 = \pm\frac{1}{2}\sqrt{A_{11} + A_{22} + A_{33} + 1} \tag{2.5}$$

$$q_1 = \frac{A_{23} - A_{32}}{4q_0} \tag{2.6}$$

$$q_2 = \frac{A_{31} - A_{13}}{4q_0} \tag{2.7}$$

$$q_3 = \frac{A_{12} - A_{21}}{4q_0} \tag{2.8}$$

and must satisfy

$$||\mathbf{q}|| = \sqrt{q_0^2 + q_1^2 + q_2^2 + q_3^2} \equiv 1. \tag{2.9}$$

A much more in-depth derivation and analysis of the different attitude representations is beyond the scope of this work, but can be found in the references by H. Schaub and J. Junkins (2009), and E. Wertz (1978).

Method	**Notation**	**Advantages**	**Disadvantages**
Euler angles	ϕ, θ, ψ	Non-redundant, intuitive	Trigonometric functions required, singularities, no easy successive rotations
Direction Cosine Matrix (DCM)	$\mathbf{[A_{3x3}]}$	No singularities or trig functions	Highly redundant
Euler Axis and Euler Angle	$\hat{\mathbf{e}}$, $\mathbf{\Phi}$	Intuitive representation	One redundant parameter, undefined at sin(Φ)=0, trig functions needed
Quaternion (Euler parameters)	$\langle \mathbf{q_0 q_1 q_2 q_3} \rangle$	No singularities, no trig functions, easy successive rotations	Redundant parameter, non-intuitive
Gibbs vector, or Classical Rodriguez vector	$\mathbf{g}$	Non-redundant, no trig functions, easy successive rotations	Infinite for 180° rotations

Table 2.1: Different three-axis attitude representation conventions[56, 71]. This list is not exhaustive.

Figure 2-3 shows a typical feedback control system block diagram for a satellite equipped with the sensors and actuators described in Chapter 1. Here, the blue shaded blocks for noise and estimation are the regions in the control system that this work aims to make contributions to. In the diagram, a desired attitude quaternion is regarded as the input to the control system. This attitude is one that is typically decided by mission operations or payload requirements, such as those in the MicroMAS mission which required the satellite to maintain local vertical local horizontal (LVLH) pointing [73]. This desired attitude is compared to the current best estimate of the spacecraft's attitude and the error is calculated and fed into the control algorithms that utilize the error to make the appropriate actuation for correction; this is typical "feedback control".

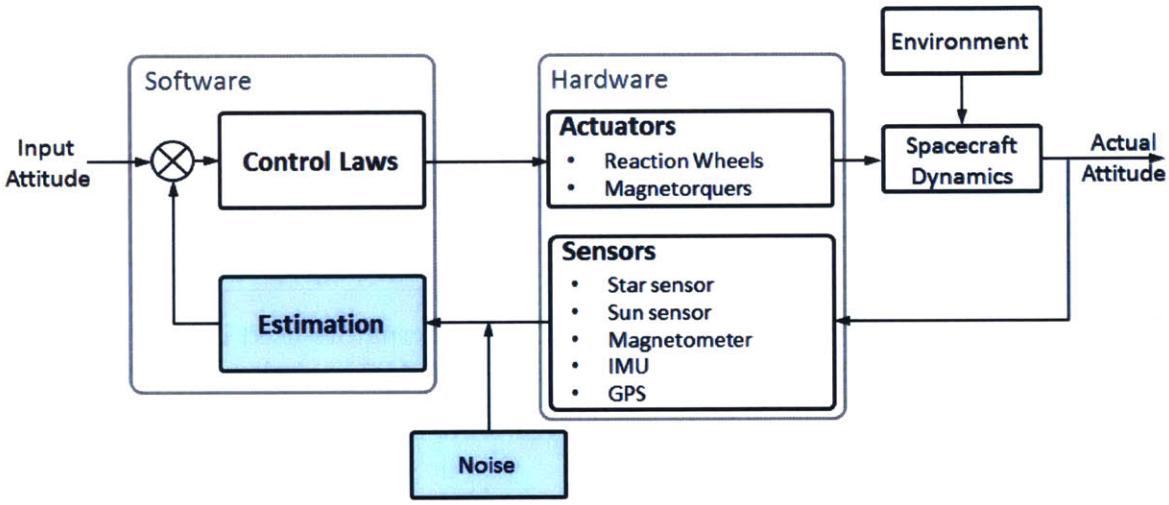

Figure 2-3: CubeSat control system block diagram. Noise and Estimation blocks are highlighted as the focus of this work. *Image credit: W. Marlow*

2.2 Current State of the Art

We present a brief market analysis of CubeSat attitude sensing and control hardware. we consider those components available to entities like universities that are developing CubeSats for concept demonstration of science payloads rather than ADCS hardware demonstrations. we then assess advanced ADCS software that has been developed in the past several years specifically for CubeSats.

2.2.1 CubeSat ADCS Hardware Roundup

Table 2.2 shows the results of our 2015-2016 COTS market analysis of the current state of the art for the CubeSat sensors and actuators. This is a non-exhaustive list of the many sensors and actuators that have flight heritage.[34, 58, 60, 61] The sensors and actuators that are used in the spacecraft simulations for this work include components from Maryland Aerospace, Inc., Sinclair Interplanetary, and Blue Canyon Technologies. Further details on each of the components in terms of specific hardware models used in the simulations can be found earlier, in Chapter 1.

State of the Art Summary of Proposed Sensors and Actuators, 3-σ values		
Component	Description	Capability
Star Trackers[26]	Precision attitude sensing	0.0003°
Reaction Wheels[12, 34, 61]	Precision pointing control	0.003°
Earth Horizon Sensors[34]	Coarse attitude sensing	0.5°
Sun Sensors[48, 49]	Coarse attitude sensing	1°
MEMS Magnetometers[23]	Coarse attitude sensing	1-5°
Magnetic Torque Rods	Coarse pointing, momentum control	5°
Propulsion	Growing trend, still limited use	–
MEMS Inertial Meas. Unit	Body rates and accelerations	–
GPS Receiver	Orbit determination	–

Table 2.2: COTS state of the art CubeSat sensors and actuators used in the simulations presented in this work and for proposed future simulation work.

2.2.2 Advanced Filtering Techniques on CubeSats

Having discussed the hardware that is used as the reference for our spacecraft models, we now turn our focus to CubeSat hardware, but the focus of this work is on the development of advanced filtering techniques for these missions. Our goal is to use existing attitude sensing hardware that is available commercially as input to construct representative models to test estimation algorithms that will increase mission utility and flexibility. Our approach involves sensor filtering and sensor fusion.

The recent commercial availability of 'CubeSat kits'[1] and increased access to space for CubeSats have been a boon for the space industry as a whole, as higher risk

[1]http://www.cubesatkit.com/ accessed April 6, 2016.

missions can be taken on with low-cost buses and at a much faster development cycles. However, the miniaturization and development of inexpensive MEMS ADCS components has usually come at the expense of sensor accuracy, precision, reliability, and noise characteristics.

All electronic devices have inherent noise characteristics that cannot be avoided. Even with larger, more precise, and more costly sensors, these noise parameters must be accounted for with the use of different filtering techniques. Since the nature of noise is nondeterministic (*i.e.* white noise or Gaussian noise), we must use the tools available for filtering satellite attitude motion.

2.2.3 CubeSat Attitude Control

CubeSat missions have flown with passive attitude control in the past, but as these technologies have matured, we see an increasing number of systems using active attitude control. Some of the earliest CubeSats flew without attitude control and only relied on attitude knowledge for operations. The next step in advancement relied on passive attitude control via gravity gradients, aerodynamic stabilization, or magnetic control with permanent magnets. Table 2.3 has a listing of several early CubeSats and their respective attitude determination and control capabilities. Passive control like aerodynamic stabilization and magnets are most effective at low LEO altitudes, since both the atmospheric density and magnetic field strength decrease exponentially as the altitude increases. An example satellite that partially utilized passive attitude control was the Naval Research Laboratory CubeSat Experiment-1 (QbX-1) that employed a 'Space Dart' solar panel configuration, as can be seen in Figure 2-4. At low enough LEO altitudes, below 500 km[50], the atmospheric density supports aerodynamic stabilization like that seen on a shuttlecock. This supplemented the reaction wheels and magnetic torquers for QbX-1.

Though simpler in design, these passive methods are not without risk. An unfortunate side effect of two CubeSats with permanent magnet control was the on-orbit conjunction of the MCubed and Hiscock Radiation Belt Explorer satellites. This was found to be caused by the mutual attraction of their permanent magnet systems after

Mission	Launch	ADCS Method	Hardware
CUTE-1[7]	2003	Attitude Determination	Gyroscopes, Accelerometers, Sun Sensor
CanX-1[70]	2003	3-Axis Active Control	MTM, MTQ
SACRED[22, 65]	2006	none	–
ROBUSTA[47]	2006	none	–
UWE-1[8]	2006	Passive Control	Permanent Magnets
ION[43]	2006	3-Axis Active Control	MTQ
AAUSat-2[5]	2008	3-Axis Active Control	MTQ, Momentum Wheels

Table 2.3: List of early CubeSats and their ADCS capabilities.

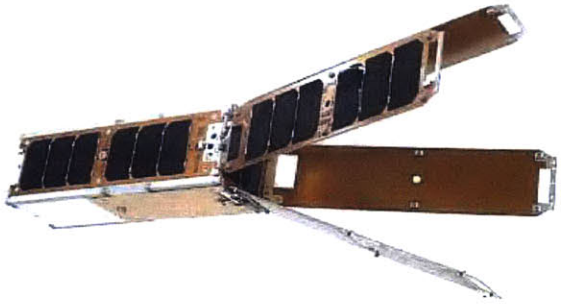

Figure 2-4: Image of the Space Dart configuration of the QBX-1 satellite. Source: `https://directory.eoportal.org/web/eoportal/satellite-missions/c-missions/colony-1`. Accessed April 7, 2016.

being released from their deployer [62]. Having the ability to control the strength and duty cycling of on-board magnets is more complex in actuation and software design, but allows for the significant reduction in this type of risk. An added benefit is the removal of a permanent magnetic field source that can bias or saturate the measurements of any magnetometers on the spacecraft (an often useful source for aiding in attitude determination). The case for electromagnets as actuators on CubeSats is further bolstered by their use in detumbling the spacecraft after deployment.

As was mentioned in Chapter 1, a fairly simple attitude rate control law is employed on at least one CubeSat that has been developed by MIT [49] using magnetic field interaction. The control law, known as *B-dot*, itself is not a new or cutting-edge

control law, but the employment of attitude control laws that are usually fielded on larger, more complicated, traditionally-developed spacecraft, is relatively new in the development of CubeSats[48]. Since CubeSats are often launched as secondary or auxiliary payloads, their release and deployment is uncontrolled and has some initial tip-off tumble of between 1 - 10 degrees per second per axis[13, 37, 40].

Early adopters of three-axis body control used a variety of actuators to enable it. The Canadian Advanced Nanosatellite eXperiment-2 (CanX-2) from the University of Toronto Institute for Aerospace Studies (UTIAS) aimed for constant Earth-pointing for their various payloads. Launched in 2008, CanX-2 was designed to achieve three-axis stabilization from three magnetorquers and one reaction wheel. The reaction wheel served dual purpose for momentum bias against the small environmental attitude disturbances and for slewing the spacecraft to point towards targets of interest.[6] A rendering of the spacecraft is shown in Figure 2-5. UTIAS was able to achieve pointing accuracy below 5°, attitude determination within 1.5°, and attitude stability of about 1° over a 25 minute period, 3-σ.[27]

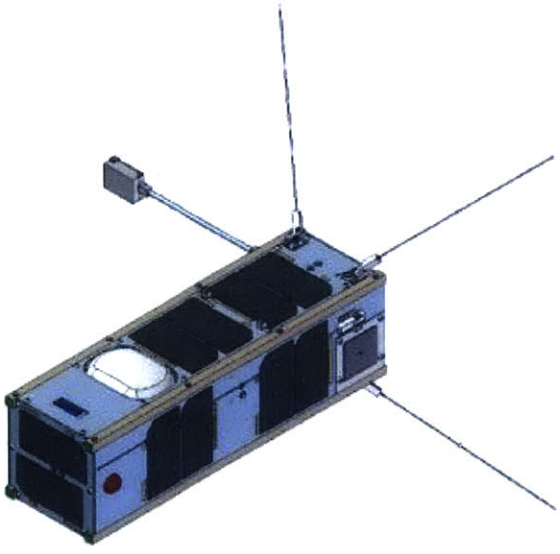

Figure 2-5: CAD rendering of the CanX-2 CubeSat. Launched in 2008, this early UTIAS CubeSat aimed for 3-axis stabilization using three MTQ and one RWA. Source: `https://directory.eoportal.org/web/eoportal/satellite-missions/c-missions/canx-2`. Accessed April 7, 2016.

2.2.4 High Slew Rates on CubeSats

To enable advanced CubeSat missions like lasercomm and LEO-to-LEO imaging, satellites must either have mechanisms that can slew the imagers or transceivers at relatively high rates, or must slew the entire body at these rates for tracking purposes. The volume and power constrained CubeSats make the inclusion of tracking mechanisms for cameras and antennas challenging. This means that the entire satellite bus must act as the actuated system. Enabling this agility is being investigated by several companies that produce CubeSat components[12, 69].

For lasercomm to ground stations, the ADCS must be capable of delivering high slew rates while simultaneously maintaining high accuracy and high precision pointing. This is different from lasercomm cross-links between satellites. Using simple geometric assumptions for LEO satellites passing directly overhead of an optical ground station, one can derive the slew rates (assuming perfect pointing) needed to maintain a comm link at various altitudes. A sampling is provided in Table 2.4. Using radio frequency (RF) communication, beamwidths at the ground are typically hundreds of kilometers for directional communication (non-isotropic). This means that pointing is less stringent than for lasercomm, where beamwidths are on the order of only several kilometers. The optical power of the transmitted beam decreases according to the free space path loss of any radiated wavelength, λ [72]. It is proportional to the distance from the transmitter to the receiver, d, squared,

$$FSPL = \left(\frac{4\pi d}{\lambda}\right)^2 \tag{2.10}$$

To achieve a high signal-to-noise ratio (SNR) at a ground station, lasercomm systems must keep high photon fluxes (ϕ) at the receiver to reduce the effects of the inherent noise terms in optical receivers, σ, (ignoring for now the losses due to optical inefficiencies and atmospheric transmission).

$$SNR_{\text{laser}} = \frac{\phi A t_{\text{integration}}}{\sigma_{\text{total}}} \tag{2.11}$$

- A is the detector area

- $t_{\text{integration}}$ is the integration time
- $\sigma_{\text{total}} = \sqrt{\sigma^2_{\text{shot}} + \sigma^2_{\text{dark-current}} + \sigma^2_{\text{readout}}}$
  - σ_{shot} is the noise inherent in counting incoming photons (a Poisson process)
  - $\sigma_{dark-current}$ is the residual current in a detector when there is no incoming signal
  - $\sigma_{readout}$ is the inherent, combined, electron noise from the detector electronics

The 'tunable' parameters for the lasercomm system designer are the choices of detector type and integration time. The largest impact comes from the contribution of the photon flux. This ultimately generates requirements that a lasercomm transmitter must be pointed such that the peak of the beam point spread function, or Airy pattern, (see Figure 2-6) falls over the ground station whenever possible, *i.e. the incoming photons cannot be assumed to be uniformly distributed over the spot size.*[72]

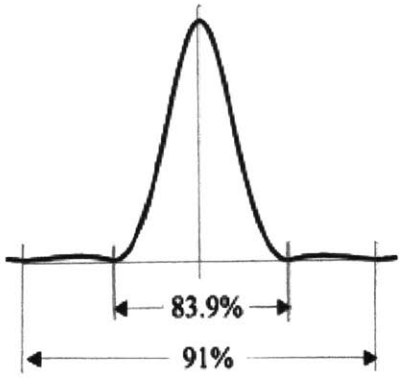

Figure 2-6: Example of an idealized point spread function, or Airy pattern, for an optical system with a circular aperture without aberration. The region in the main lobe contains the majority of the signal energy. Source: `http://spie.org/Images/Graphics/Publications/TT48_Fig3.42.jpg`. Accessed May 15, 2016.

Work by Kingsbury, *et al.*, (2014), has shown that a nanosatellite equipped with a lasercomm downlink must be able to slew at or greater than 1 degree per second. Kingsbury, *et al.*, (2014), also pointed to a similar gap in CubeSat ADCS capabilities

Slew Rates Required for Ground Station Tracking		
Orbital Altitude [km]	Orbital Speed [km/s]	Expected Slew Rate [deg/s]
300	7.73	1.48
400	7.67	1.10
500	7.62	0.87
600	7.56	0.72
700	7.50	0.61
800	7.45	0.53

Table 2.4: Sampling of slew rates needed for optical ground station tracking. These values assume constant tracking during slew maneuvers.

needing high slew rates while maintaining pointing accuracy. The solution proposed for the Nanosatellite Optical Downlink Experiment (NODE) was a two-stage pointing approach. Here, we work to improve the (single stage) body pointing of CubeSats, achieving down to two degrees of pointing accuracy. From there, a second stage fine steering mirror would provide the required accuracy (0.01 degrees, 3σ) to achieve 10 Mbps with a 1550 nm, 1 W (output) laser system on a CubeSat in circular 400 km LEO to a 30 cm aperture ground telescope. The work presented here assumes a single-stage approach for simulation simplicity, meaning that the spacecraft body alone must be pointed with high accuracy.

Another communication architecture that is appropriate for inexpensive systems like CubeSats is the 'bent pipe' data system. This arrangement uses satellites as relay way-points to forward data from one point on Earth to another. Currently, these data relay systems are used by industry and government alike and rely solely on RF communication bands. If a constellation or network of low-cost, easily replaced optical communication relay satellites were employed, the bandwidth potential for these data relay systems would be greatly increased. For such a system to operate, there is a need to enable satellite-to-satellite lasercomm crosslinks for high-bandwidth comm between satellites. Such a project for CubeSats is also being investigated by the MIT STAR Lab.[45]

The Free Space Lasercomm and Radiation Experiment (FLARE), project aims to demonstrate intersatellite lasercomm between two 6U CubeSats. Crosslink lasercomm

with these platforms will demand high performance ADCS for success. This system will nominally operate with the satellites in a leader-chaser configuration with no relative velocities between the satellites. However, we can envision a scenario where a constellation of satellites is configured in different orbital planes where the satellites have differential relative velocities. For instance, in a constellation of polar orbits all synchronized in direction, there will be two orbital planes that will inevitably be non-synchronized, as is illustrated in Figure 2-7. This configuration gives good global coverage, but also gives rise to high relative orbital velocities at or near the poles. If an intersatellite link were to be maintained during the pass of two adjacent non-synchronized satellites, this could drive slew rates of many tens of degrees per second. Tracking at these rates is unreasonable, even for very agile spacecraft[23]. However, using advanced ADCS filtering techniques like those presented in this work might allow for extending the envelope of accurate tracking during high slew rates, increasing mission up-time.

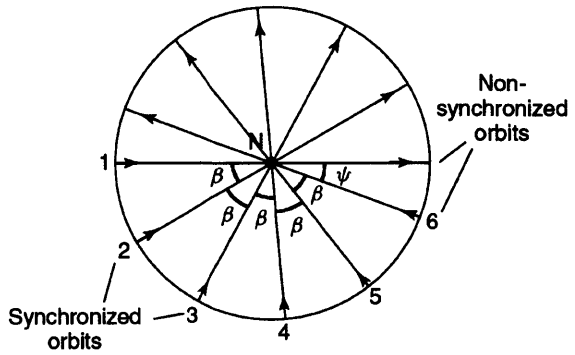

Figure 2-7: An example of a polar constellation with two adjacent but non-synchronized orbital planes, viewed down at the north pole. β denotes the equal spacing between orbits, ψ denotes the spacing between adjacent, non-synchronized planes.Image adapted from *Spacecraft Systems Engineering*[18]

2.2.5 Fine Pointing on CubeSats

While there are numerous examples of the increase in CubeSat pointing capability, the focus here is on three missions of interest. The first is a CubeSat mission initially called ExoplanetSat and now called ASTERIA[57] that was developed at MIT to im-

age exoplanets that required high pointing ability on a 3U bus[48]. The second is a 3U CubeSat mission developed by MIT and MIT Lincoln Laboratory for weather sensing, called MicroMAS[74]. The last is a CubeSat mission by the Aerospace Corporation that aimed to demonstrate optical comm on nanosatellites, called OCSD[4].

ExoplanetSat

Imaging distant astronomical objects using a CubeSat platform in LEO requires the imaging system to be extremely stable and accurate. A 3U-sized spacecraft called ExoplanetSat designed at MIT by exoplanet researchers, shown in Figure 2-8, was designed to measure exoplanet transits in front of their host stars, requiring very precise pointing and sensitive photometry.[44] This CubeSat was designed to have a two-stage pointing system that was at least two orders of magnitude better than the SOA at the time (2014) on other CubeSats. ExoplanetSat uses coarse three-axis body pointing with a three-axis set of reaction wheels and fine pointing using a piezo stage for the imaging payload. Simulations by C. Pong, (2014), showed that this system had the potential to achieve 2.3 arcsec (3-σ) pointing precision[48]. The ADCS hardware proposed for this mission (originally slated for 2016, but which has since changed to the JPL Phaeton project called ASTERIA[30]) consisted of: A star camera and tracker for fine attitude knowledge, medium sun sensors and a three-axis magnetometer for coarse attitude knowledge, a GPS receiver for absolute position and velocity, three orthogonal reaction wheels and torque rods for coarse attitude control, and a piezoelectric stage for the fine pointing control.[48] The attitude sensing and control hardware on ExoplanetSat was chosen to be COTS or custom-COTS for low-cost design and ease of procurement. This approach is fairly common on CubeSat missions in the academic sector[36, 48, 49]. A similar COTS-first approach was taken for the next mission to be discussed, the MicroMAS CubeSat.

MicroMAS

The Microsized Microwave Atmospheric Satellite CubeSat from MIT was another 3U satellite designed with three-axis pointing control. However, the ADCS responsibil-

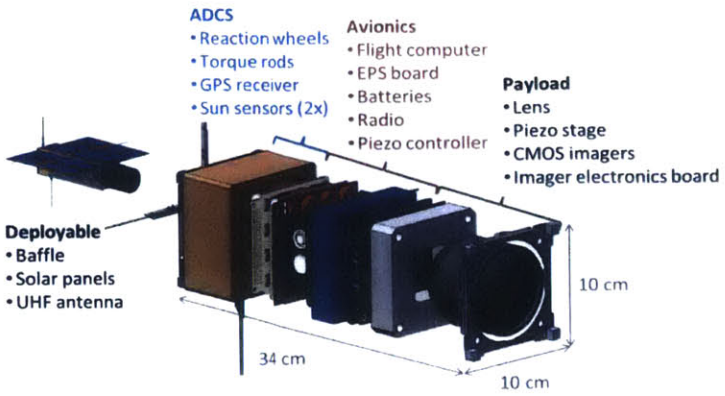

Figure 2-8: CAD rendering of the ExoplanetSat CubeSat, originally designed to be a 3U sized satellite with three-axis body pointing control and fine piezoelectric stage pointing. Image from *High-Precision Pointing and Attitude Estimation and Control Algorithms for Hardware-Constrained Spacecraft*[48]

ities and pointing needs differed from ExoplanetSat. MicroMAS was a dual-spinner satellite that needed to counter the momentum generated from the spinning microwave sounding payload and still maintain at least one degree pointing accuracy in all three axes for weather sensing[49, 73]. Though the pointing accuracy requirements were far less stringent than those on ExoplanetSat, the ADCS operation designed for MicroMAS was still at the cutting edge of nanosatellite capabilities for actual fielded systems at the time of its deployment (early 2015). Unfortunately, the bus suffered a communication system failure soon after deployment and the full system pointing capabilities were not exercised.

The MicroMAS ADCS used an all-in-one COTS attitude control unit from Maryland Aerospace, Inc. The MAI-400 ADCS unit contained three orthogonal reaction wheels and magnetorquers for attitude control actuation and interfaced with a three-axis magnetometer, a three-axis gyroscope, two orthogonal EHS heads, and six coarse sun sensors for full 4π steradian sky coverage. A CAD rendering[49] and side view of the spacecraft are shown in Figure 2-9a and Figure 2-9b for reference. The 1U spinning payload can be seen at the far right of Figure 2-9b.

CubeSat projects from the MIT Space Systems Laboratory have utilized relatively simple nonlinear control laws like a proportional-derivative control algorithm[48, 73].

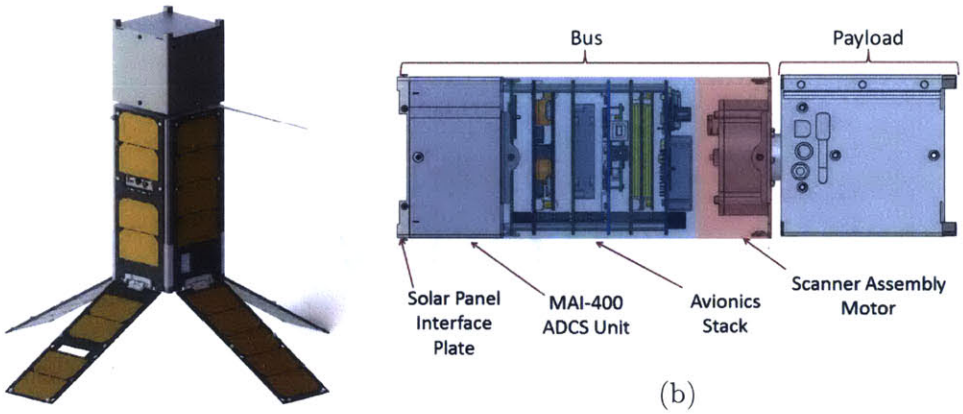

(a) (b)

Figure 2-9: (a)CAD rendering of the MicroMAS 3U CubeSat, and (b)a side view of the major spacecraft components. Images from *Testing the Attitude Determination and Control of a CubeSat with Hardware-in-the-Loop*[49]

Here, the control software is designed to apply appropriate torques using the reaction wheels to enable three-axis attitude control. Equation 2.12 shows the different elements that the RWA control torque, τ_{RW}, is composed of. These include the spacecraft rotation rates, $\hat{\omega}$, the spacecraft inertia matrix, $\mathbf{J}$, the RWA momentum, $\mathbf{H}$, disturbance torques, τ_{dist}, the proportional feedback terms, $\mathrm{K_p}$ and α_{e}, and the derivative feedback terms, $\mathrm{K_d}$ and ω_{e}.

$$\tau_{\mathrm{RW}} = \hat{\omega} \times (\mathrm{J}\hat{\omega} + \mathbf{H}_{\mathrm{RW}}) - \tau_{\mathrm{dist}} - \mathrm{K_p}\alpha_{\mathrm{e}} - \mathrm{K_d}\omega_{\mathrm{e}} \tag{2.12}$$

OCSD

The third mission we present is designed to take a major step forward in CubeSat demonstrated pointing ability. The NASA-funded Optical Communication and Sensor Demonstration (OCSD) program was selected by NASA to demonstrate up to 50 Mbps optical downlink on very small CubeSats. The OCSD spacecraft are each only 1.5U. The first CubeSat of three built, OCSD-A, was launched in October of 2015, but suffered a software failure[23]. The remaining pair, OCSD-B and C are currently slated for a summer 2016 launch[23]. OCSD was developed by the Aerospace Cor-

poration (Aerospace), and a different design philosophy was taken for this program. Instead of the COTS-first approach, Aerospace mixed custom-COTS with miniaturized hardware specifically designed for this mission. This method allowed for very high performance attitude determination and control on an even smaller scale.

The OCSDs are only half the size of the previously mentioned 3U satellites. A CAD rendering can be seen in Figure 2-10[4]. OCSD uses a wide array of attitude sensors, far more than would be seen on typical CubeSat missions.[4] For coarse attitude sensing, each satellite contains six two-axis sun senors, two three-axis magnetometers, four Earth horizon sensors, and a two-axis Earth nadir sensor. This combination of sensors allows the OCSD satellites to achieve about 1 degree of pointing accuracy, with attitude sensing redundancy for added reliability[23]. To achieve the even higher pointing accuracy needed for the downlink demonstration (about 0.1 degree), OCSD also contains a pair of star trackers and implements closed-loop tracking of an optical beacon uplink from the ground station. For control, the satellites have a triad of reaction wheels and magnetorquers, also custom designed and built. The custom approach taken by the Aerospace Corporation, a Federally Funded Research and Development Center, is an example of what may be possible for a larger number of CubeSats if the hardware and software used in such missions becomes available to the larger space community and CubeSat development sector.[4, 23]

Implications of Fine Pointing

It can be seen from the example three missions we focus on that CubeSat usage is gaining popularity for increasingly complex missions. With the greater reliance on CubeSats for gathering useful science data like weather sensing weather sensing, Earth imaging, or astronomical imaging, comes harder requirements for pointing capability for the Attitude Determination and Control System. Figure 2-11 illustrates the increase of pointing accuracy required for three different 3U CubeSat buses. These range from commercial applications like Planet Labs to CubeSat missions like the NODE program, which aims to demonstrate lasercomm downlinks from LEO.

Based on our example missions, we can see the need for attitude filters that can

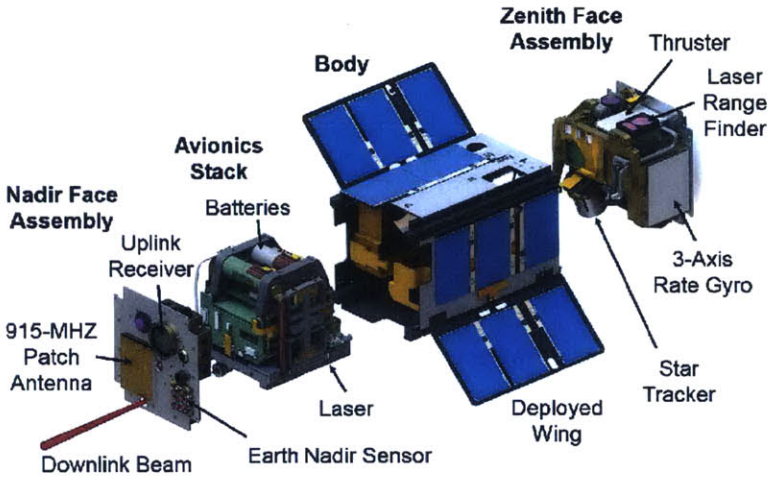

Figure 2-10: Exploded view rendering of the pathfinder OCSD satellite. This was a highly miniaturized system, only 1.5U in size. Source: `https://directory.eoportal.org/web/eoportal/satellite-missions/a/aerocube-ocsd`. Accessed April 15, 2016.

handle the potentially noisy attitude sensors while still maintaining fine pointing, and more stringent missions that can achieve fine pointing during fast maneuvers with high slew rates. This is not a trivial task, and in Chapter 4 we see to what extent these pointing demands and expectations tax the Kalman filter or, more precisely, a version of such for nonlinear systems called the Extended Kalman filter [48, 49, 73].

2.2.6 The Kalman Filter

The seminal method of linear filtering known as the Kalman Filter first appeared in print in 1960 by R. E. Kalman, and many different variations have followed since.[1] The formulation of the continuous form of the Kalman Filter (KF), or Linear Quadratic Regulator (LQR), is beyond the scope of this work, and we refer the interested reader to references in the literature, such as: *Optimal Estimation of Dynamic Systems* by Crassidis and Junkins (2004). For CubeSats, the discrete forms of the different filters are used, as is the case with most dynamic systems that use digital controllers or processors[17]. The simulations built for this work, as described in Chapter 3, use discrete-time calculations since they aim to model the behavior of the microcontroller used in the previously described MicroMAS and ExoplanetSat

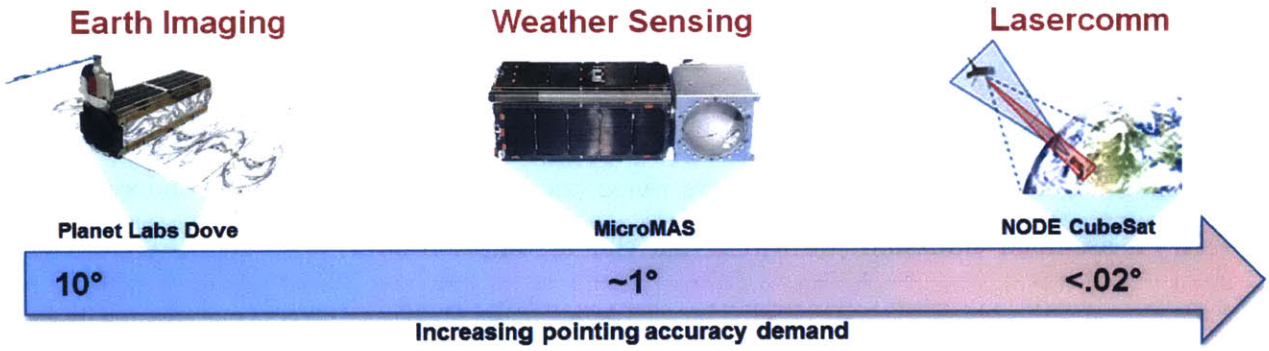

Figure 2-11: Illustration of the increase in pointing accuracy required for different missions. All CubeSats shown are 3U buses.
Image credit: Overall image - W. Marlow.
Image Sources: Planet Labs Dove, `http://eijournal.com/wp-content/uploads/2014/11/PlanetLabs_Dove-659x362.png`. Accessed December 15, 2016. MicroMAS bus `https://directory.eoportal.org/web/eoportal/satellite-missions/m/micromas-1`. Accessed December 7, 2016. NODE diagram, `https://deshpande.mit.edu/portfolio`. Accessed December 15, 2016.

missions.

The purpose of any estimator is to use past measurements and known (or assumed) system properties, like measurement noise and system process noise parameters, to inform future estimates of the system dynamics. As system designers, we will not know the exact state of the spacecraft, but we must use the measurements of attitude to infer it. As we receive measurements, we include them in our estimate of the dynamics. This recursive behavior allows the estimator to take prior system behavior into account to update the system covariance parameters (denoted as Q).[17, 54, 59]

We begin with the representation of the system, or the parts of the system we are estimating the behavior for, with notation as defined by Roy, (2015). The state variable, x is a representation of the dynamics of the spacecraft that we wish to estimate; it is a vector of system variables, the *state vector* ($\mathbf{x}$)[54]

$$\mathbf{x} = \langle x_1,\ x_2,\ x_3,\ \ldots\ x_n \rangle^T \tag{2.13}$$

where

$$\mathbf{x}, \hat{\mathbf{x}} \in \mathbb{R}^n \tag{2.14}$$

and the state estimate of $\mathbf{x}$ is denoted as $\hat{\mathbf{x}}$ after we take erroneous or noisy measurements into consideration. The *process noise* (random execution noise) of the system ($\mathbf{w}$) is assumed Gaussian (we will revisit this assumption later),

$$\mathbf{w} = \langle w_1,\ w_2,\ w_3,\ \ldots\ w_n \rangle^T \tag{2.15}$$

where, by definition of Gaussian noise,

$$w_i \sim \mathcal{N}(0, N_i) \quad \text{additionally,} \quad E[w_k w_j] = W \tag{2.16}$$

such that, using the discretized system state matrix, A_d, we can obtain a method of propagating our system dynamics and covariance to a future time step. The discrete KF can be initialized from either the update or propagate steps, as seen in the recursion loop in Figure 2-12. The discrete Kalman filter is built upon the assumptions that both the model of the system and the measurements of the state are available in discrete-time formulation. These measurements, $\mathbf{y}$, and the error (noise) vector $\mathbf{v}$, are denoted by

$$\mathbf{y} = \langle y_1,\ y_2,\ y_3,\ \ldots\ y_m \rangle^T \quad \text{and} \quad \mathbf{v} = \langle v_1,\ v_2,\ v_3,\ \ldots\ v_m \rangle \tag{2.17}$$

where

$$\mathbf{y}, \mathbf{v} \in \mathbb{R}^m \quad \text{and} \quad v_l \sim \mathcal{N}(0, N_l) \quad \text{and} \quad E[v_o, v_p] = R \tag{2.18}$$

With the descriptions of our state, measurements, and noise, we also need to denote and index the discretization of time. Here, a subscript notation is used[54] and shown in Table 2.5. Subscripts are used rather than superscript notation as seen in other works[17, 59].

The discrete-time Kalman filter is then[54, 59],

Subscript standards used for discrete KF.	
Notation	Description
$k-1$	Preveious time step
k	Current time step
$k+1$	Future time step
$k\|k-1$	Used for *a priori* estimate. Current estimate using all measurements up to, but not including time k.[59]
$k\|k$	Used for *a posteriori* state estimate. Current estimate based on all measurements up to and including time k.[59]
$k+1\|k$	Used for *prediction* step. Propagate state statistics to future time step using *a priori* estimate.

Table 2.5: Subscript convention used in this work.

$$\mathbf{K}_k = \mathbf{Q}_{k|k-1}\mathbf{C}_d^T\mathbf{C}_d(\mathbf{Q}_{k|k-1}\mathbf{C}_d^T + \mathbf{R}_k)^{-1} \tag{2.19}$$

$$\mathbf{Q_{k|k}} = (\mathbf{I} - \mathbf{K}_k\mathbf{C}_d)\mathbf{Q}_{k|k-1} \tag{2.20}$$

$$\hat{\mathbf{x}}_{k|k} = \hat{\mathbf{x}}_{k|k-1} + \mathbf{K}_k(\mathbf{y}_k - \mathbf{C}_d\hat{\mathbf{x}}_{\mathbf{k|k-1}}) \tag{2.21}$$

If we are beginning with some initial estimate and state covariance, then we have $\hat{\mathbf{x}}_0$ and $\mathbf{Q}_0$ in place of $\mathbf{Q}_{k|k-1}$

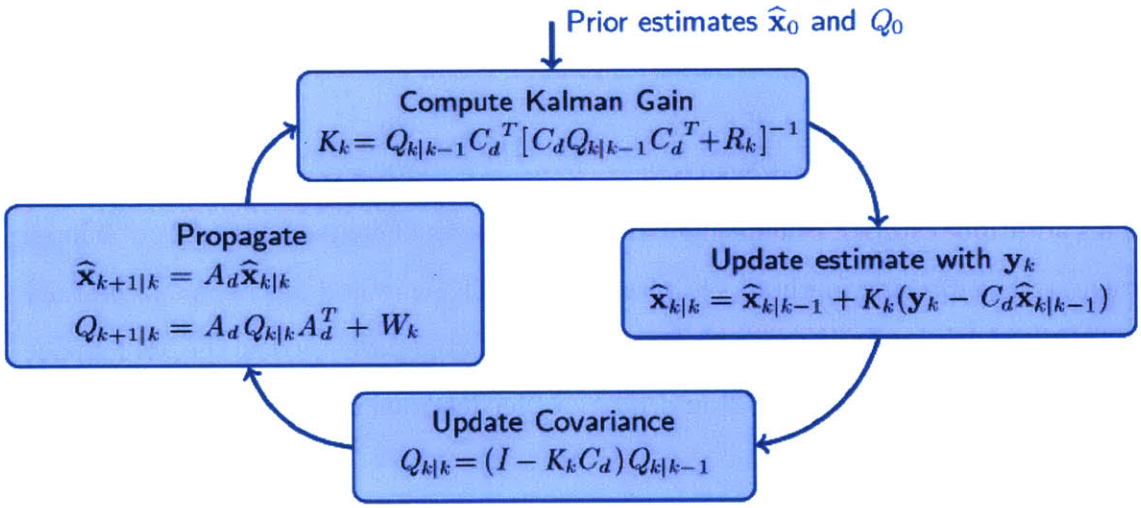

Figure 2-12: Discrete Kalman Filter recursion loop. Image source from Nicholas Roy (2015). *16.322 Class Lecture 8: Discrete Kalman Filtering* [PDF slides].

The standard KF formulation as presented here is based on the assumptions that

the measurement and process noise, w_k and v_k, are both Gaussian, zero-mean, uncorrelated, and white.[59] When this is the case, along with the assertion that we are working with a linear system, then the KF minimizes the estimation error, and is the best *linear filter* for the system. [59] A much more widely-utilized approach that extends the KF to nonlinear systems will be discussed next in Section 2.2.7.

2.2.7 The Extended Kalman Filter

In this section, the traditional Kalman filter is expanded to apply to nonlinear systems, and is known as the Extended Kalman Filter (EKF).

The attitude dynamics for spacecraft will be explained further in Chapter 3, but the equations of motion for these and many other systems are nonlinear in nature. The traditional KF fails for nonlinear systems. The EKF, proposed in 1967 [59], uses linearization of the nonlinear system dynamics around the Kalman filter estimate. This allowed the Kalman filter to be 'extended' to more systems of interest.

The EKF is based on the assumption that the actual or true state of the system is sufficiently close to the estimate such that the linearization errors are small.[17] The filter gain and covariance uses the first-order partial derivatives of the state and measurement equations[17, 59],

$$F(t) \equiv \left.\frac{\partial \mathbf{f}}{\partial \mathbf{x}}\right|_{\hat{\mathbf{x}}(\mathbf{t}),\mathbf{u}(t)} \quad \text{and} \quad H(t) \equiv \left.\frac{\partial \mathbf{h}}{\partial \mathbf{x}}\right|_{\hat{\mathbf{x}}(\mathbf{t})} \tag{2.22}$$

This additional step of calculating partial derivatives of course adds computational overhead to the filtering method. Despite this, the EKF method has been successfully implemented in two different CubeSat missions that were developed at the MIT Space Systems Laboratory (SSL)[48, 73] and many other institutions.

2.3 Gap Identification

In order to increase the utility of CubeSats to satisfy more science-driven and imaging-based needs of CubeSat agility, we must begin looking at different methods of attitude

filtering that are more robust to system nonlinearities and measurement noise properties.

Currently fielded CubeSats that represent some of the most recent flights are demonstrating precision attitude control, but still use an EKF approach. BRITE, the BRIght-star Target Explorer constellation, is demonstrating arc-minute stability using only EKF for precision imaging[24]. This implementation works well since BRITE stares at bright astronomical targets which have a low relative rate to the satellite. The Canadian Advanced Nanospace eXperiment-4 and 5 (CanX-4 and 5) are currently using an EKF for state estimation and filtering to achieve 0.5 to 1 degree pointing accuracy for accurate thruster firing only, since the mission is a formation flying demonstration[53]. The University of Michigan Radio Aurora Explorer (RAX) satellites, RAX-1 and RAX-2 are performing attitude estimation with a multiplicative Extended Kalman Filter to obtain 0.5 degree (1-σ attitude accuracy on orbit[2]. We previously described the OCSD mission that is demonstrating high attitude estimation accuracy, but the filtering method has not disclosed.

If we look again at Figure 2-1, the work that has been done on KF and EKF fall well within advancing CubeSat pointing, the first section of the diagram, in green. To better address system nonlinearities, potentially changing system noise properties, and noise properties that may not necessarily be Gaussian in nature, we must move away from the standard KF and the EKF.

The unscented transformation is a further extension of the Kalman Filter[67] that is widely used for standard (larger) spacecraft attitude estimation and determination[31], and has been only recently investigated and proposed for CubeSat attitude determination [19, 31, 55, 68]. The earliest mention of proposing the use of a UKF for Cubesat attitude estimation was from Vinther, *et al.*, (2011). They proposed and reformulated the UKF to estimate the quaternion error state. Li *et al.*, (2013), formulated a new Adaptive UKF (AUKF) for the use on a 3U CubeSat. The AUKF had a larger state, estimating the Euler angles, gyro bias, and angular velocity of the satellite[32]. Simulations by Grigore, (2015) showed the implementation of a UKF on a 3U CubeSat. The UKF was shown to obtain arc-minute attitude estimation for low-rate attitude

motion using star trackers as the main sensors for the filters[19]. Lastly, Sanfedino *et al.*, (2015), developed another variation of the AUKF for CubeSat attitude estimation. Their reformulation of the filter used a single attitude sensor (magnetometer measurements) and Modified Rodrigues Parameters (not covered in the scope of this work) as the attitude representation parameters[55]. The UKF will be covered in detail in Section 3.3, along with the variations and combinations of variations that are used in our work.

2.3.1 Combining Filtering Methods

The long-term goal is the development of a minimal-set adaptive Unscented Kalman filter, or MAUKF. This combination filter will have lower overhead computational cost[68] than a standard UKF while still maintaining the flexibility and robustness to uncertainties about the system [31], and will use an estimation scheme based on filtering of the system quaternion attitude representation. Previous work has also not had simulation environments as detailed as that which the author has been able to use from previous flight missions. This highly detailed simulation allows us to use flight-like system data to exercise the filters.

Chapter 3

Modeling and Simulation Approach and Attitude Filter Development

3.1 Overview and Simulation Approach

Chapter 1 laid out details of the different attitude sensors and actuators that are used in this work. Chapter 2 introduced the state of the art in CubeSat attitude estimation and control, and identified the research gap that this work will address. In this chapter, the framework for the simulation approach is revisited and expanded.

3.1.1 Bus Sizes and Coordinate Convention

The 3U bus is the basis for the majority of the analysis and simulation work presented. On a standard 3U CubeSat, the individual units are stacked on one another to form a long rectangular body with dimensions of 100 mm $\times$ 100 mm $\times$ 340.5 mm, as set forth by the CubeSat Design Specification (CDS)[16]. Figure 3-1 also shows the 3U bus coordinate convention as required by the CDS. This ultimately is not the coordinate system used for the simulation. Instead, a more standard axis convention is used based on the spacecraft assumed direction of motion. In Figure 3-2, the axes are shown with the body Z axis nominally aligned with the zenith direction, and the body X axis nominally aligned with the spacecraft ram direction. The body Y axis

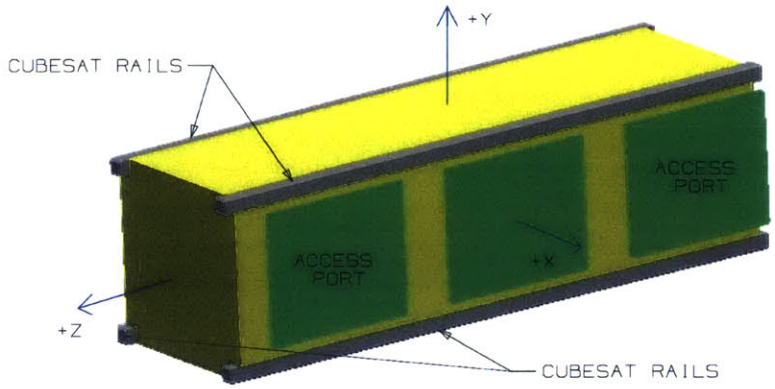

Figure 3-1: Excerpt from the CubeSat Design Specification from California Polytechnic Institute of Technology[16]. Image depicts a typical 3U CubeSat with the required coordinate convention.

completes the right-handed triad.

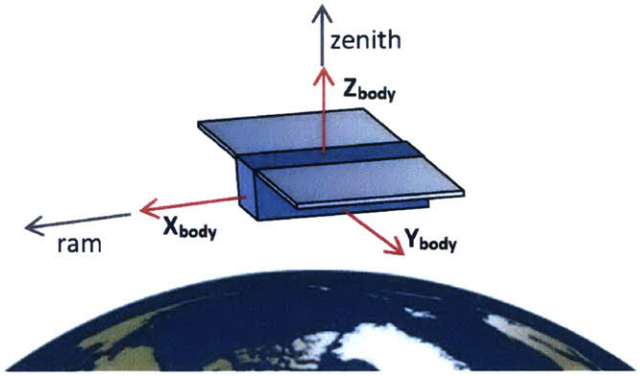

Figure 3-2: Graphic showing the spacecraft body frame (red) with relation to the zenith and ram directions (gray) of the orbit. *Image Credit: W. Marlow*

The inertia properties assumed for the 3U and 6U buses are based on simplified models of the spacecraft. The inertia tensor used for the 3U bus is based on the configuration shown in Figure 3-2 with two double-deployed solar panels in full deployment and normal to the $\pm$ Z-axis. The 3U is assumed to be at the maximum allowable mass of 4 kg[16]. The 6U inertia properties are based on principal axis configuration using a 100 mm $\times$ 200 mm $\times$ 340.5 mm solid geometry with mass of 14 kg. This assumes that the spacecraft has no deployed panels, similar to the system shown in Figure 3-3. The 6U is essentially two 3U CubeSats stacked side-by-side, but with a higher combined mass.

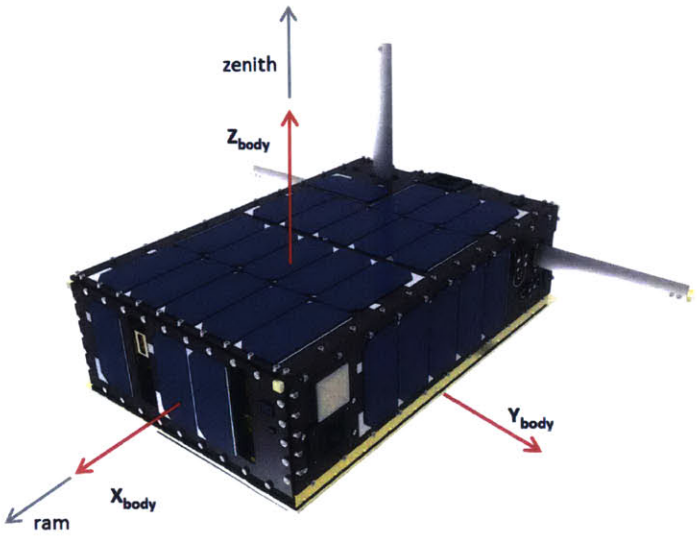

Figure 3-3: Example 6U with body axes shown, relative to orbit zenith and ram directions. Source: `http://www.nasa.gov/sites/default/files/thumbnails/image/dellingr_artist_concept.jpg`. Accessed April 17, 2016.

The modeled systems have the following inertia characteristics, with the inertia matrix for the 3U denoted $\mathbf{I_{3U}}$ and the 6U denoted $\mathbf{I_{6U}}$:

$$[I_{3U}] = \begin{vmatrix} 15.7 \times 10^{-3} & -9.0 \times 10^{-4} & 3.0 \times 10^{-4} \\ -9.0 \times 10^{-4} & 44.6 \times 10^{-3} & 1.0 \times 10^{-4} \\ 3.0 \times 10^{-4} & 1.0 \times 10^{-4} & 52.2 \times 10^{-3} \end{vmatrix} [\text{kg} \cdot \text{m}^2] \tag{3.1}$$

and

$$[I_{6U}] = \begin{vmatrix} 58.3 \times 10^{-3} & 0 & 0 \\ 0 & 14.7 \times 10^{-2} & 0 \\ 0 & 0 & 18.2 \times 10^{-2} \end{vmatrix} [\text{kg} \cdot \text{m}^2] \tag{3.2}$$

3.1.2 Simulated Actuator Sizing

If we examine the inertia properties of the larger spacecraft bus, we can determine if the actuators described in Table 1.2 are sized appropriately for the spacecraft and for the scenarios presented in Chapter 1.

The B-dot control law briefly described in Chapter 2 is typically used to detumble spacecraft, and is described in detail as well as in application in several works[49,

50, 63]. CubeSats are ejected from deployers with some non-zero tip-off rate. Active detumble is often done with commanded magnetic dipoles to oppose the spacecraft rotation[48, 73]. In the case of maneuvering, however, we wish to look at the capability of the ADCS system to produce higher slew rates in the host spacecraft rather than slow it as with detumble.

Using classical rotational dynamics[56], we can easily find if the wheels we have chosen for the attitude simulations are capable of providing the momentum exchange needed to spin a spacecraft up to some nominal rate. First, we assert that the ADCS has fully utilized the wheels (or they have transferred the maximum momentum possible to the spacecraft), with the total angular momentum of the spacecraft denoted as the 3x1 vector $\mathbf{H}$. The spacecraft body rates in inertial space are denoted as the 3x1 vector ω_I. To determine what slew rates the wheels are capable of imparting, the angular momentum equation is used,

$$\mathbf{H} = [I_{sat}]\omega_I \tag{3.3}$$

to obtain the spacecraft body rates,

$$\omega_I = [I_{sat}]^{-1}\mathbf{H} \tag{3.4}$$

where I_{sat} is either $\mathbf{I_{3U}}$ or $\mathbf{I_{6U}}$.

With the simple exercise above, it can be seen that the maneuvers described in Section 1.2 that require the spacecraft to slew at single degrees per second at 400 km altitude orbits can be accommodated with these actuators. To bound the performance of the buses chosen in this work, the 3U bus can be equipped with over-sized wheels, for example, the BCT XACT ADCS system. (Also, the 6U bus can have slightly smaller wheels the MAI-400 attitude control unit). Performing the exercise with these systems yields,

$$\omega_{I3U} = I_{3U}^{-1}[\text{kg}\cdot\text{m}^2](15\ 15\ 15)^T[\text{mNms}] \approx (34.7\ \ 12.7\ \ 10.0)^T[\text{deg/s}] \tag{3.5}$$

for the 3U system, which agrees closely with claims by the manufacturer[12]. Additionally,

$$\omega_{I6U} = I_{6U}^{-1}[\text{kg} \cdot \text{m}^2](9.351\ 9.351\ 9.351)^T[\text{mNms}] \approx (14.7\ \ 5.8\ \ 4.7)^T[\text{deg/s}]. \quad (3.6)$$

The wheels can clearly impart the required momentum to slew the different spacecraft at the desired rates. This first-order analysis assumes no disturbances and perfect angular rate measurements. In real systems there will be the added complication of modeling and filtering measurement and process noise for attitude determination.

3.1.3 Simulated Sensor Noise Characteristics

Measurement Noise Characteristics

The different sources of noise that affect an estimator in practice originate from each of the sensors that are being utilized for attitude measurements, both relative and inertial in nature. The attitude sensors must be extensively tested such that the noise is well-characterized for fielded systems, since attitude estimation utilizes measurement noise statistical properties for filtering (see Section 3.3.2).

The noise characteristics for the 3-axis gyroscope, 3-axis accelerometer, and 3-axis magnetometer are used for the purposes of the estimator work. Future iterations of this work will include noise and input from all sensors; for more details, see Chapter 5. The specifications for the ADIS16334 IMU and RM3000 magnetometer are taken from the manufacturer datasheets[3, 52], rather than empirical data. The performance characteristics are presented in Table 3.1.

To illustrate the angular rate, velocity walk, and magnetic field noise in system measurements, simulated results are presented in Figure 3-4, Figure 3-5 assuming at-rest sensors (zero angular rate and zero acceleration), and in Figure 3-6. Here the angular rate and velocity random walk noise statistics are modeled with the advertised bias performance, but with more conservative variance (3 times worse than advertised performance) to account for less than nominal performance. The magnetometer noise parameters are assumed 3-σ values from the manufacturer specification

Sensor Noise Parameters		
Parameter	Value	Units
ADIS16334 Gyroscope		
Initial Bias	± 3 1-σ	deg/sec
Random Walk	2 1-σ	deg/$\sqrt{hr}$
ADIS16334 Accelerometer		
Initial Bias	± 12 1-σ	mg
Random Walk	0.11 1-σ	m/s/$\sqrt{hr}$
RM3000 Magnetometer		
Random Noise	35 (assumed 3-σ)	nT

Table 3.1: Data sheet performance values for the ADIS16334 inertial measurement unit[3] and the RM3000 Geomagnetic Sensor Suite magnetometer[52].

and datasheets.

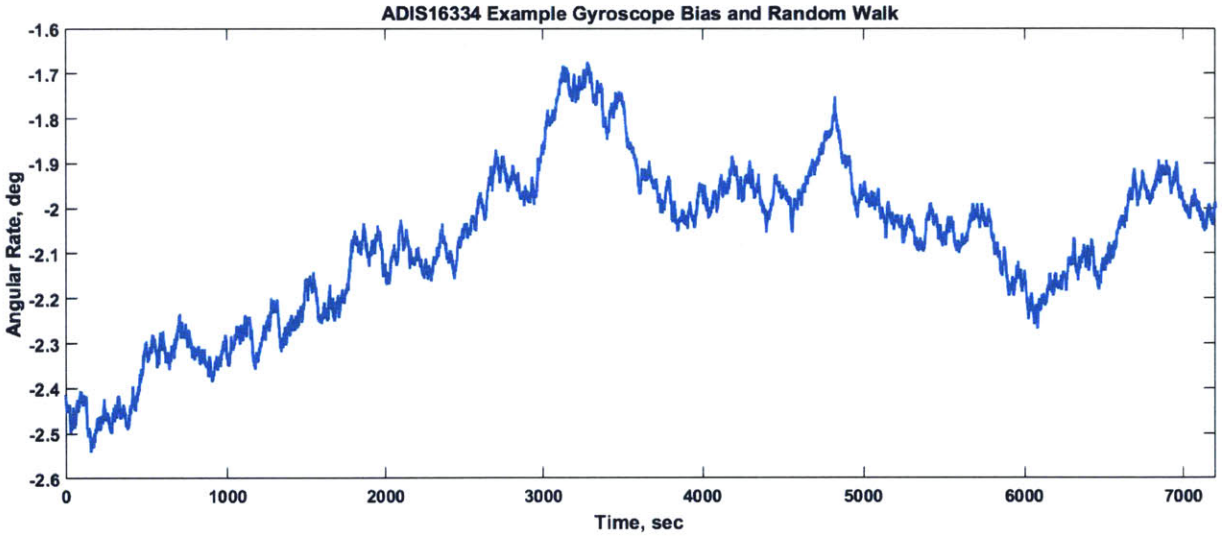

Figure 3-4: Random gyroscope bias and angular rate walk are shown for one axis over a two hour period. *Image credit: W. Marlow.*

Process Noise Characteristics

Process noise is included in the system dynamics as the covariance matrix $\mathbf{W}$, and the error term, $\mathbf{w}$. Process noise would be injected from the actuators or from the external environment for any real system where these have not been adequately captured by the system models[48]. The process noise is captured in the estimator execution in this work by the injection of fictitious process noise, with $\mathbf{w} \in \mathbb{R}^3$.

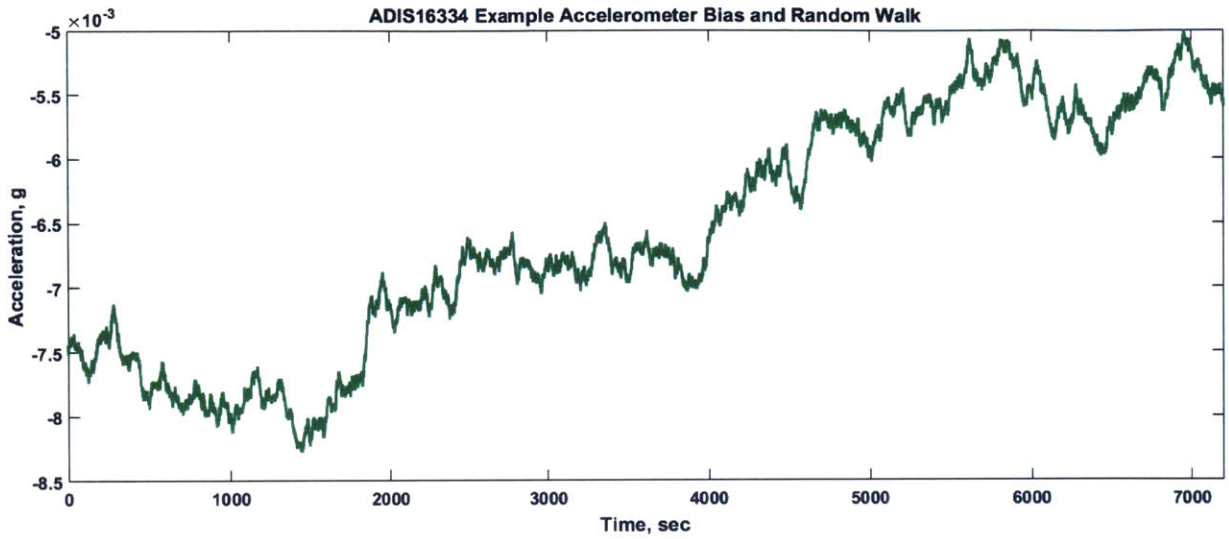

Figure 3-5: Random accelerometer bias and walk are shown for one axis over a two hour period. *Image credit: W. Marlow.*

3.2 Data Gathering

The data used for developing and testing the filters in this work was gathered from a Simulink and MATLAB simulation of the different buses and orbit combinations. The basis of this environment was developed for previous MIT programs and contains models of the different CubeSat actuators described in Chapter 1.

Since many CubeSats are manifest as auxiliary payloads for ISS-bound launches, the simulation contains models of the orbital disturbances that are expected for a satellite in a LEO environment. The orbital parameters for the different circular orbits are shown.

Orbit details from simulations.		
Orbit	Altitude	Inclination
ISS	403.5 km	51.64°
Sun-synch	400 km	97.03°
High-LEO	800 km	45°

Table 3.2: Altitude and inclination for the three circular orbits are shown.

The simulation includes the ISS orbit (where the orbit is assumed circular and the altitude is based on the current semi-major axis at the time of writing[46]. At the ISS-orbit, atmospheric drag will dominate the disturbance forces.

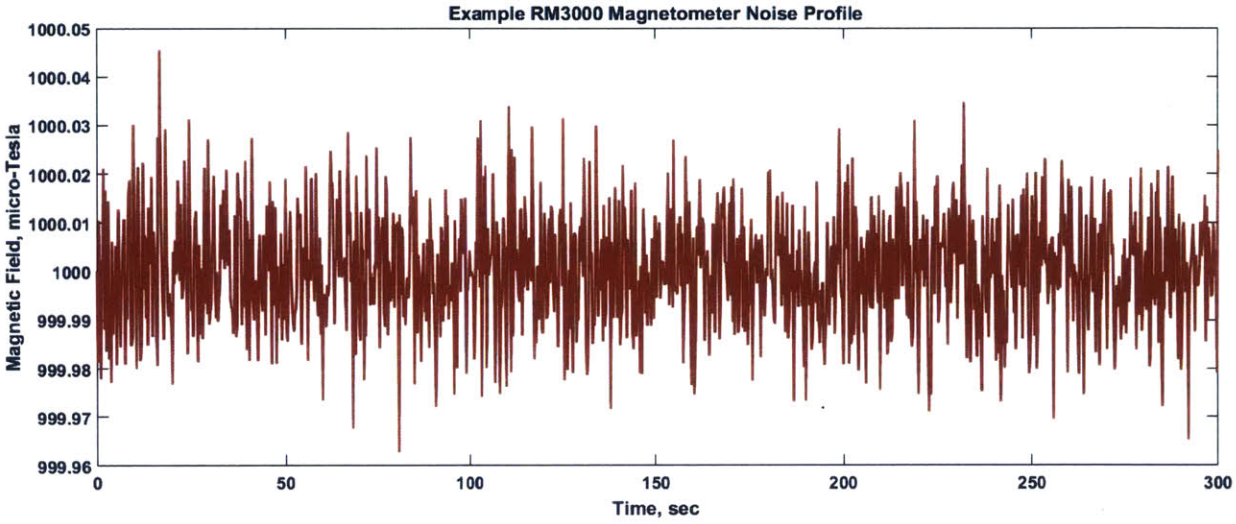

Figure 3-6: A measurement of a constant 1000 μT magnetic field is assumed over a five minute period. *Image credit: W. Marlow.*

The second orbit is a Sun-synchronous Orbit (SSO) at 400 km (also circular). In this lower altitude, like the ISS-orbit, the atmosphere will dominate. This orbit is included because it is a useful orbit for Earth sensing. A Systems Tool Kit (STK) analysis on such an orbit shows full *accumulated* global coverage for a single satellite in this orbit using a simple 45° half-cone sensor. This orbit also presents an interesting magnetic environment. The orbit is inclined at roughly 97 degrees, where Earth's geomagnetic pole is tilted by about 11 degrees[21], resulting in the satellite orbiting occasionally with its direction of motion aligned with the magnetic field lines. This can cause issues due to magnetic actuation limitations (see Equation 1.3).

Finally, an 800 km altitude high-LEO orbit is included, where atmospheric disturbances play a smaller role. Such an orbit altitude would allow for extended mission lifetimes for CubeSat missions or CubeSat constellations and may require a method to actively deorbit.

Several key data products were gathered from these orbits simulations. The disturbance torques acting upon the satellites were recorded and used for propagating the rigid body dynamics for the system state equations. The key quaternions from the spacecraft Body to Inertial frames were recorded and were used as the truth attitude reference. The true spacecraft rotation rates were also used for the rotation estima-

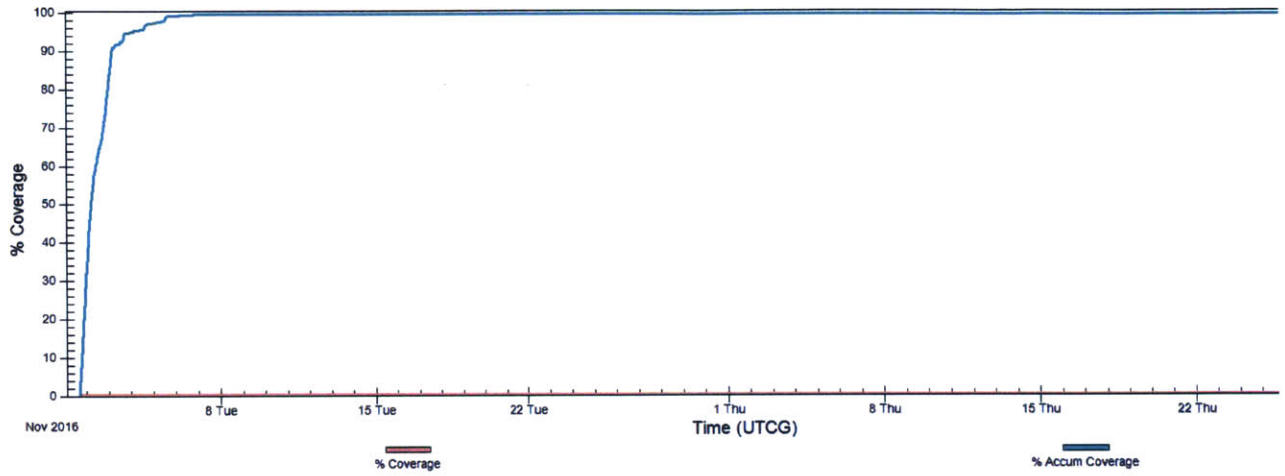

Figure 3-7: Coverage analysis shows the potential utility of a sun-synchronous orbit (SSO) for Earth sensing. For a single satellite, full accumulated global coverage is possible. This analysis used Analytical Graphics Inc.'s STK. *Image credit: W. Marlow.*

tion. The rate measurements were initialized using the truth rotation and propagated forward using the noise parameters described in Section 3.1.3. Simulation time was also used for plotting and timekeeping. All data products were gathered at a 4 Hz cadence.

3.3 Filter Design

Using the data gathered from the simulation, as discussed in Section 3.2, the data set is comprised of two of the attitude sensors: the IMU and the Magnetometer, "gathered" from the simulated spacecraft over an orbit. The unscented transformation of the Kalman Filter will be applied to this noisy data, with iterations between the data sets and the filter applications, illustrated in Figure 3-8.

3.3.1 Unscented Transformation

The unscented transformation of the Kalman Filter, is a fairly recent development in attitude estimation. It was proposed in 1997 by Juiler and Uhlmann as an alternative to the widely used EKF, and further derived for spacecraft attitude estimation in 2004 by VanDyke, Schwartz, and Hall. It was developed as a method of solving

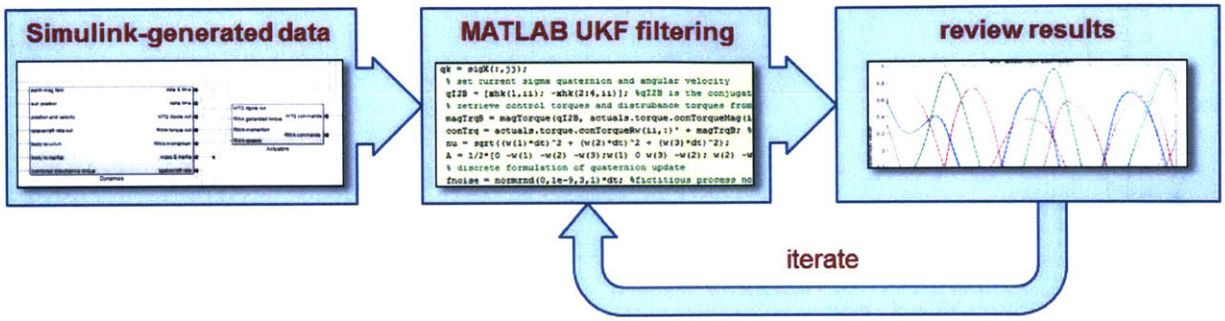

Figure 3-8: Depiction of the UKF development cycle. Data is gathered from a flight simulation in Simulink and this data is used for the filter design and tuning. *Image credit: W. Marlow.*

spacecraft estimation problems with greater accuracy than is possible with EKF on highly nonlinear systems[25, 67].

As discussed in Section 2.2.7, the EKF is an extension of the linear Kalman Filter that uses the best estimate from the previous time step to linearize the system. The linearization step from this last "best guess" is done by performing a first-order Taylor series expansion about the estimate, neglecting higher order terms[17]. It is the effect of neglecting these higher order terms that causes issue for attitude estimation schemes that require higher accuracy. According to VanDyke, *et al*,

> "The EKF accounts for nonlinearities by linearizing the system about its last-known best estimate with the assumption that the error incurred by neglecting the higher-order terms is small in comparison to the first-order terms. The Kalman Filter measurement update equations are then applied to the linear system, resulting in a suboptimal solution."

The EKF has two distinct drawbacks, one which was described by the previous quote, that the linearization step can induce errors. These errors can produce filters that are inherently unstable if the assumption that the system is locally linear fails[25]. The second major drawback, one which must be considered when designing estimators, is the implication of deriving the Jacobian matrices for the system[25]. This can be a difficult task, or numerically intensive. While the Unscented Kalman Filter (UKF) is not without its own implementation issues, namely computational complexity[67],

it is presented here as a beneficial step forward for CubeSat estimation as processing power increases for these limited platforms.

The unscented transformation takes samples from a Gaussian distribution that then have the system nonlinear function applied to them individually. An illustration of the principle is given in Figure 3-9, from Julier and Uhlmann (1997).

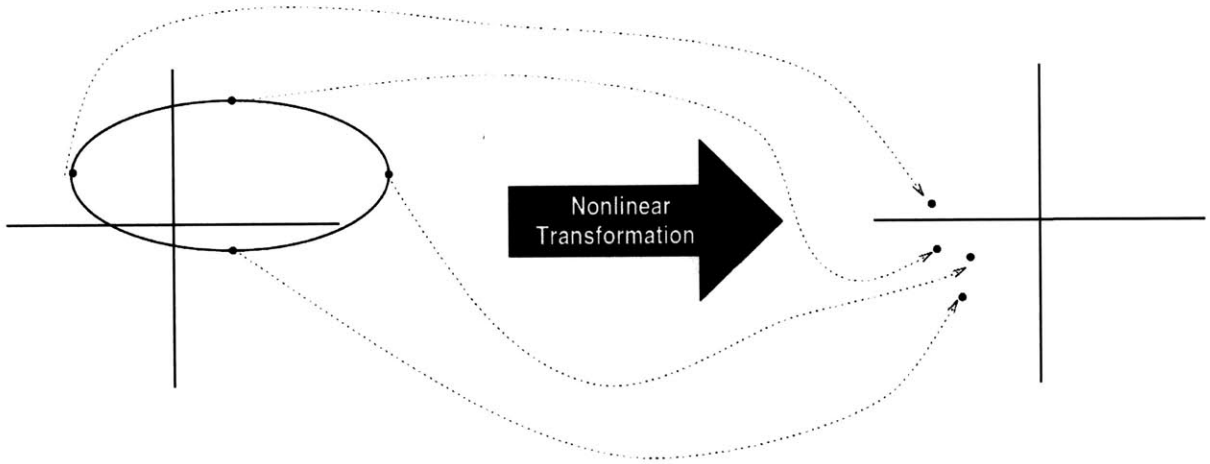

Figure 3-9: Basic principle behind the unscented transformation. Image from Julier and Uhlmann, (1997) work on UKF[25].

For whatever sample set we are estimating, we have an appropriate vector length of the random variable, $\mathbf{x}$, of size n for the appropriate attitude state and parameters[67]. A set of $2n + 1$ sample points (known as *sigma points*) is taken from a Gaussian distribution such that the mean and covariance of the untransformed set are $\bar{\mathbf{x}}$ and $\mathbf{Q_{xx}}$ respectively, which yields the following[25]:

$$\mathcal{X}_0 = \bar{\mathbf{x}} \qquad W_0 = k/(n+k) \tag{3.7}$$

$$\mathcal{X}_i = \bar{\mathbf{x}} + \left(\sqrt{(n+k)\mathbf{Q}_{xx}}\right)_i \qquad W_i = 1/2(n+k) \tag{3.8}$$

$$\mathcal{X}_{i+n} = \bar{\mathbf{x}} - \left(\sqrt{(n+k)\mathbf{Q}_{xx}}\right)_i \qquad W_{i+n} = 1/2(n+k) \tag{3.9}$$

Where:

- $k \in \mathbb{R}$ and is separate from the time notation subscript (*i.e.* x_{k+1})

- $\left(\sqrt{(n+k)\mathbf{Q}_{xx}}\right)_i$ denotes the ith row of the matrix square root of the quantity $(n+k)\mathbf{Q}_{xx}$

- Weight, W_i, for the respective ith sigma point

We then take our transformed sigma points, now denoted vector $\mathcal{Y}_i$, and we extract the new statistical properties[25],

$$\bar{\mathbf{y}} = \sum_{i=0}^{2n} W_i \mathcal{Y}_i \tag{3.10}$$

and

$$\mathbf{Q}_{yy} = \sum_{i=0}^{2n} W_i \left\{\mathcal{Y}_i - \bar{\mathbf{y}}\right\} \left\{\mathcal{Y}_i - \bar{\mathbf{y}}\right\}^T. \tag{3.11}$$

The power in the unscented transformation lies in a few crucial differences from the EKF that allow it to capture the mean and covariance of the state to second order, be numerically stable with the appropriate matrix square root method, and the value k allows the designer to adjust the estimator to work with non-Gaussian distribution populations.[25] The distribution population is assumed to be Gaussian for this work, so k is chosen appropriately[25, 67].

3.3.2 The Unscented Kalman Filter

The Unscented Kalman Filter applies the unscented transformation to the recursive process of the standard KF, and explicitly captures the cross-covariance between the state and the measurements during the state covariance update equation[25, 67]. As with the standard KF, we begin with a set of points that are propagated through the process model of the system dynamics, using Equations 3.7-3.9. However, in this original derivation by Julier and Uhlmann (1997), the number of terms in the state vector is lengthened to include the process noise terms. The state vector grows to, $\hat{\mathbf{x}}^a = \begin{pmatrix} \hat{\mathbf{x}} \\ \mathbf{v} \end{pmatrix}$ of size $n+q$, denoted n^a. The number of sigma points to propagate

becomes $2n^a + 1$ and are sampled from,[25]

$$\hat{\mathbf{x}}^a_{k|k} = \begin{pmatrix} \hat{\mathbf{x}}_{k|k} \\ \mathbf{0}_{q\times 1} \end{pmatrix} \quad \text{and} \quad \mathbf{P}^a_{k|k} = \begin{vmatrix} \mathbf{P}_{k|k} & \mathbf{P}_{xy(k|k)} \\ \mathbf{P}_{xy(k|k)} & \mathbf{Q}_k \end{vmatrix} \tag{3.12}$$

The Kalman filter is then formulated according to the following steps,[25]

1. The sigma points are processed through the state equations,

$$\mathcal{X}_{i(k+1|k)} = \mathbf{f}\left[\mathcal{X}^a_{i(k|k)}, \mathbf{u}_k, k\right] \tag{3.13}$$

2. The predicted mean of the state is the weighted sum of the transformed points

$$\hat{\mathbf{x}}_{k+1|k} = \sum_{i=0}^{2n} W_i \mathcal{X}_{i(k+1|k)} \tag{3.14}$$

3. The predicted state covariance uses the transformed set and the predicted mean

$$\mathbf{Q}_{xx(k+1|k)} = \sum_{i=0}^{2n} W_i \left\{\mathcal{X}_{i(k+1|k)} - \hat{\mathbf{x}}_{k+1|k}\right\}\left\{\mathcal{X}_{i(k+1|k)} - \hat{\mathbf{x}}_{k+1|k}\right\}^T \tag{3.15}$$

4. The sigma points are propagated through the measurement model equations using

$$\mathcal{Y}_{i(k+1|k)} = \mathbf{h}\left[\mathcal{X}_{i(k|k)}, \mathbf{u}_k, k\right] \tag{3.16}$$

5. Similarly, the prediction of the mean of the measurements is

$$\hat{\mathbf{y}}_{k+1|k} = \sum_{i=0}^{2n} W_i \mathcal{Y}_{i(k+1|k)} \tag{3.17}$$

6. Now the covariance of the innovation, using the measurement noise covariance $\mathbf{R}$, is

$$\mathbf{Q}_{yy(k+1|k)} = \sum_{i=0}^{2n} W_i \left\{\mathcal{Y}_{i(k+1|k)} - \hat{\mathbf{y}}_{k+1|k}\right\}\left\{\mathcal{Y}_{i(k+1|k)} - \hat{\mathbf{y}}_{k+1|k}\right\}^T + \mathbf{R} \tag{3.18}$$

7. Next, the system cross-covariance is needed for the UKF calculation of the Kalman gain,

$$\mathbf{Q}_{xy(k+1|k)} = \sum_{i=0}^{2n} W_i \left\{ \mathcal{X}_{i(k+1|k)} - \hat{\mathbf{x}}_{k+1|k} \right\} \left\{ \mathcal{Y}_{i(k+1|k)} - \hat{\mathbf{y}}_{k+1|k} \right\}^T \tag{3.19}$$

8. The final step is to utilize the newly derived covariance matrices for the calculation of the Kalman gain,

$$\mathbf{K}_k = \mathbf{Q}_{xy(k+1|k)} \mathbf{Q}^{-1}_{yy(k+1|k)} \tag{3.20}$$

It is clear that as the number of variables and noise parameters grows, the computational loading to propagate the sigma points scales according to $2n^a + 1$. However, taking advantage of some assumptions that can be made about the process and measurement noise, the size of the state vector can be reduced by the number of noise parameters being estimated. This yields a more efficient derivation of the UKF, a useful modification for processor-limited CubeSat avionics platforms.

3.3.3 Efficient UKF Derivation

The variance in the IMU and Magnetometer measurements assumed zero-mean, or additive Gaussian, noise for the UKF developed in this work. The process noise was also assumed to be white Gaussian. In work by VanDyke, *et al.* (2004), these assumptions of additive noise allow the state vector to be decoupled from the estimation of the process or measurement parameters. This decreases the number of sigma points from $2n^a + 1$ to $2n + 1$[67], and requires a reformulation of the weighting parameters and their uses within the filter. We deem this the 'Efficient EKF' for state estimation. It is derived as follows.[67, 68]

1. The filter is initialized by sampling from the predicted statistics of the state only,

$$\hat{\mathbf{x}}_{k-1|k-1} = \mathbf{x}_0 \quad \textit{and} \quad \mathbf{Q}_{xx(k-1|k-1)} = \mathbf{Q}_0 \tag{3.21}$$

2. The sigma points are calculated according to,

$$\mathcal{X}_{0(k-1|k-1)} = \hat{\mathbf{x}}_{(k-1|k-1)} \tag{3.22}$$

$$\mathcal{X}_{i(k-1|k-1)} = \hat{\mathbf{x}}_{(k-1|k-1)} + \left(\sqrt{(n+\lambda)\mathbf{Q}_{xx(k-1|k-1)}}\right)_i \quad \text{for} \quad i = 1, ..., n \tag{3.23}$$

$$\mathcal{X}_{i(k-1|k-1)} = \hat{\mathbf{x}}_{(k-1|k-1)} - \left(\sqrt{(n+\lambda)\mathbf{Q}_{xx(k-1|k-1)}}\right)_i \quad \text{for} \quad i = n+1, ..., 2n \tag{3.24}$$

where $\lambda = \alpha^2(n+k) - n$. The new term α is used to determine the spread of the sigma points and is typically set between $10^{-4} \leq \alpha \leq 1$. [68]

3. The sigma points are propagated through the system model as before

4. The *a priori* state estimate and covariance are calculated using new weighting parameters. Borrowing the notation from Vinther, *et al.* (2011), these new parameters are $W^{(m)}$ for the state and $W^{(c)}$ for the covariance,

$$\mathbf{x}_{(k|k-1)} = \sum_{i=0}^{2n} W_i^{(m)} \mathcal{X}_{i(k|k-1)} \tag{3.25}$$

and

$$\mathbf{Q}_{xx(k|k-1)} = \sum_{i=0}^{2n} W_i^{(c)} \left\{\mathcal{X}_{i(k|k-1)} - \mathbf{x}_{(k|k-1)}\right\} \left\{\mathcal{X}_{i(k|k-1)} - \mathbf{x}_{(k|k-1)}\right\}^T + \mathbf{W}_k \tag{3.26}$$

where $\mathbf{W}$ is the process noise covariance matrix. The weights are calculated as,

$$W_0^{(m)} = \lambda/(n+\lambda) \tag{3.27}$$

$$W_0^{(c)} = \lambda/(n+\lambda) + \left(1 - \alpha^2 + \beta\right) \tag{3.28}$$

and

$$W_i^{(m)} = W_i^{(c)} = 1/(2(n+\lambda)) \quad \text{for} \quad i = 1, ..., 2n \tag{3.29}$$

here β is set to 2 for a Gaussian distribution[68].

5. As before, the sigma points are propagated through the sensor model equations

6. The new measurement vector is found with the state weighting parameter

$$\hat{\mathbf{y}}_{k|k-1} = \sum_{i=0}^{2n} W_i^{(m)} \mathcal{Y}_{i(k|k-1)} \tag{3.30}$$

7. The measurement and state-measurement cross-covariance matrices are calculated as before, only using $W^{(c)}$ in place of W.

8. Finally, the *a posteriori* state estimate, the error covariance, and the Kalman gain can be calculated according to

$$\hat{\mathbf{x}}_{k|k} = \hat{\mathbf{x}}_{k|k-1} + \mathbf{K}_{xx(k)} \left(\hat{\mathbf{y}}_k - \hat{\mathbf{y}}_{k|k-1} \right) \tag{3.31}$$

$$\mathbf{Q}_{xx(k|k)} = \mathbf{Q}_{xx(k|k-1)} - \mathbf{K}_k \mathbf{Q}_{yy(k)} \mathbf{K}_k^T \tag{3.32}$$

where the Kalman gain is then

$$\mathbf{K}_k = \mathbf{Q}_{xy(k)} \mathbf{Q}_{yy(k)}^{-1} \tag{3.33}$$

3.3.4 Application of the Efficient UKF

To develop and apply the Efficient UKF, the spacecraft were assumed to obey standard rigid body dynamics. This allows for the derivation of kinematic differential equations using the body rates, Euler angles, and the quaternion attitude representation. A diagram of the 3U spacecraft model displaying a 3-2-1 Euler angle rotation is shown in Figure 3-10. The Efficient UKF was applied to the quaternion state for estimation. The rigid body dynamics, solved for the angular acceleration as has been represented in previous works[48, 68], are

$$\dot{\omega} = \mathbf{I}_{sat}^{-1} \left(-\Phi_3(\omega) \mathbf{I}_{sat} \omega + \tau_{control} + \tau_{disturbance} \right) \tag{3.34}$$

where $\Phi(\omega)$ is the skew symmetric cross-product matrix of the vector ω. For the 3-element angular velocity vector this becomes

$$\Phi_3(\omega) = \begin{bmatrix} 0 & -\omega_3 & \omega_2 \\ \omega_3 & 0 & -\omega_1 \\ -\omega_2 & \omega_1 & 0 \end{bmatrix}. \tag{3.35}$$

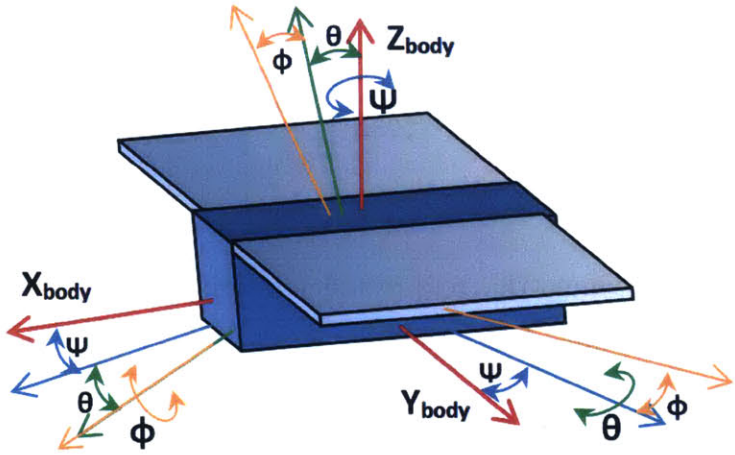

Figure 3-10: The standard Euler angle representation for a 3-2-1 (ϕ about +Z, θ about +Y, and ψ about +X) transformation is shown with respect to the spacecraft body frame. *Image credit: W. Marlow.*

The state vector is defined as the quaternion from the *body* to *inertial* frames, denoted as q_{B2I},

$$\mathbf{x} = q_{B2I} \equiv q = \begin{pmatrix} q_0 \\ q_1 \\ q_2 \\ q_3 \end{pmatrix} \tag{3.36}$$

where q_0 is the scalar portion and $[q_1\ q_2\ q_3]$ is the vector portion of q_{B2I}. The measurement equations used the spacecraft Euler angles, which are measured by integrating the spacecraft angular rates at a specified time interval of $dt = 0.25$ seconds and relating this rigid body motion to q_{B2I}, thus

$$\mathbf{y} = \begin{pmatrix} \psi \\ \theta \\ \phi \end{pmatrix} \tag{3.37}$$

Through differentiation of the directional cosine matrix for the widely used Euler 3-2-1 angle set, the spacecraft angular rates can be used in the formulation of the quaternion kinematic differential equation[56].

$$\dot{\mathbf{x}} = \dot{q} = \frac{1}{2} q_{B2I} \begin{pmatrix} 0 \\ \omega_x \\ \omega_y \\ \omega_z \end{pmatrix} \tag{3.38}$$

Expanding the skew-symmetric cross-product matrix to four dimensions, $\mathbf{\Phi}_4(\omega)$, the quaternion kinematic differential equation is then,

$$\dot{\mathbf{x}} = \frac{1}{2} \begin{bmatrix} 0 & -\omega_3 & -\omega_2 & -\omega_3 \\ \omega_3 & 0 & \omega_3 & -\omega_2 \\ \omega_2 & -\omega_3 & 0 & \omega_1 \\ \omega_3 & \omega_2 & -\omega_1 & 0 \end{bmatrix} \begin{pmatrix} q_0 \\ q_1 \\ q_2 \\ q_3 \end{pmatrix} \tag{3.39}$$

and converted to the discrete state update equation, $\mathbf{F}$, we see the highly nonlinear state equation[75], using $\omega = E[\omega]$,

$$q_{k+1} = \mathbf{F}(\mathbf{x}_k) \cdot q_k = \left(\cos(\frac{\nu}{2}) I_4 \ + \frac{\sin(\frac{\nu}{2})}{\frac{\nu}{2}} \mathbf{\Phi}_4(\omega) \cdot dt \right) \cdot q_k + w_k \tag{3.40}$$

where

$$\nu \equiv \sqrt{(\omega_x dt)^2 + (\omega_y dt)^2 + (\omega_z dt)^2} \tag{3.41}$$

and $\mathbf{I}_4$ is the 4×4 identity matrix.

Additionally, we must also reformulate the process noise calculation and the state covariance to suit the four-element quaternion formulation.[75] The process noise term for the discrete state update equation, denoted w, includes the noise portions of the

angular rate vector, denoted by ω_{ni},

$$w \equiv \frac{1}{2}\begin{bmatrix} -q_1 & -q_2 & -q_3 \\ q_0 & -q_3 & -q_2 \\ q_3 & q_0 & -q_1 \\ -q_2 & q_1 & q_0 \end{bmatrix}\begin{pmatrix} \omega_{nx} \\ \omega_{ny} \\ \omega_{nz} \end{pmatrix} \tag{3.42}$$

and the process covariance is a function of the state and the angular rate variance[75],

$$W = \frac{1}{4}\begin{bmatrix} -q_1 & -q_2 & -q_3 \\ q_0 & -q_3 & -q_2 \\ q_3 & q_0 & -q_1 \\ -q_2 & q_1 & q_0 \end{bmatrix}\begin{bmatrix} \sigma^2_{\omega_x} & 0 & 0 \\ 0 & \sigma^2_{\omega_y} & 0 \\ 0 & 0 & \sigma^2_{\omega_z} \end{bmatrix}\begin{bmatrix} -q_1 & -q_2 & -q_3 \\ q_0 & -q_3 & -q_2 \\ q_3 & q_0 & -q_1 \\ -q_2 & q_1 & q_0 \end{bmatrix}^T \tag{3.43}$$

Finally, to retrieve the spacecraft orientation in the original, intuitive Euler angle formulation, we must propagate the sigma points through the measurement equation for the Euler 3-2-1 set seen in Equation 3.37, $\mathbf{H}$, with inverse trigonometric functions[56, 75],

$$\mathbf{H}(\mathbf{x}_k) = \begin{pmatrix} \tan^{-1}\frac{2(q_1q_2+q_0q_3)}{q_0^2+q_1^2-q_2^2-q_3^2} \\ \sin^{-1}2(q_0q_2 - q_1q_3) \\ \tan^{-1}\frac{2(q_2q_3-q_0q_1)}{q_0^2-q_1^2-q_2^2+q_3^2} \end{pmatrix} \tag{3.44}$$

The performance of the application of the Efficient UKF with the formulated kinematic equations to the spacecraft data is presented in Chapter 4 in Sections 4.3 and 4.4. The results are presented by spacecraft bus type and by orbit.

Chapter 4

Analysis and Results

4.1 Overview

The Unscented Kalman Filter design that was presented and developed in Chapter 3 was applied to data collected from the system models for sets of 3U and 6U CubeSat missions. The results of the filter application are discussed in this chapter. We present results for the 3U bus missions first for the three different orbits defined in Chapter 3. These are followed by the results for the larger 6U bus and its respective three orbits. A discussion about the overall filter performance and potential improvements are presented last.

Previous Iterations of the EKF and Differences with the UKF Development Results

Previous CubeSat attitude estimation work in the MIT SSL has been in the development and testing of Extended Kalman Filters for CubeSat attitude estimation and control[48, 73]. These works developed quaternion-based attitude and spacecraft rate estimation. The UKF estimator developed in this thesis provides a body of work to be as direct of a comparison with the EKF performance from the previous programs as possible. Therefore,the UKF was also designed for quaternion estimation. We also highlight the differences in the filter implementations.

The Extended Kalman Filters are executed within the larger simulation environ-

ment. This code environment is a combination of MATLAB functions and scripts, Simulink models, and flight-like C-code that can run natively on a typical CubeSat microcontroller or microprocessor. Since this code base is much more mature than the UKF development, the EKF results contain sensor fusion and filtering of the full set of attitude sensors, with the exception of star trackers. The inclusion of star tracker input is an item for future work.

The UKF results seen in Sections 4.3 and 4.4 are from a code base that exists solely as an algorithm development tool. The UKF development was done in MATLAB using spacecraft rotation rate and quaternion data products as 'truth' sources from the more detailed mission simulator code.

The filter parameters used for most of the 3U and 6U spacecraft were:

$k = 2$	$\alpha = 1 \times 10^{-3}$	$\beta = 2$ (assuming Gaussian)

Parameters for any specifically-tuned filters are described for those cases. The effects of changing α and k on filter performance are presented in more detail in Section 4.4.4.

4.2 Filter Performance Metrics

The presentation of the quaternion estimation performance for the EKF and UKF is given here in several forms. The first is the classical presentation of the error of the individual quaternion elements. This gives the reader a sense of the error evolution over time for each of the quaternion components. The second is the the root sum square (RSS) error of the quaternion error. The true quaternion defining the rotation from Body to Inertial frames is compared unit-wise against the estimated quaternion of the same rotation. The RSS difference between the four element quaternion attitude representations is then,

$$q_{RSS} = \sqrt{(q_{0t} - q_{0e})^2 + (q_{1t} - q_{1e})^2 + (q_{2t} - q_{2e})^2 + (q_{3t} - q_{3e})^2} \tag{4.1}$$

where q_{it} is the ith element of the true quaternion, and q_{ie} is the ith element of the estimated quaternion. This is different than the physical representation of the difference of two quaternions being the rotational difference between them. This metric allows for direct inspection of the overall quaternion accuracy between the EKF and the UKF, which is presented as a separate graph for each of the cases, labeled *Superimposed RSS Quaternion Estimation Error.* The final presentation of the accuracy of the filters is the direct inspection of the Euler angle errors. These are presented individually for ϕ, θ, and ψ. Different succinct methods of filter performance have been used by previous authors on the subject. Julier and Uhlmann (1997) present their findings with the mean squared errors of an EKF and UKF, while VanDyke, *et al.*, (2004) present in a percent error format.

4.3 Filter Performance Values for 3U Bus

As described in Chapters 2 and 3, the 3U bus configuration includes a variety of attitude sensors in the overall simulation; we use the output from a small subset in this work. The 3U bus was equipped with the ADCS all-in-one BCT XACT system (see Table 1.2 for a listing of the capabilities of the BCT XACT and the MAI-400 units). Though the actuators are different between the two systems, the performance parameters of the IMU and MTM were assumed consistent between the two different buses. This assumption is asserted through previous avionics designs from the MIT SSL and STAR Lab that have included the IMU and MTM in the avionics hardware, separate from the attitude control unit internal electronics.

4.3.1 ISS Orbit

The spacecraft body rates for the specific simulation case are shown in Figure 4-1. These rates are referenced throughout the results of this orbit simulation and estimation.

The body rates shown in all figures for the 3U spacecraft have several elements in common. The angular rates are the result of the initial random tipoff rate from

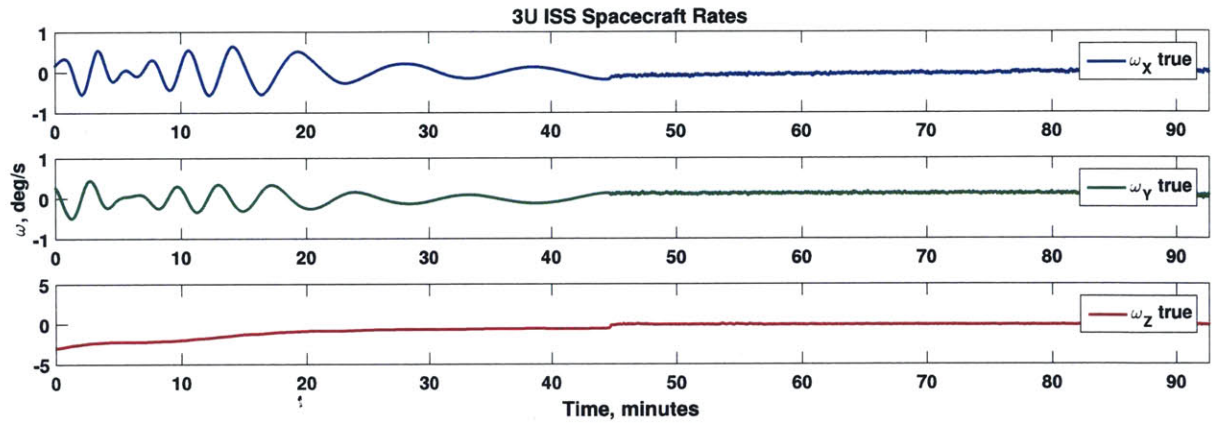

Figure 4-1: 3U ISS spacecraft body rates. *Image credit: W. Marlow.*

being 'deployed'. This tipoff rate is generated independently for each axis according to a $\pm$ 10 degree/s (3-σ) distribution,

$$\omega_i \sim \mathcal{N}(0, 10/3\ deg/s) \tag{4.2}$$

The UKF quaternion estimation error for the 3U ISS mission is shown in Figure 4-2. The RSS presentation is shown in Figure 4-3. The UKF performance for this simulation was improved over the entire orbit when compared to the EKF. Although some transient error growth can be seen in the later portions of Figure 4-2, the sizes of these errors are still two to three orders of magnitude smaller than the errors seen in the EKF at the beginning of the orbit.

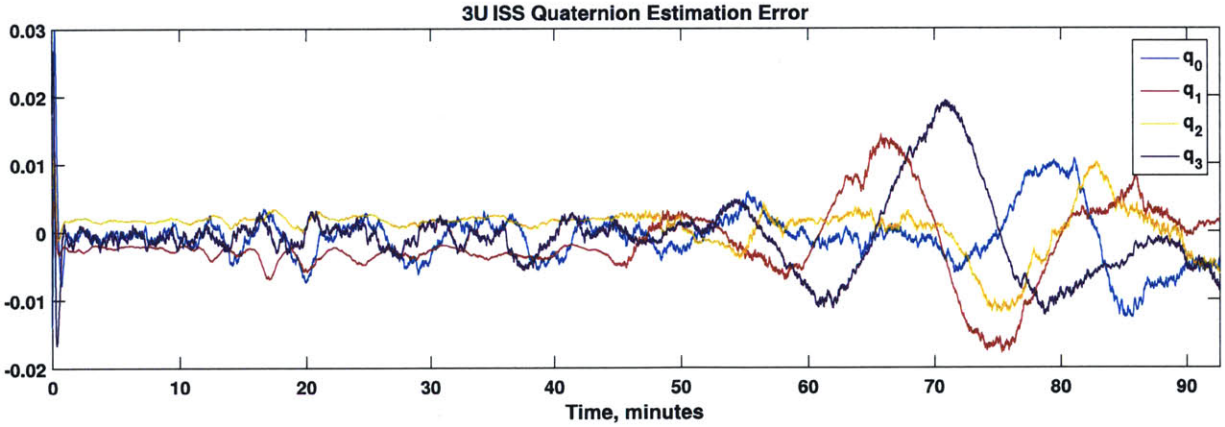

Figure 4-2: Plot of the 3U ISS orbit spacecraft UKF quaternion element estimation error. *Image credit: W. Marlow.*

The spacecraft body rates for two of the axes are relatively low (below about ± 1 deg/s initially), but the impact of the the higher Z axis rate can be seen on the EKF performance early in the orbit. The linearization errors (see Equations 3.40 and 3.41) required for the operations of the EKF likely become dominant contributors at higher rates.

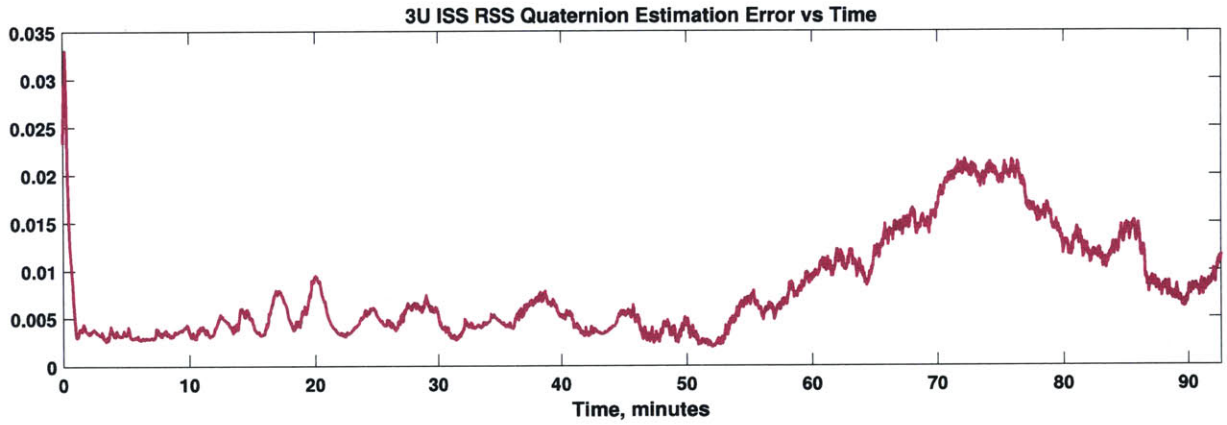

Figure 4-3: Plot of the 3U ISS orbit spacecraft UKF RSS quaternion estimation error. *Image credit: W. Marlow.*

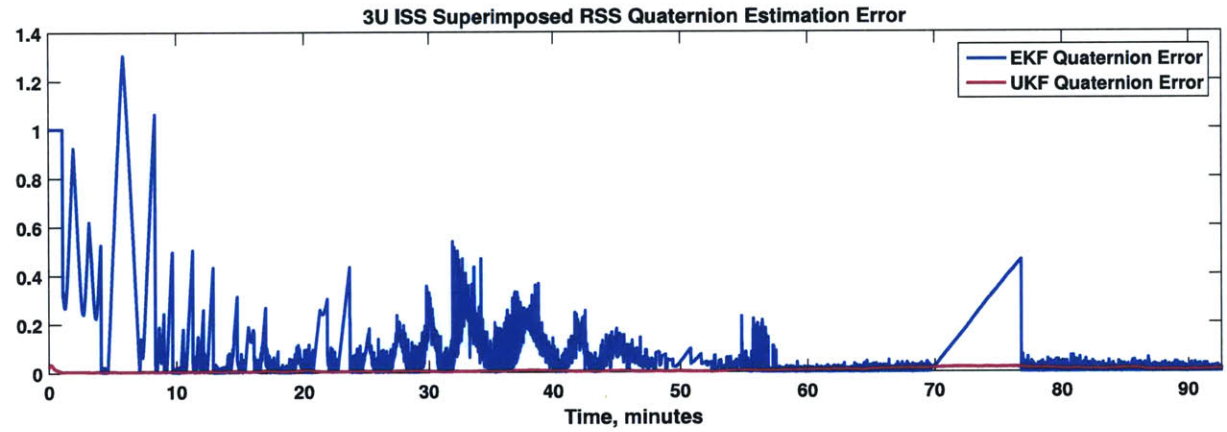

Figure 4-4: Combined plots of the ISS orbit 3U EKF and UKF RSS quaternion estimation errors. *Image credit: W. Marlow*

For this scenario, the UKF starts with a non-zero error and is able to quickly drive down the error magnitude and maintain superior performance over the EKF throughout the orbit. To give a clearer picture of the evolution of the Euler angle error over time, the errors for the three Euler angles are presented in Figure 4-5. The

UKF maintains a maximum error in each of the three axis to at or below about two degrees absolute value.

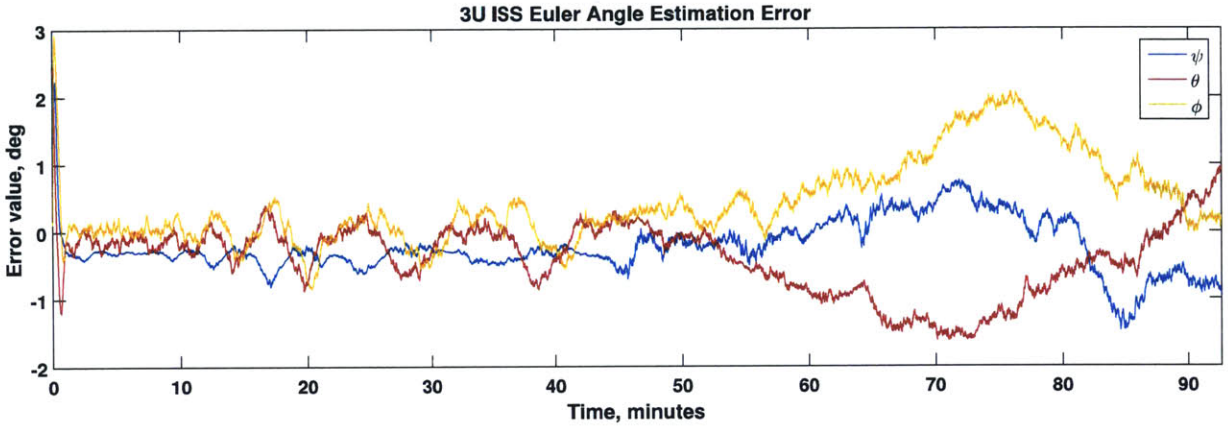

Figure 4-5: Combined plot of 3U ISS orbit UKF individual Euler angle errors. *Image credit: W. Marlow.*

A summary of the filter performances over the entire orbit are presented in Table 4.1. To highlight the performance of the UKF in the nonlinear, higher angular rate regime, Table 4.2 is provided. This displays the error statistics for the first 45 minutes of the orbit (see Figure 4-1 for the spacecraft rates for this orbit).

Overall performance comparison and summary		
Filter	μ_{total}	σ_{total}
EKF	11.90°	21.28°
UKF	0.42°	0.59°

Table 4.1: 3U ISS performance summary.

t<45 minutes performance comparison and summary		
Filter	μ_{total}	σ_{total}
EKF	17.64°	38.87°
UKF	0.11°	0.10°

Table 4.2: 3U ISS performance summary for higher rate tumbling.

Over the entire orbit, the UKF reduced the mean of the estimation error by about

96% with a 97% improvement in error variance over the EKF. During the higher rates, the UKF reduced the mean error by over two orders of magnitude, though still two times larger than the desired 0.05° accuracy. There was an even higher reduction in the error variance as compared the EKF in this region.

4.3.2 Sun-synchronous Orbit

The UKF allowed general improvement over the EKF for the SSO orbit, though not as successful as with the ISS orbit. The overall EKF and UKF performance error is being dominated by rate estimation errors introduced when the measured body rates spike near 55 minutes into the orbit. This was a product of the simulation data that can be seen affecting both filters. There is no obvious body rate increase or sudden change in that time period in Figure 4-6.

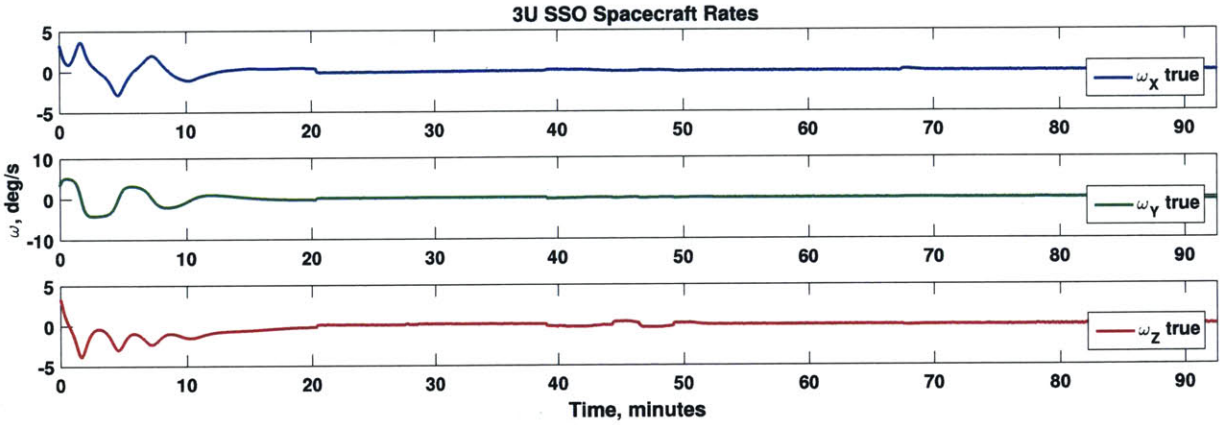

Figure 4-6: 3U SSO spacecraft body rates. *Image credit: W. Marlow.*

The element-wise quaternion estimation error is shown in Figure 4-7. Here, there is an initial bout of error before about ten minutes, on par with the EKF error, as can be seen in Figure 4-9.

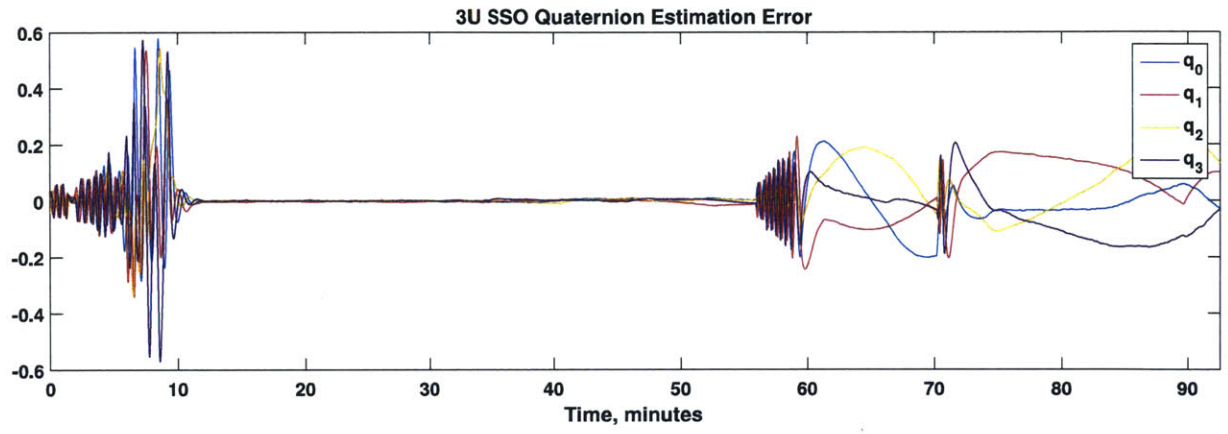

Figure 4-7: Plot of the 3U SSO spacecraft UKF quaternion element estimation error. *Image credit: W. Marlow.*

It can be seen that after the filter has compensated for the initial error, the attitude estimation is superior to the EKF until the rate error is introduced at 55 minutes. At this point, both filters seem to perform similarly, although the UKF RSS quaternion error is more constant over the remainder of the orbit.

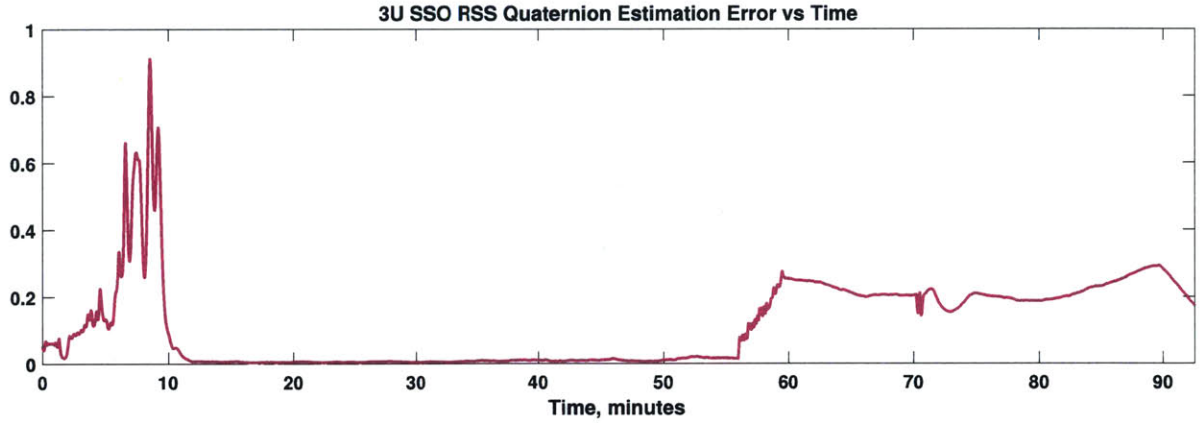

Figure 4-8: Plot of the 3U SSO spacecraft UKF RSS quaternion estimation error. *Image credit: W. Marlow.*

For the first fifteen minutes of the sun-synchronous orbit, the spacecraft rates are still high enough to have the UKF performance improve the quaternion estimation relative the the EKF.

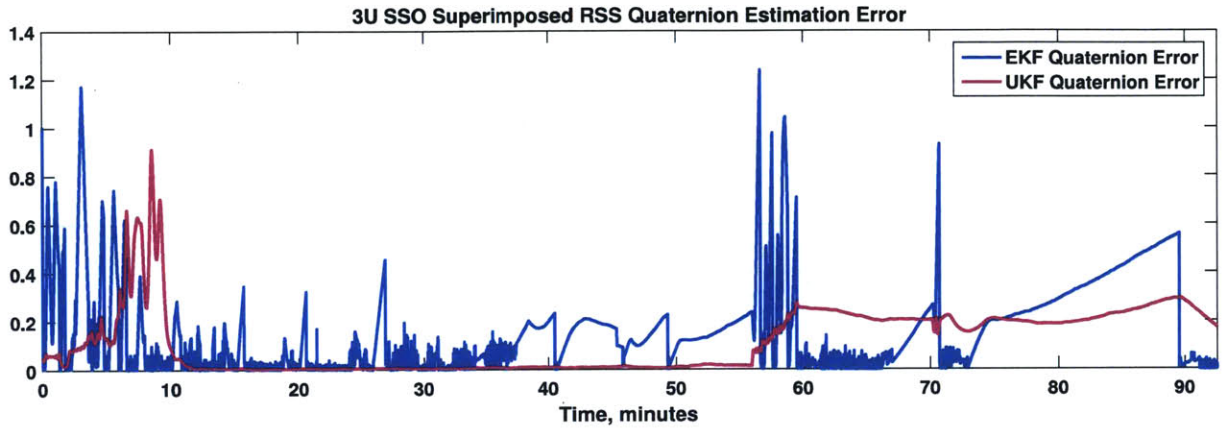

Figure 4-9: Combined plots of the 3U SSO spacecraft EKF and UKF RSS quaternion estimation errors. *Image credit: W. Marlow*

The Euler angle estimation errors are provided in Figure 4-10. Despite the spikes in attitude error during slow rotations, the UKF provided overall marked improvement over the EKF.

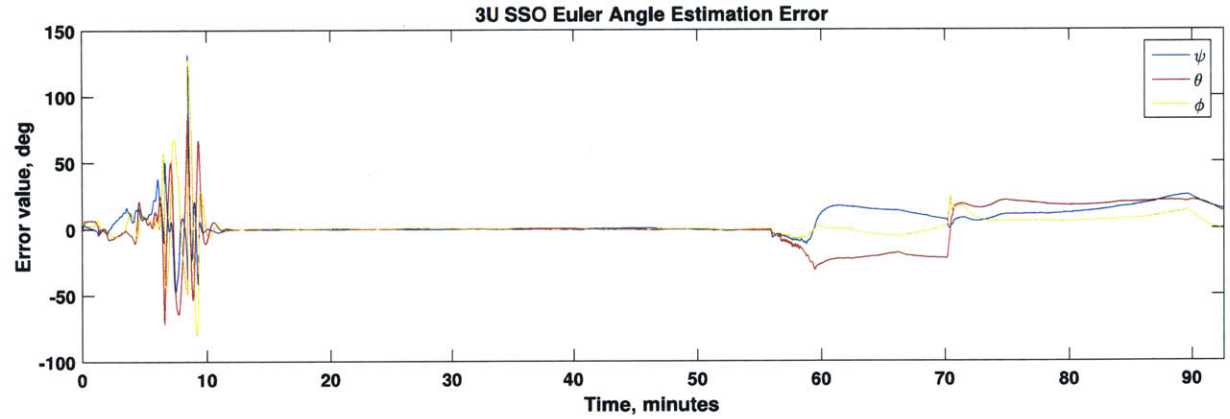

Figure 4-10: Combined plot of 3U SSO spacecraft UKF individual Euler angle errors. *Image credit: W. Marlow.*

A summary of the filter performances over the entire orbit are presented in Table 4.3. Table 4.4 displays the error statistics for the first fifteen minutes of the orbit (see Figure 4-6 for the spacecraft rates for this orbit).

Overall performance comparison and summary		
Filter	μ_{total}	σ_{total}
EKF	-8.19°	34.11°
UKF	-0.13°	0.51°

Table 4.3: 3U SSO performance summary.

t<15 minutes performance comparison and summary		
Filter	μ_{total}	σ_{total}
EKF	-47.86°	70.30°
UKF	-2.90°	5.45°

Table 4.4: 3U SSO performance summary for higher rate tumbling.

The performance of the UKF with respect to the ISS orbit was less successful overall. However, the UKF reduced the mean of the estimation error (using absolute values) by about 98% with a similarly large reduction in variance versus the EKF for the full orbit statistics. During the higher rates in the first 15 minutes of the orbit, the UKF reduced the mean error by 94% with a 92% reduction in the error variance. The absolute values of the mean error and variance are several orders of magnitude more than the desired performance for a lasercomm mission with body-pointing only.

4.3.3 800 km Orbit

Both the UKF and EKF estimators performed well in the 800 km high LEO orbit. After an initial detumble period and slowing of the body rates, the EKF was able to drive the overall quaternion and Euler angle error down to levels that are on par with the performance of this iteration of the UKF. Further improvement and tuning is required for this implementation to try to drive the errors down further. The spacecraft rates for this orbit are provided in Figure 4-11.

Figures 4-12 and 4-13 show the quaternion error by element and by RSS value, respectively. Although some error begins to oscillate at about 45 minutes, the mag-

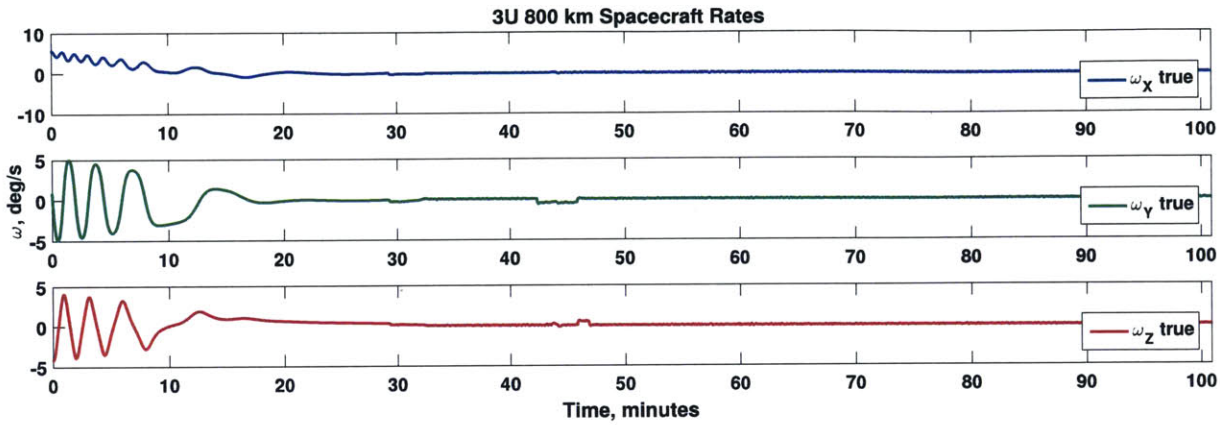

Figure 4-11: 3U 800 km orbit spacecraft body rates. *Image credit: W. Marlow.*

nitude of these errors are each still less than about 5% of the unit quaternion value. The UKF estimation maintained strong performance throughout the orbit.

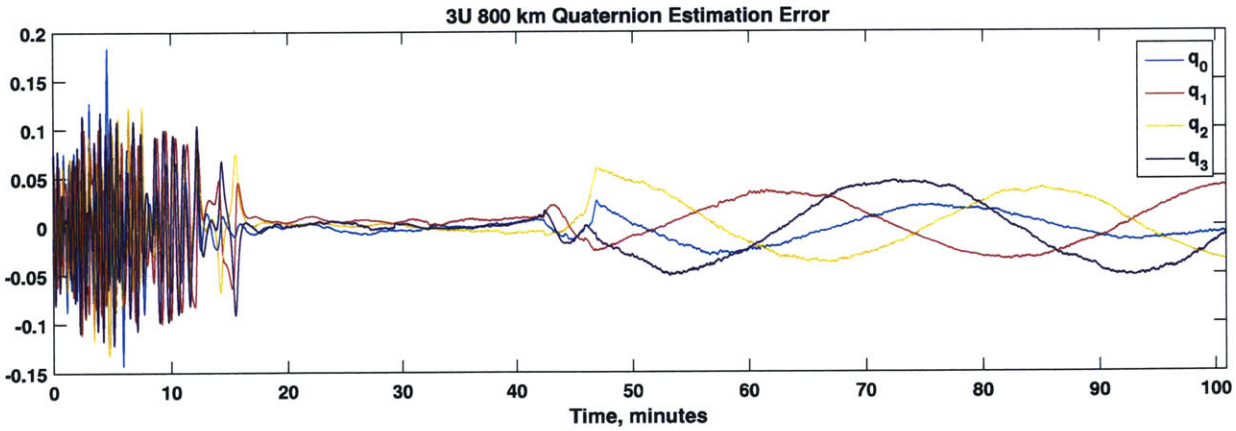

Figure 4-12: Plot of the 3U 800 km orbit spacecraft UKF quaternion element estimation error. *Image credit: W. Marlow.*

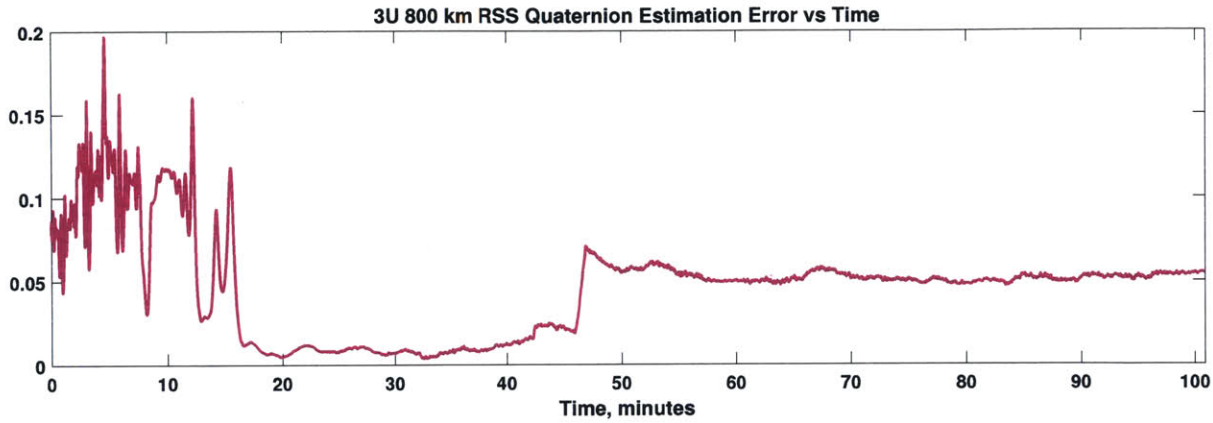

Figure 4-13: Plot of the 3U 800 km orbit spacecraft UKF RSS quaternion estimation error. *Image credit: W. Marlow.*

The impact of rate bias correction by the EKF can be seen quite dramatically in Figure 4-14. Up until the rotation rate correction point near 30 minutes, the UKF outperforms the EKF in total quaternion error.

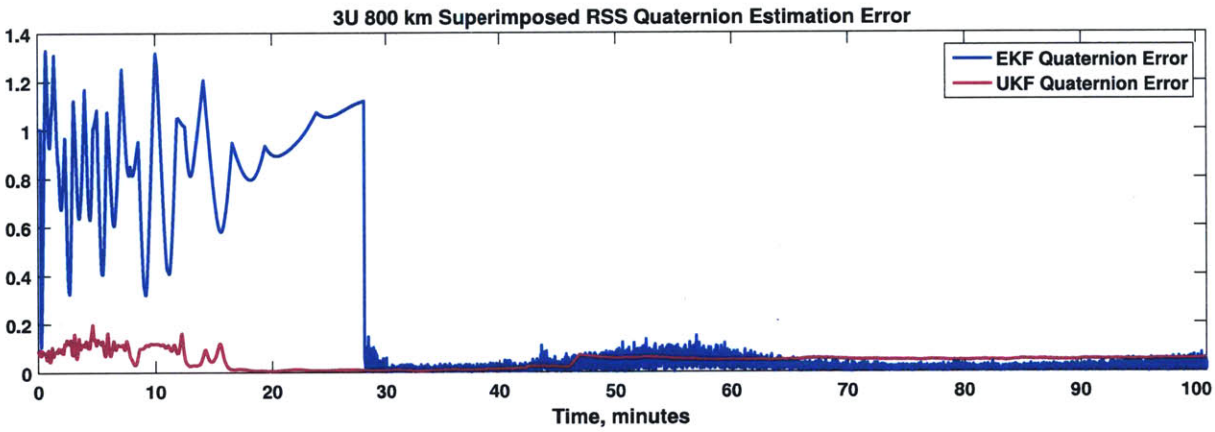

Figure 4-14: Combined plots of the 3u 800 km orbit spacecraft EKF and UKF RSS quaternion estimation errors. *Image credit: W. Marlow*

The Euler angle estimation errors are provided in Figure 4-15. Some error growth can be seen after about 45 minutes, when the quaternion error jumps. This is attributed to the sudden change is body rates that are present in the Y and Z axes, in Figure 4-11. The estimator seemingly could not recover from this in a timely manner, suggesting that further improvement is needed for scenarios like this.

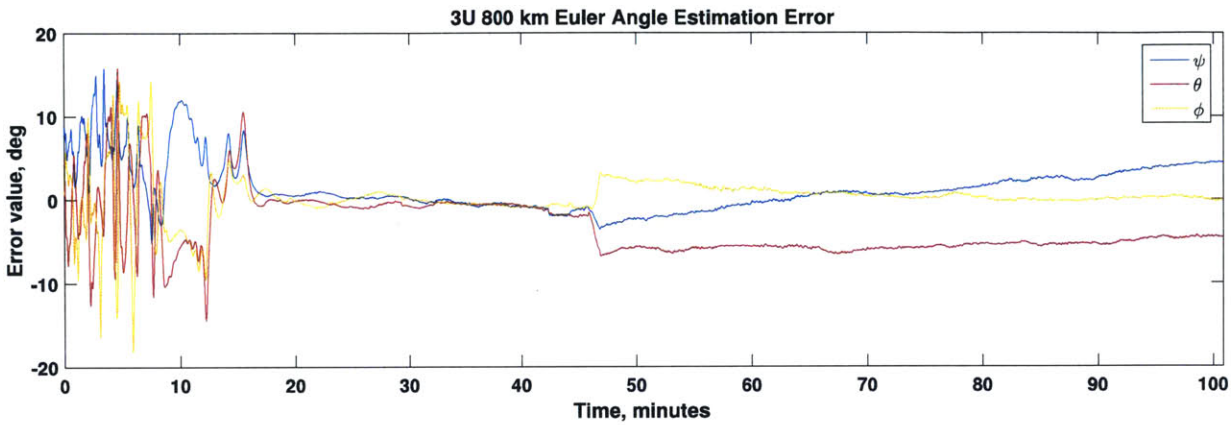

Figure 4-15: Combined plot of 3U 800 km orbit spacecraft UKF individual Euler angle errors. *Image credit: W. Marlow.*

A summary of the filter performances over the 800 km altitude orbit are presented in Table 4.5. Table 4.6 displays the error statistics for the first 22 minutes of the orbit, where the rates are highest (see Figure 4-11 for the spacecraft rates for this orbit).

Overall performance comparison and summary		
Filter	μ_{total}	σ_{total}
EKF	-0.34°	3.48°
UKF	0.78°	2.26°

Table 4.5: 3U 800 km performance summary.

t<22 minutes performance comparison and summary		
Filter	μ_{total}	σ_{total}
EKF	-12.05°	20.52°
UKF	-0.06°	0.53°

Table 4.6: 3U 800 km performance summary for higher rate tumbling.

The UKF could not improve upon the EKF for the full orbit profile. The UKF mean error was about of the same magnitude, with only a slight improvement in error variance versus the EKF. During the higher rates, the UKF was able to improve upon the EKF performance significantly. There was over two orders of magnitude in mean

error improvement, reaching very near the desired 0.05° attitude estimation error. The filter was able to drive down the error variance by 97%.

4.4 Filter Performance Values for 6U Bus

In Chapters 2 and 3, the 6U bus configuration was presented. The bus is modeled containing a variety of attitude sensors in the overall simulation. A subset of those sensors were used in this work. The 6U bus was equipped with the ADCS all-in-one MAI-400 system (see Table 1.2) to examine the impact of lower control authority on the higher inertia bus.

The tipoff rates of the 6U were all initiated at 5-10 degrees per second on each axis. Since the larger spacecraft has slightly lower actuator torque using the MAI-400, the high tipoff rates continued for longer into the orbits during detumble. This exercised the estimators for longer periods of time in a more mathematically strenuous environment where the nonlinear improvements of the UKF over the KF and EKF could be better showcased.

Regarding the performance results for all of the 6U cases, there are sections in the early orbit operations where the quaternion and Euler angle error are elevated relative to the 3U cases. Given the higher tipoff rates, the overall filter performance is still improved over the EKF with these moderate increases in error. In future work for the filter, we will investigate the use of a control system and measurement cadence with a higher bandwidth. Finer time resolution during the higher body rate motion should help drive these estimation errors down further.

4.4.1 ISS Orbit

Presented here are figures for estimation of the 6U spacecraft attitude in the ISS orbit. The spacecraft rates are provided for reference in Figure 4-16.

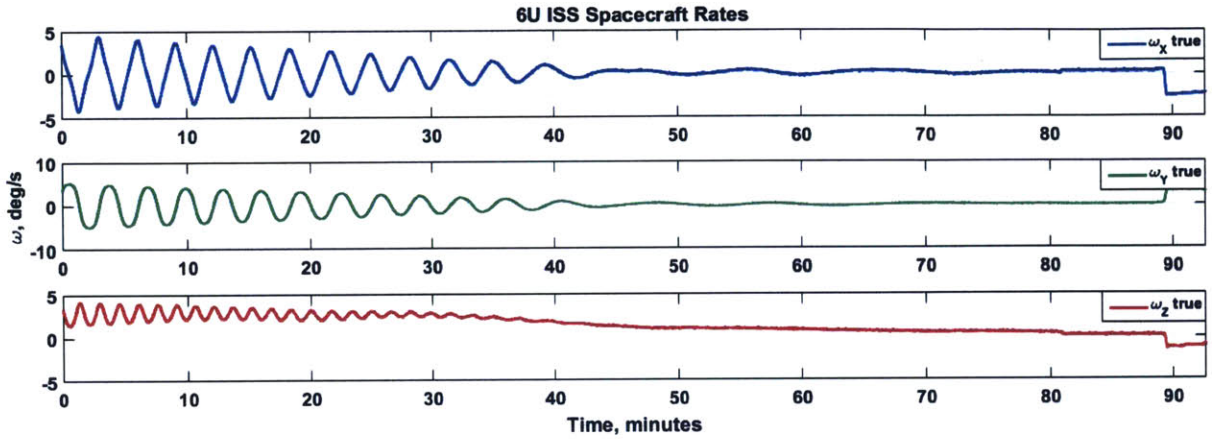

Figure 4-16: 6U ISS spacecraft body rates. *Image credit: W. Marlow.*

In general, the UKF did not perform better than the respective 3U case. However, the quaternion error is kept low for a majority of the orbit, seen in Figures 4-17 and 4-18. This level of performance is still superior to the EKF for the full mission profile.

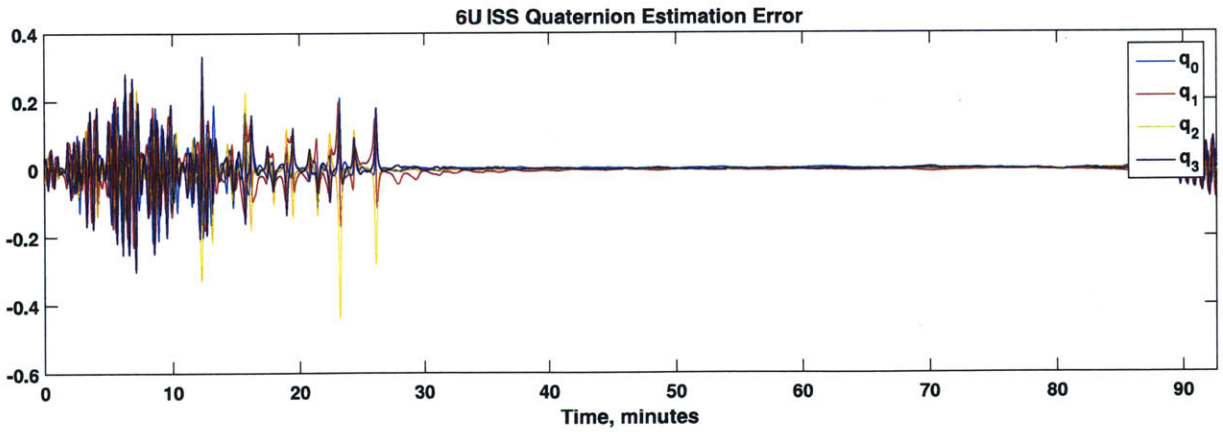

Figure 4-17: Plot of the 6U ISS orbit spacecraft UKF quaternion element estimation error. *Image credit: W. Marlow.*

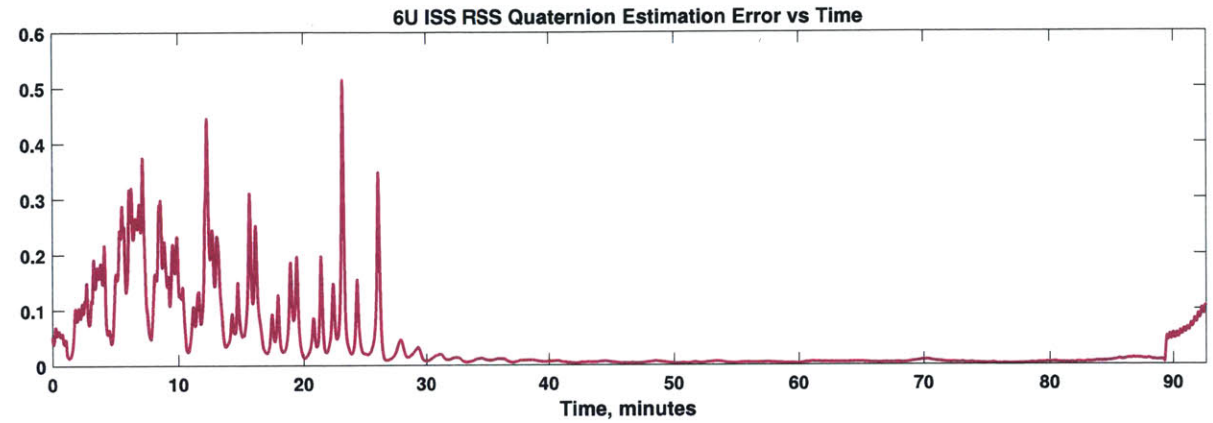

Figure 4-18: Plot of the 6U ISS orbit spacecraft UKF RSS quaternion estimation error. *Image credit: W. Marlow.*

When the RSS quaternion error for both filters is presented for direct comparison in Figure 4-19, the impact of the error growth early in the orbit can be seen when compared to the EKF. Further tuning of the filter may help reduce the time for the filter to converge and reduce the over all error, which can be seen happening by about 25 minutes into the orbit.

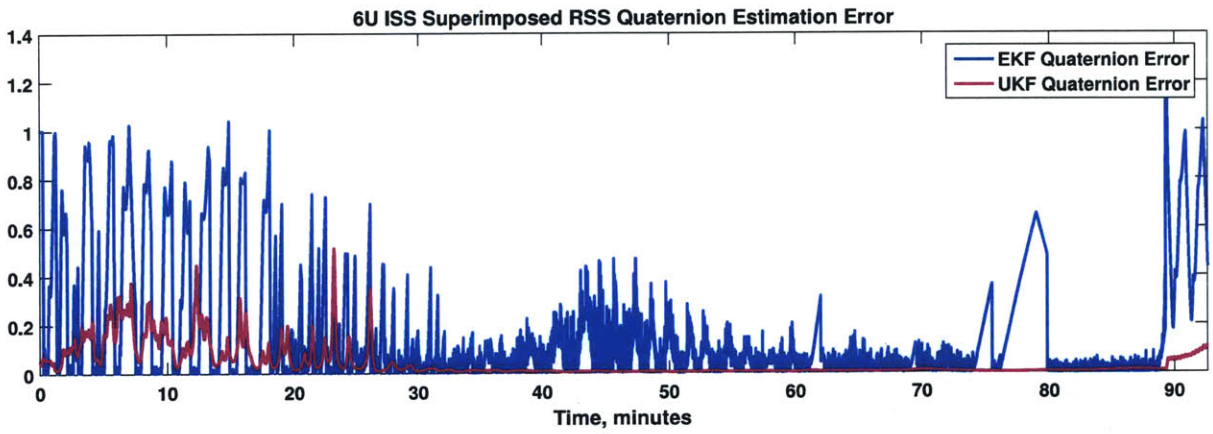

Figure 4-19: Combined plots of the ISS orbit 6U EKF and UKF RSS quaternion estimation errors. *Image credit: W. Marlow*

The impact of the poor initial performance can be seen in the Euler angle errors quite clearly in Figure 4-20.

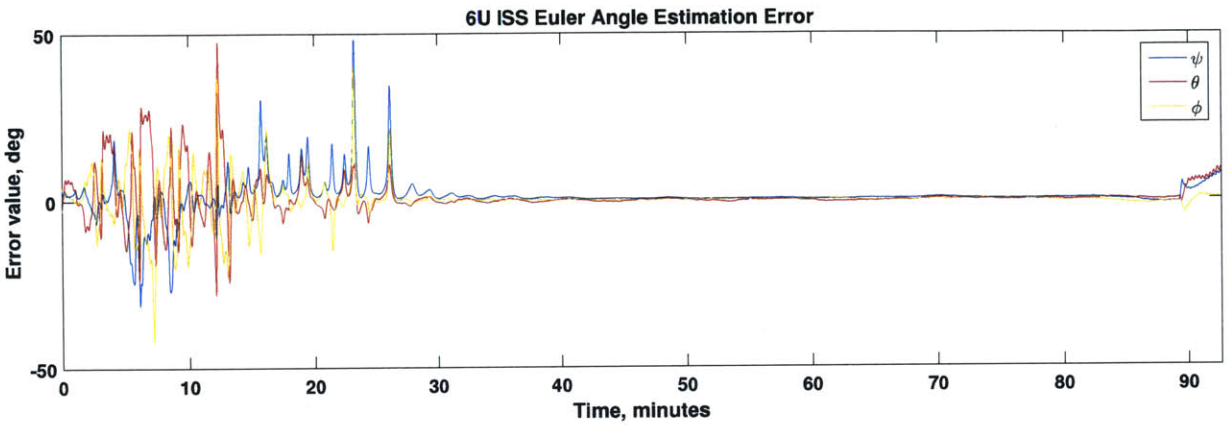

Figure 4-20: Combined plot of 6U ISS orbit UKF individual Euler angle errors. *Image credit: W. Marlow.*

As before, a summary of the filter performances over ISS orbit for the 6U satellite are presented in Table 4.7. Table 4.8 displays the error statistics for the first 55 minutes of the orbit. See Figure 4-16 for the spacecraft rates for this orbit.

Overall performance comparison and summary		
Filter	μ_{total}	σ_{total}
EKF	1.05°	1.31°
UKF	-0.18°	0.41°

Table 4.7: 6U ISS performance summary.

t<55 minutes performance comparison and summary		
Filter	μ_{total}	σ_{total}
EKF	-19.92°	35.55°
UKF	-0.34°	0.83°

Table 4.8: 6U ISS performance summary for high rate tumbling.

The UKF performance for this mission was able to improve upon the already fair performance of the EKF for the full orbit. The UKF improved the mean error by nearly 83% and the variance by nearly 69% compared the EKF. The length of time with higher rotation rates was a larger portion of this orbit. For this segment of the

orbit, the mean error was reduced by nearly two orders of magnitude, by 98%. The variance was similarly improved.

4.4.2 Sun-synchronous Orbit

Presented next are results for the estimation of the 6U sun-synchronous orbit mission. The spacecraft rates are given in Figure 4-21 for reference. The filter parameters for this mission were tuned to gain some improvement. The variable α was adjusted to 1×10^{-1} to change the spread of the sigma points and reduce the overall estimation error. All other parameters remained the same.

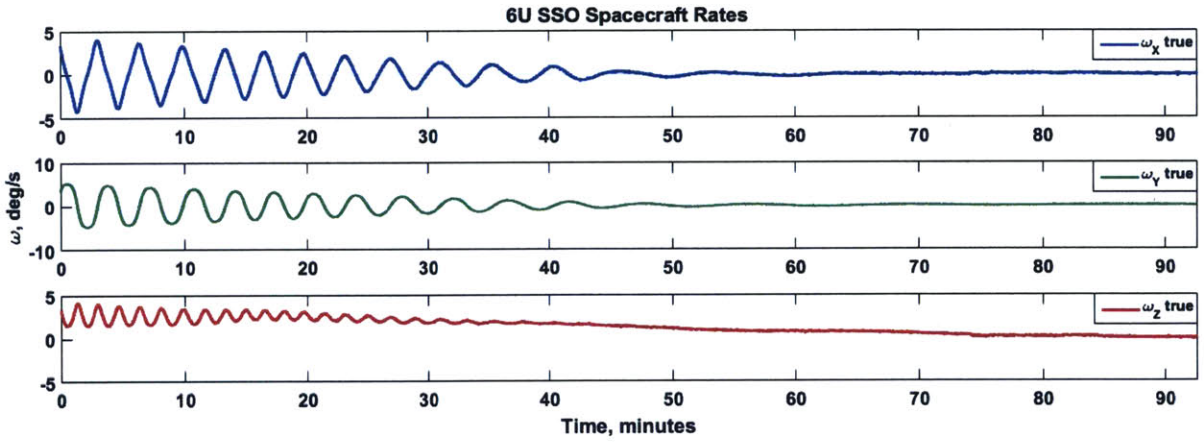

Figure 4-21: 6U SSO spacecraft body rates. *Image credit: W. Marlow.*

For more than half of the orbit in this scenario, the spacecraft rates are high enough to cause a fair amount of error in the EKF implementation. The length of time for the detumble can be attributed in the orbit orientation relative to the local magnetic field lines. Since the detumble algorithm uses the magnetorquers to slow the spacecraft rates, the alignment of the field lines with the orbit reduce the available control authority and lengthen the time for detumble.

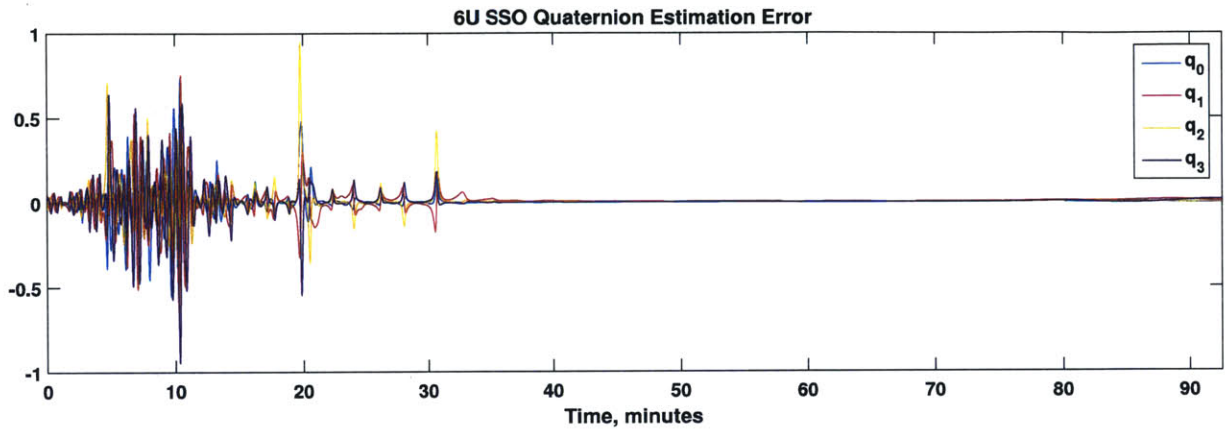

Figure 4-22: Plot of the 6U SSO spacecraft UKF quaternion element estimation error. *Image credit: W. Marlow.*

In Figures 4-22 and 4-23, the UKF quaternion error initially wavers and grows until the filter can converge and lower the estimation error for the remainder of the orbit.

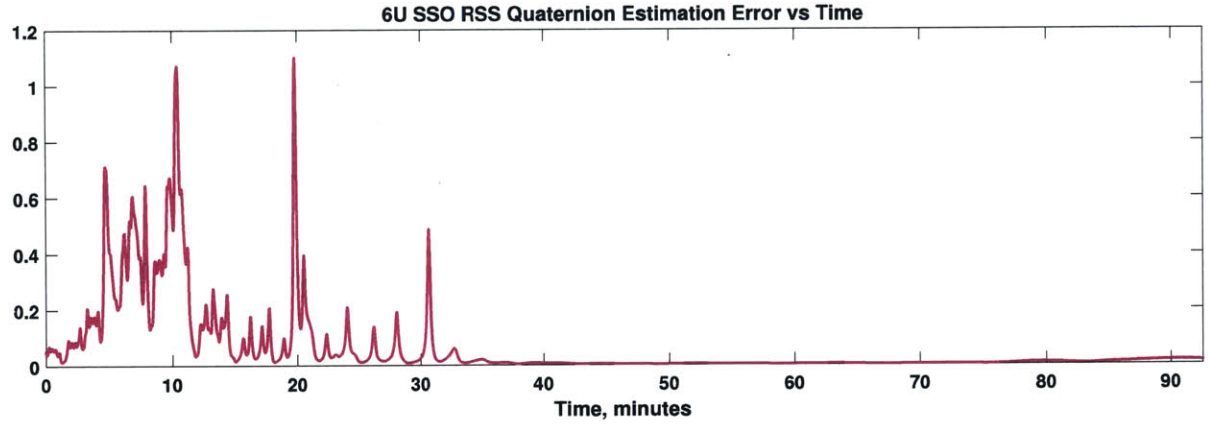

Figure 4-23: Plot of the 6U SSO spacecraft UKF RSS quaternion estimation error. *Image credit: W. Marlow.*

Figure 4-24 has the direct comparison for the UKF and EKF quaternion estimation error. There are brief spikes where the UKF error is temporarily higher than the EKF, but the performance for the entirety of the orbit is greatly improved over the EKF.

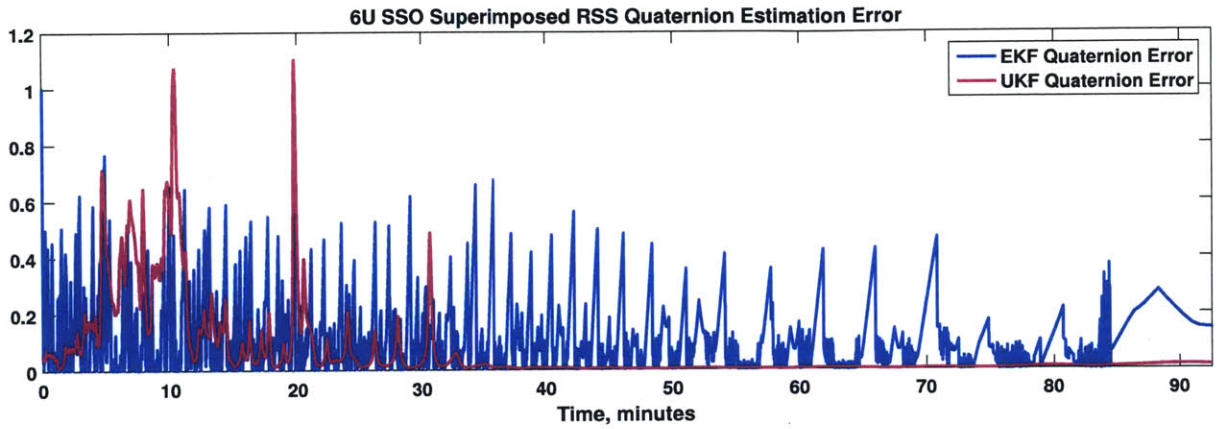

Figure 4-24: Combined plots of the 6U SSO spacecraft EKF and UKF RSS quaternion estimation errors. *Image credit: W. Marlow*

The initial estimation error can be seen in the Euler angles before about 30 minutes. After this time, the errors are kept consistently low.

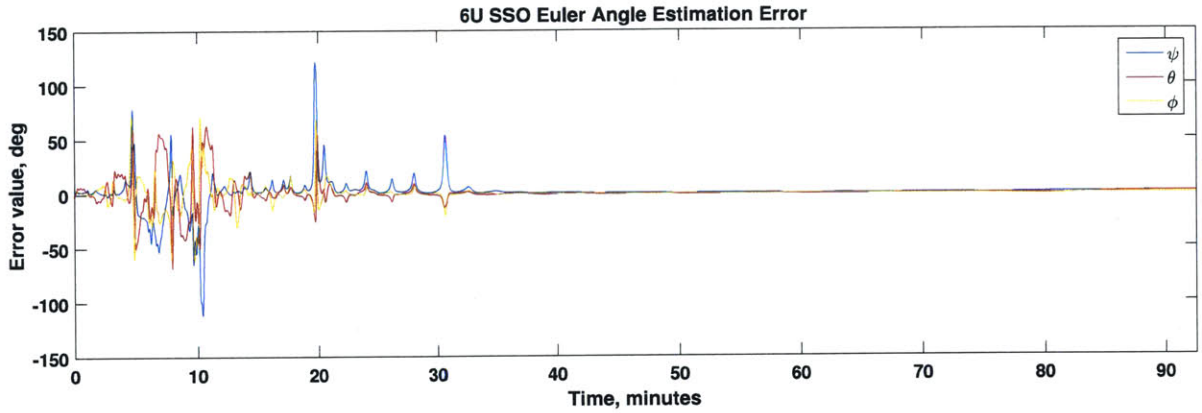

Figure 4-25: Combined plot of 6U SSO spacecraft UKF individual Euler angle errors. *Image credit: W. Marlow.*

The performance summary tables for this orbit are provided in Table 4.9 and Table 4.10.

Overall performance comparison and summary		
Filter	μ_{total}	σ_{total}
EKF	-2.95°	32.14°
UKF	-0.20°	1.57°

Table 4.9: 6U SSO performance summary.

t<50 minutes performance comparison and summary		
Filter	μ_{total}	σ_{total}
EKF	-39.80°	42.11°
UKF	-1.81°	6.54°

Table 4.10: 6U SSO performance summary for high rate tumbling.

Overall, the UKF improved the mean error by 93% and the variance by similarly by about 95%. The early orbit operations improved the attitude estimation by about the same amount. The mean error was reduced by 95% and the variance was reduced by about 84%.

4.4.3 800 km Orbit

The final set of results are those for the 6U 800 km altitude orbit configuration. The spacecraft rates are given in Figure 4-26 for reference. The same filter parameter as before was tuned for this implementation. The variable α was adjusted to 1×10^{-1} to change the spread of the sigma points and similarly reduce the overall estimation error.

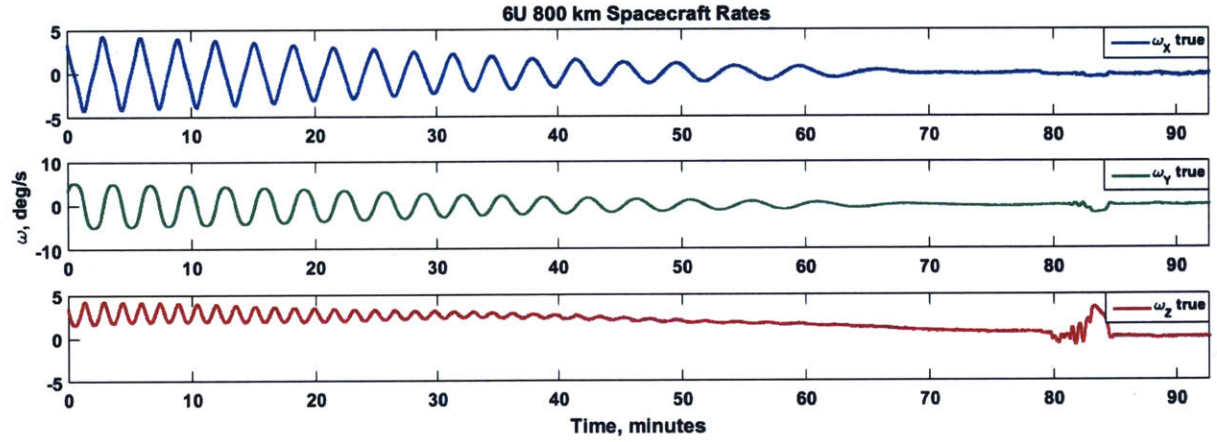

Figure 4-26: 6U 800 km spacecraft body rates. *Image credit: W. Marlow.*

With the extended period of spacecraft tumbling, the UKF performs better than the EKF for the majority of the orbit in this case. The more massive spacecraft and higher orbit altitude lengthen the detumble period significantly. The quaternion

elements have a similar appearance to the 6U SSO mission, with errors early in the orbit until the filter converges. These can be seen in Figures 4-27 and 4-28.

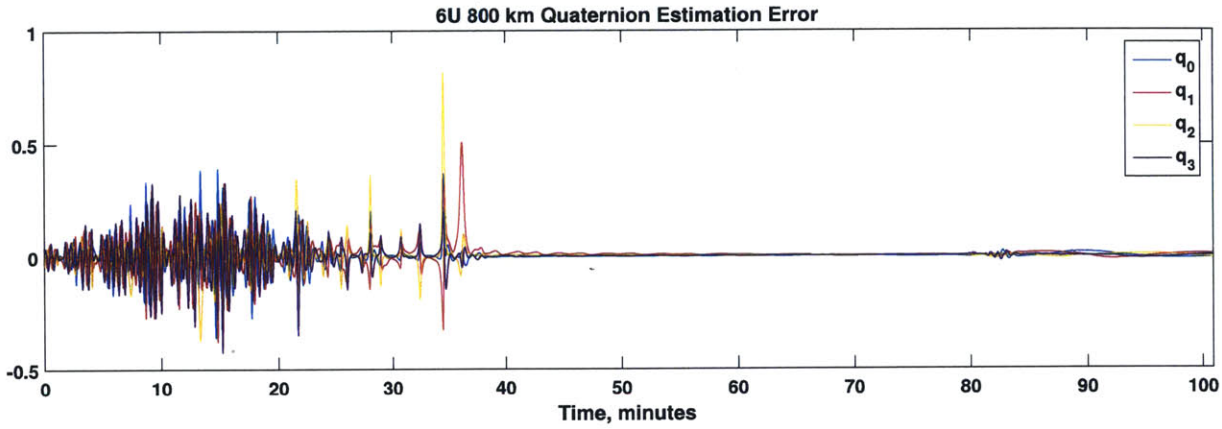

Figure 4-27: Plot of the 6U 800 km orbit spacecraft UKF quaternion element estimation error. *Image credit: W. Marlow.*

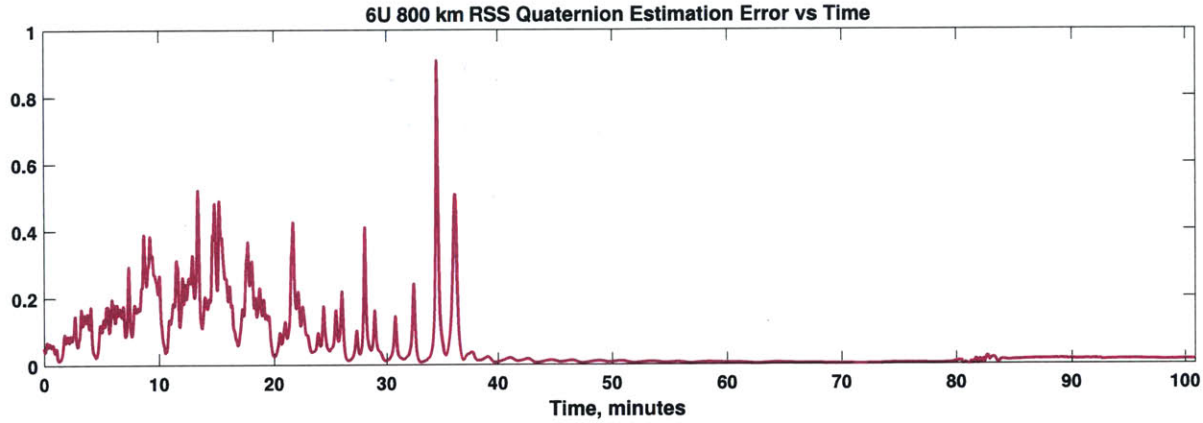

Figure 4-28: Plot of the 6U 800 km orbit spacecraft UKF RSS quaternion estimation error. *Image credit: W. Marlow.*

The EKF and UKF RSS errors are presented in Figure 4-29. Here, the UKF can be seen with similar RSS errors compared the EKF early in the orbit.

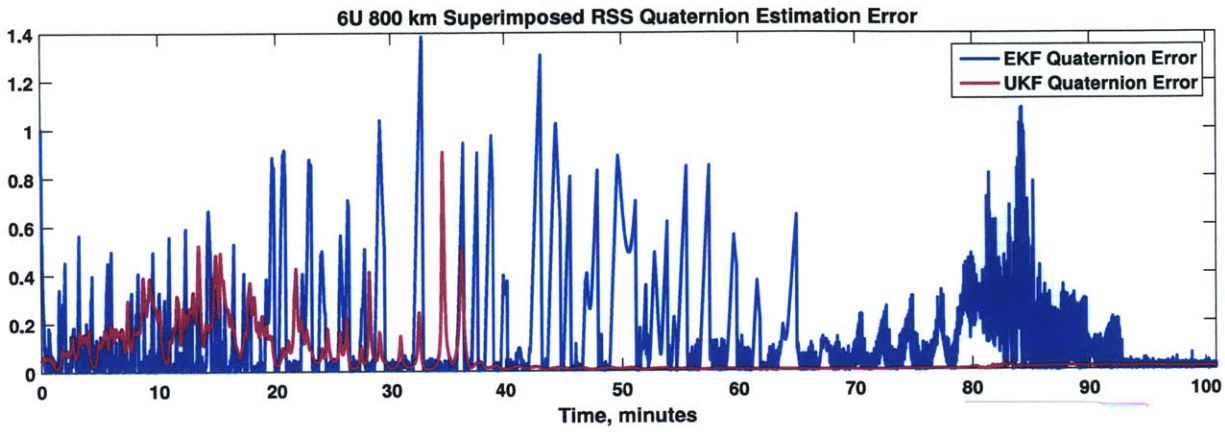

Figure 4-29: Combined plots of the 6U 800 km orbit spacecraft EKF and UKF RSS quaternion estimation errors. *Image credit: W. Marlow*

Despite the overall good performance, the variance in the attitude error was still quite high early in the orbit. Figure 4-30 shows the various peaks in Euler angle estimation error before filter convergence.

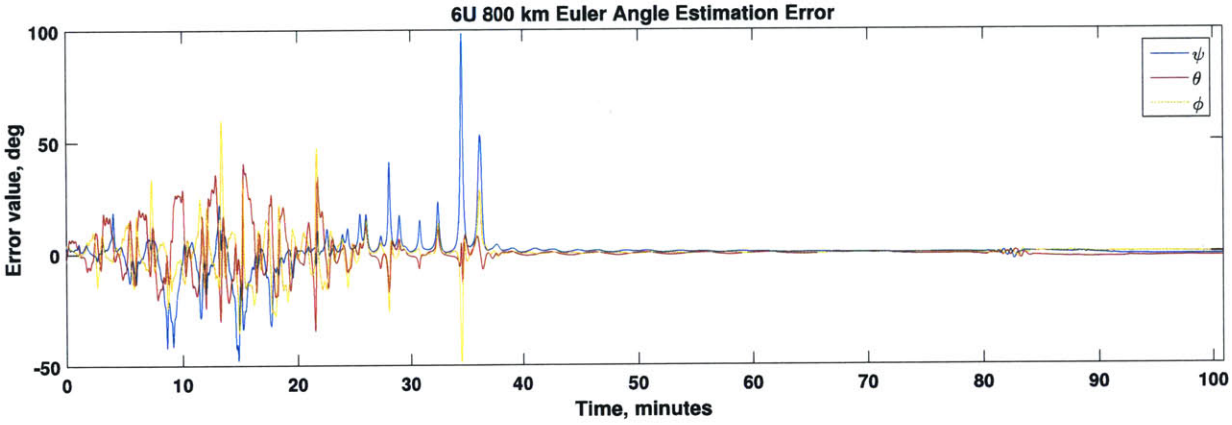

Figure 4-30: Combined plot of 6U 800 km orbit spacecraft UKF individual Euler angle errors. *Image credit: W. Marlow.*

Finally, Tables 4.11 and 4.12 show the overall and early orbit performance, respectively.

Overall performance comparison and summary		
Filter	μ_{total}	σ_{total}
EKF	-4.03°	6.31°
UKF	0.01°	0.47°

Table 4.11: 6U 800 km performance summary for high rate tumbling.

t<60 minutes performance comparison and summary		
Filter	μ_{total}	σ_{total}
EKF	-28.69°	49.86°
UKF	0.66°	0.42°

Table 4.12: 6U 800 km performance summary for high rate tumbling.

The UKF performed well on this mission profile, despite the early spikes in attitude error. The mean error for the full orbit was reduced by over two orders of magnitude to within the desired levels of pointing accuracy for a lasercomm mission with body-pointing only. This shows a significant improvement over the previous filter iteration. The variance for the full orbit was reduced by about 93%. For the majority of the orbit, the spacecraft rates were high enough to disturb the EKF performance. The mean error during this time was reduced by almost 98% and the variance by over two orders of magnitude when compared to the EKF performance.

4.4.4 Varying Filter Parameters

The filter parameters k and α, discussed in Chapter 3, were varied and the results are shown in the following plots. The term β was not altered. The distributions that the sigma points were sampled from are assumed Gaussian, so this term remained $\beta = 2$ for the following results.

The term for the sigma point spread, α, was kept at small values to retain a tight spreading of the sigma point population. This helped overall filter performance by increasing the filter resolution. α was taken below the typical lower bound of

1×10^{-4} to investigate the impact it had on performance. The filter performance decreased significantly beyond this limit (not shown). In the results shown, the filter had a sufficient grouping of sigma points for sampling, and the k term allowed for an additional 'tuning' parameter.

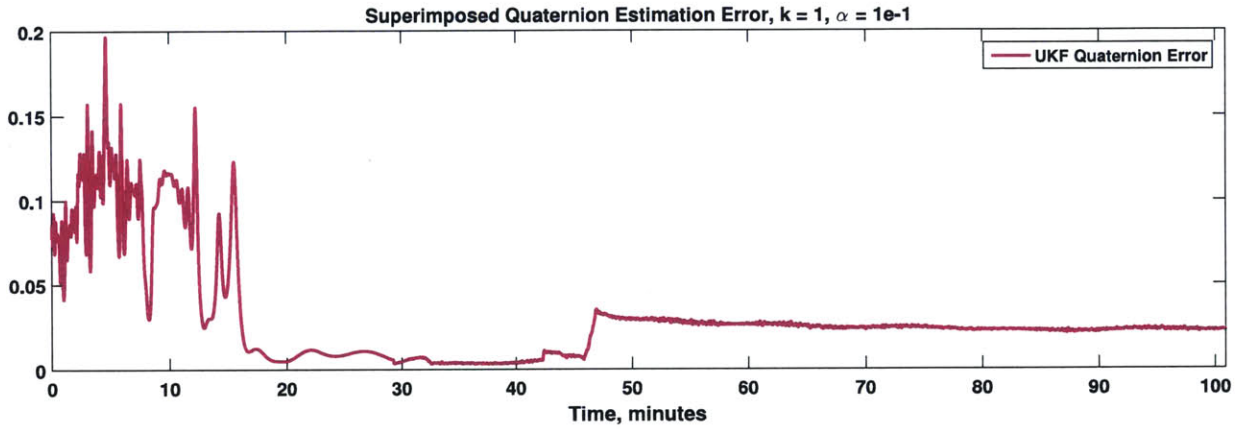

Figure 4-31: Plot of UKF performance. UKF parameters: $k = 1$, $\beta = 1$, and $\alpha = 1 \times 10^{-1}$. *Image credit: W. Marlow*

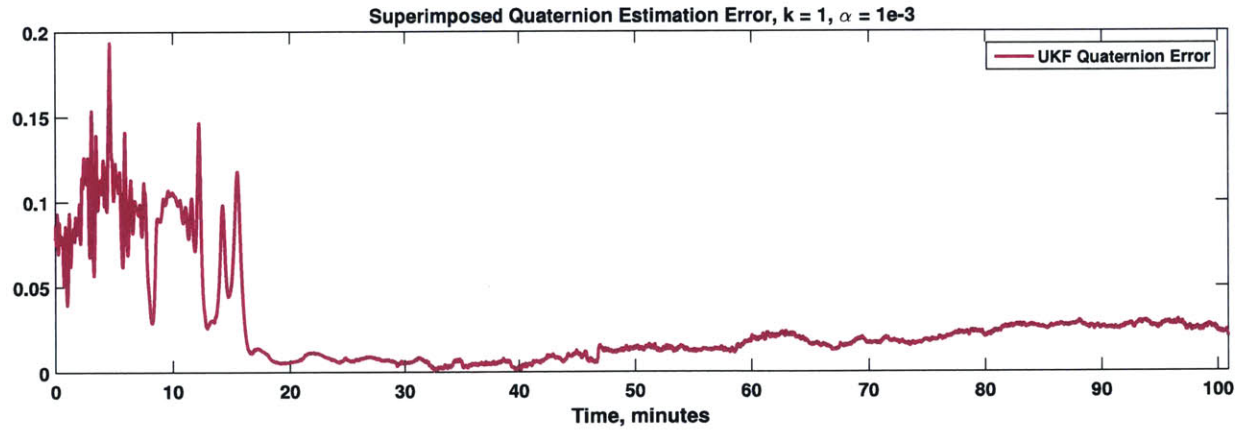

Figure 4-32: Plot of UKF performance. UKF parameters: $k = 1$, $\beta = 1$, and $\alpha = 1 \times 10^{-3}$. *Image credit: W. Marlow*

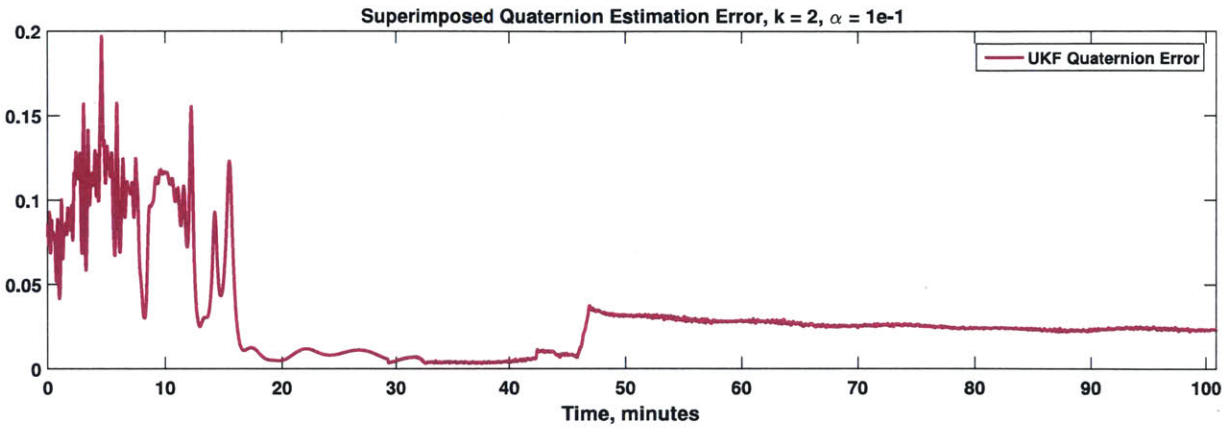

Figure 4-33: Plot of UKF performance. UKF parameters: $k = 2$, $\beta = 2$, and $\alpha = 1 \times 10^{-1}$. *Image credit: W. Marlow*

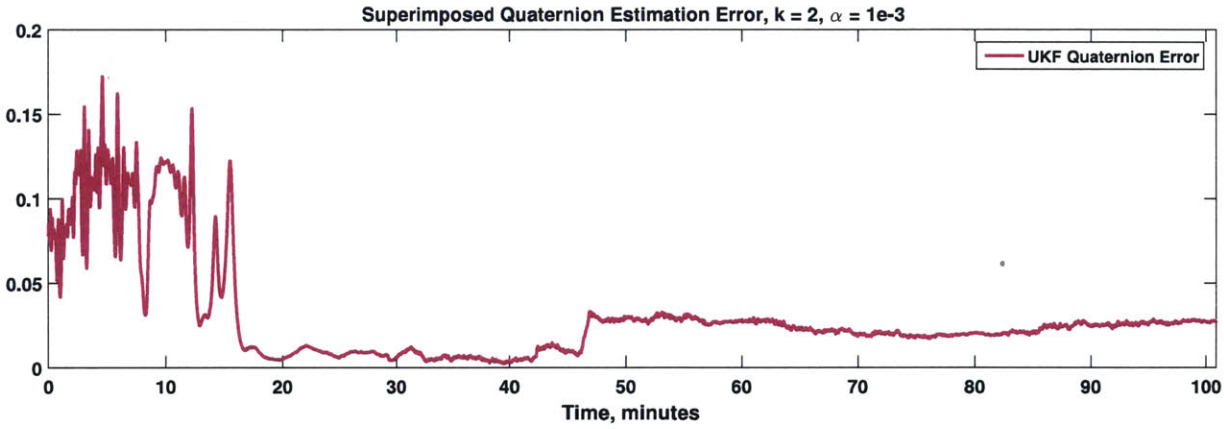

Figure 4-34: Plot of UKF performance. UKF parameters: $k = 2$, $\beta = 2$, and $\alpha = 1 \times 10^{-3}$. *Image credit: W. Marlow*

Additional variations were investigated for this work, but a sampling of the combinations are shown. Varying the parameter α to the higher end of the bounds reduced the filter sigma point resolution, and the UKF performance decreased overall.

4.5 Areas for Algorithm Improvement

With additional tuning and modifications, the Unscented Kalman filter presented in this work has the capacity to alleviate high-rate estimation problems seen with the Extended Kalman filter used in many CubeSat platforms. Due to the desire to

implement a filter with Euler angle representation, the implementation of a traditionally quaternion-only filter was foregone for this work. To avoid the computation of trigonometric functions on less capable microprocessors, the quaternion-only filter design will be implemented in future work. Additionally, a more robust Monte Carlo-like or optimization approach into filter parameter adjustment would help fine-tune the algorithms after the quaternion-only filter design is complete.

4.6 Summary

The UKF has overall advantages for attitude estimation in direct comparison with the EKF implemented on previous CubeSat programs. With the higher rotation rates in the detumble phases seen on all of the simulations, the UKF significantly outperformed the EKF in early-orbit operations. The Unscented filter applied to the simulations in this work was able to achieve better than the desired pointing accuracy for lasercomm on CubeSats, showing the utility of addressing attitude estimation with more advanced methods of filtering. High accuracy attitude estimation is a different but equally important capability than attitude stability, which is a separate topic of interest for the implementation of the UKF within a feedback control system. This version of the UKF has yet to be optimized to gain further error improvements, but the authors expect even better performance with such work.

In the scenarios presented for these simple detumble cases, fine attitude estimation is not necessary. Appropriate algorithms for detumbling use only coarse attitude sensing to aid in slowing the spacecraft. However, it is easy to extrapolate the usefulness of greater estimation accuracy using the proposed Unscented Kalman filter during high spacecraft body rates to the concepts of operations described in chapter 2, Section 2.2.4.

Chapter 5

Conclusion and Future Work

5.1 Summary

Typical communication or Earth-sensing satellites are large systems that are high cost and the development and operation of such systems are highly risk averse. The emergence of CubeSats has allowed the science and engineering fields to explore a new paradigm in satellite development for proof of concept operation. As these nanosatellites gain popularity and capability, they are moving beyond proof of concept missions and providing real scientific value. This work focused on 3U and 6U satellite missions in low Earth orbit. These miniaturized satellites are accommodated as auxiliary payloads on standard launches with ride-sharing. As CubeSats are being used for increasingly demanding mission profiles, an increase in attitude estimation and control performance is highly desired, if not required.

The overall aim of this work is to improve the current state of the art in CubeSat attitude estimation using Unscented Kalman filtering. We discussed the difficulty in achieving high-accuracy attitude estimation inherent in nanosatellite platforms. These include, but are not limited to, low-cost attitude sensors that are noisy and may not be well-characterized, limited volume for high-accuracy sensors, and limited computational power. There has been only a minimal amount of research to-date in developing and applying advanced filtering methods to these small platforms. This work focuses on adding to this body of research and help advance the state of the art

in attitude knowledge by at least two orders of magnitude from about 1-5° attitude knowledge error down to 0.05° or better.

5.2 Research Contributions

Our proposed tool for increasing attitude estimation performance (and ultimately attitude control improvement) was the Unscented Kalman filter. Along with a formulation for the state dynamics using both quaternion and Euler angle representation, this work applied an efficient UKF to the satellite state equations. This method has advantages over traditionally fielded CubeSat attitude filters in higher rotation rate regimes. Here, nonlinearities in the state dynamics play a dominant role in introducing errors into the estimation schemes. For the six missions simulated, the detumble phase early in the orbit was the region where the UKF reliably outperformed the previously-developed extended Kalman filter.

The simulated measurements for this work were the gyroscopes and magnetometers. With the limited measurement profiles, this work was still able to produce improvements in attitude estimation. Ultimately, this can translate into better control and finer body pointing for the CubeSat platforms described, and can help enable the advanced concepts of operations described earlier, in Chapter 2, Section 2.2.4.

The UKF that was developed has higher attitude estimation accuracy over the EKF for nearly all operations for the six missions presented. This is highlighted during high angular rate mission operation. Figure 5-1 contains all of the mean attitude estimation results for the full orbits of the different missions. In one instance the filter was able achieve the desired two order of magnitude improvement in attitude estimation for the full orbit profile, and two others attaining this level for the higher rate portions of the orbit (see Chapter 4, Sections 4.3 and 4.4 for performance summary tables). One implementation was able to achieve better than the desired 0.05° attitude estimation error threshold for the entire orbit profile, with another simulation achieving 0.06° during the high-rate early orbit operations, showing that future improvements of this work should increase capability into this operational regime.

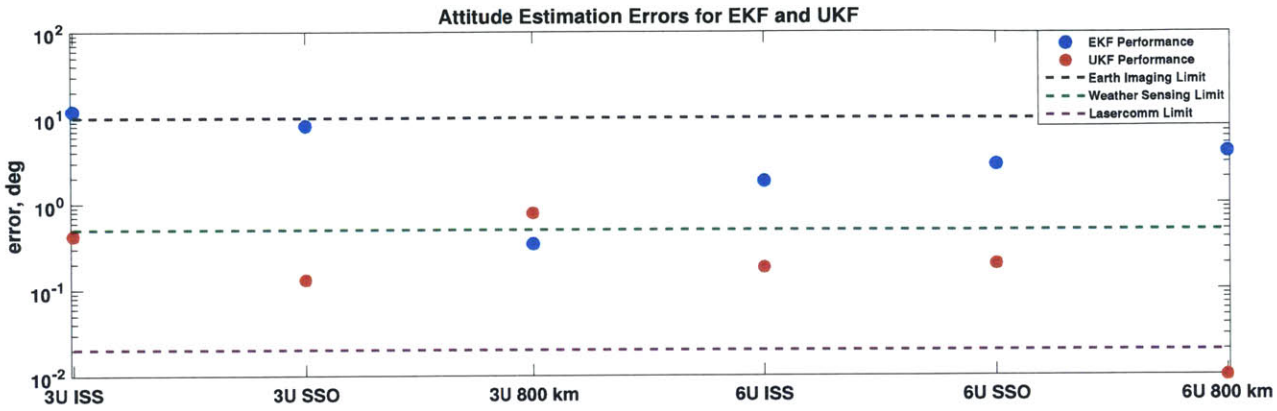

Figure 5-1: Benchmarks for the EKF and UKF-based attitude estimation for the different labeled mission profiles. Attitude knowledge limits for different operational needs are marked by the dashed lines. *Image credit: W. Marlow.*

Continued improvement of the filter should achieve the desired increase in attitude estimation capability and decrease computational loading. Despite the increase in performance for certain parts of the missions, this is not sufficient for what will be required for body-pointing laser communication on CubeSats. The inclusion of a fast steering mirror to enable ultra-fine beam control can help alleviate these pointing requirements. Even with the inclusion of an FSM for lasercomm, the spacecraft will still need to have attitude knowledge and control of single degrees or better[28]. The plot in Figure 5-1 also includes the minimum pointing capability needed for the different missions described in Chapter 1.

5.2.1 Approach Improvements and Additions

In future implementations of the UKF and variations proposed, measurement noise from all attitude sensing sources will also be considered. As described in Chapter 1, these will include:

- 3-axis gyroscope: The 3-axis gyro was included in this revision, and will be kept for future work.

- 3-axis accelerometer: The 3-axis accelerometer was included in this revision, and will be kept for future work. It will be especially useful for the inclusion of

thrusters.

- 3-axis magnetometer: The 3-axis magnetometer was included in this revision, and will be kept for future work.

- Coarse sun sensors: The coarse sun sensors will allow for a sun vector solution during non-eclipse. This additional attitude reference vector will help clarify ambiguities during calculations.

- Earth horizon sensors: These sensors will allow for a relatively fine calculation of the nadir vector. Ongoing work in the SSL aims to better characterize these sensors to improve the models.

- Star trackers: The inclusion of star trackers will likely greatly improve overall attitude estimation. For future iterations of this work, star trackers will replace Earth horizon sensors as the main provider of fine attitude sensing.

5.3 Future Work

5.3.1 Further UKF Derivations

The future work for the Unscented Kalman filter development for CubeSats includes the addition of two more UKF variations. These additions will address two main concerns with attitude estimation on nanosatellites.

Minimal Set UKF

The fist UKF variation will help improve the performance of the filter on the computationally-limited systems. This is done by reformulating the filter[38] to utilize only a minimal set of sigma points of $n+1$ rather than the traditional $2n+1$. With this formulation, the weighting parameters are chosen similarly as the standard UKF,

$$W_0^{(m)} = \lambda/(n+\lambda) \tag{5.1}$$

$$W_0^{(c)} = \lambda/(n+\lambda) + \left(1 - \alpha^2 + \beta\right) \tag{5.2}$$

and

$$W_i^{(m)} = W_i^{(c)} = 1/(2(n+\lambda)) \quad \text{for} \quad i = 1, ..., n \tag{5.3}$$

and the new covariance parameters are derived with the minimal set,

$$\mathbf{Q}_{yy(k|k-1)} = \sum_{i=0}^{n} W_i^{(c)} \left\{\mathcal{Y}_{i(k|k-1)} - \mathbf{y}_{(k|k-1)}\right\} \left\{\mathcal{Y}_{i(k|k-1)} - \mathbf{y}_{(k|k-1)}\right\}^T + \mathbf{R}_k \tag{5.4}$$

and

$$\mathbf{Q}_{xy(k|k-1)} = \sum_{i=0}^{2n} W_i^{(c)} \left\{\mathcal{X}_{i(k|k-1)} - \mathbf{x}_{(k|k-1)}\right\} \left\{\mathcal{Y}_{i(k|k-1)} - \mathbf{y}_{(k|k-1)}\right\}^T \tag{5.5}$$

Adaptive UKF

Additional work will be taken on to include the ability for the minimal filter to adapt to the noise parameters of the system. The adaptive UKF[32] allows for the sampling of the innovation sequence over time,

$$\hat{\mathbf{W}}_v = \frac{1}{N} \sum_{i=k-N+1}^{k} \Delta\hat{\mathbf{x}}_k \Delta\hat{\mathbf{x}}_k^T \tag{5.6}$$

where N is a sampling parameter chosen. This new weighting parameter can be used to update the covariance parameters for the measurement sequence,

$$\hat{\mathbf{R}}_k = \hat{\mathbf{W}}_v + \mathbf{Q}_{k|k-1} - \mathbf{K}_{k+1}\mathbf{Q}_{yy}\mathbf{K}_{k+1}^T \tag{5.7}$$

$$\hat{\mathbf{Q}}_k = \mathbf{K}_{k+1}\hat{\mathbf{W}}_v\mathbf{K}_{k+1}^T \tag{5.8}$$

The proposed work flow is shown in Figure 5-2. The unscented transformation is based on existing works, and is being improved upon for future work. The continued EKF implementations will work to include the minimal and adaptive qualities to the filter.

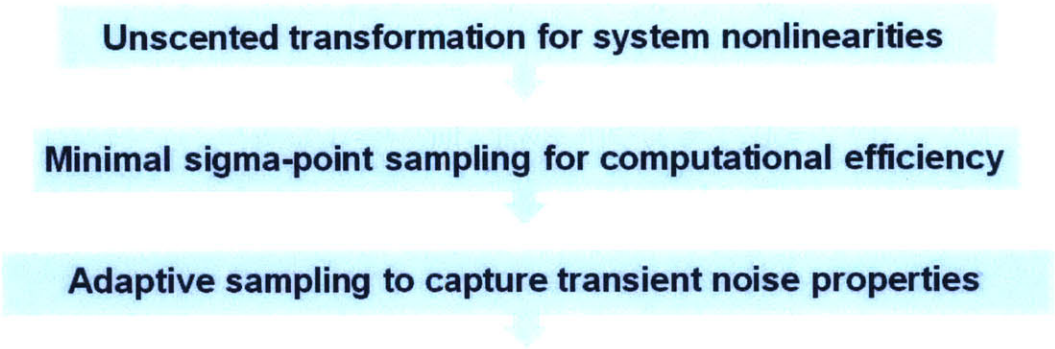

Figure 5-2: Notional CubeSat minimal adaptive unscented Kalman filter development work flow. *Image credit: W. Marlow.*

The extension of the advanced filters to the larger spacecraft bus will need to include propulsion models, which necessitate future discussion with the MIT space propulsion laboratory researchers, and commercial developers and suppliers of CubeSat propulsion systems. This work will extend the current body of work in minimal and adaptive UKF work on CubeSats by offering new formulations of the filters and applying them to full mission profiles with heritage sensor and actuator models, along with extensive testing and tuning with HIL.

Hardware In the Loop and Test Infrastructure

In future work, we intend to develop a more robust, project-agnostic CubeSat testing infrastructure for the MIT SSL. Given that many CubeSat projects are now in development in the laboratory, it would benefit the projects to have a dedicated hardware-in-the loop test facility that uses flight-like processing for Cubesats. The use of empirical data and simulated data for all attitude sensors will help exercise closed-loop control and estimation in this HIL setup. Additionally, there are plans to further develop a single-axis air bearing test platform inside the SSL Helmholtz cage for characterization of magnetometers, magnetorquers, and reaction wheel performance. Figure 5-3 shows the existing Helmholtz cage, developed by previous graduate students[49].

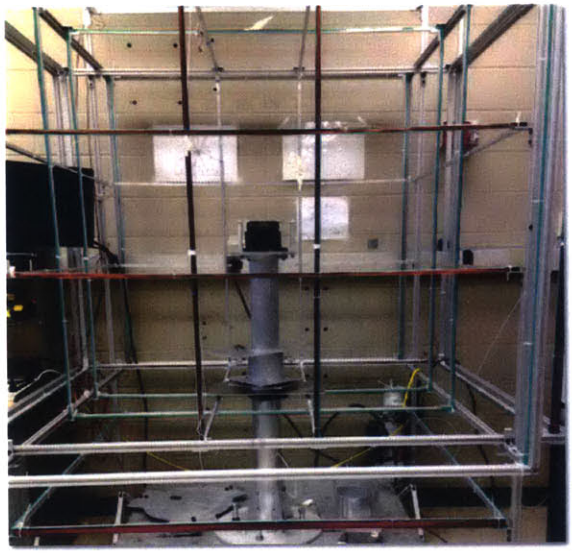

Figure 5-3: MIT Space Systems Laboratory 3-axis Helmholtz cage for simulating the Earth's orbital magnetic field. *Image credit: W. Marlow.*

Computational Benchmarking

Future work aims to benchmark the execution of the UKF code in the hardware-in-the-loop setup using flight-like ADCS processors and avionics motherboard processors or microcontrollers. Current UKF implementations are only benchmarked against EKF using a laptop computer in a MATLAB environment[1]. This is not representative of the true performance and processor loading that would be expected for the CubeSat platforms.

[1]Laptop specifications: Dell Latitude E6540, Intel Core i7-4610M 3.00 GHz CPU, 16.0 GB RAM, Windows 7 64-bit

Bibliography

[1] *A new approach to linear filtering and prediction problems*, author=Kalman, Rudolph Emil. *Journal of basic Engineering*, 82(1):35–45, 1960.

[2] *Flight results of a low-cost attitude determination system*, author=Springmann, John C and Cutler, James W. *Acta Astronautica*, 99:201–214, 2014.

[3] Analog Devices, Inc., *ADIS16334 Six Degree of Freedom Inertial Sensor Datasheet.*

[4] European Space Agency. *Earth Observation Portal: AeroCube-OCSD.* `https://directory.eoportal.org/web/eoportal/satellite-missions/a/aerocube-ocsd`, April 2016.

[5] European Space Agency. *Earth Observation Portal: eoPortal Directory AAUSat-2 (Aalborg University CubeSat-2).* `https://directory.eoportal.org/web/eoportal/satellite-missions/a/aausat-2`, May 2016.

[6] European Space Agency. *Earth Observation Portal: eoPortal Directory CanX-2.* `https://directory.eoportal.org/web/eoportal/satellite-missions/c-missions/canx-2`, March 2016.

[7] European Space Agency. *Earth Observation Portal: eoPortal Directory CUTE-I (Cubical Tokyo Tech Engineering Satellite-I).* `https://directory.eoportal.org/web/eoportal/satellite-missions/c-missions/cute-i`, May 2016.

[8] European Space Agency. *Earth Observation Portal: eoPortal Directory UWE-1 (UniversitÃ∂t WÃijrzburg's Experimentalsatellit-1).* `https://directory.eoportal.org/web/eoportal/satellite-missions/u/uwe-1`, May 2016.

[9] European Space Agency. *Earth Observation Portal: MiniCOR.* `https://directory.eoportal.org/web/eoportal/satellite-missions/m/minicor`, April 2016.

[10] Justin Albert. *Satellite-mounted Light Sources as Photometric Calibration Standards for Ground-based Telescopes. The Astronomical Journal*, 143(1):8, 2011.

[11] Lt. Kelly Alexander. *AFRL University Nanosat Program (UNP).* In *CubeSat Developers' Workshop*, 2012.

[12] Blue Canyon Technologies, *BCT XACT Datasheet.*

[13] Christopher R Binz, Mark A Davis, Bernie E Kelm, and Christopher I Moore. *Optical Survey of the Tumble Rates of Retired GEO Satellites.* Technical report, DTIC Document, 2014.

[14] William J. Blackwell, Rebecca Bishop, Kerri Cahoy, Brian Cohen, Clayton Crail, Lidia Cucurull, Pratik Dave, Michael DiLiberto, Neal Erickson, Chad Fish, Shu-peng Ho, R. Vincent Leslie, Adam B. Milstein, and Idahosa A. Osaretin. *Radiometer Calibration Using Colocated GPS Radio Occultation Measurements. IEEE Transactions on Geoscience and Remote Sensing*, 52(10), 2014.

[15] William J. Blackwell, Christy F. Cull, Richard N. Czerwinski, R. Vincent Leslie, and Idahosa Osaretin. *The Advanced Technology Microwave Sounder (ATMS): New Capabilities for Atmospheric Sensing.* Presentation at the 92nd American Meteorological Society Annual Meeting, New Orleans, LA, 2012.

[16] California Polytechnic State University. *CubeSat Design Specification* Rev 13.

[17] J.L. Crassidis and J.L. Junkins. *Optimal Estimation of Dynamic Systems.* Chapman & Hall/CRC Applied Mathematics & Nonlinear Science. CRC Press, 2004.

[18] Peter Fortescue, Graham Swinerd, and John Stark. *Spacecraft Systems Engineering.* Wiley, United Kingdom.

[19] Vlad Grigore. *Unscented Kalman Filters for Attitude and Orbit Estimation of a Low Earth Orbit CubeSat.* 2015.

[20] Hamid Hemmati. *Near-Earth Laser Communications.* CRC Press, 2009.

[21] Wikipedia Foundation Inc. *Geomagnetic Pole*, 2016.

[22] Wikipedia Foundation, Inc. *SACRED.* `https://en.wikipedia.org/wiki/SACRED`, May 2016.

[23] Siegfried W. Janson and Richard P. Welle. *The NASA Optical Communication and Sensor Demonstration Program.* In *Proceedings of the 27th AIAA/USU Conference on Small Satellites*, Small Satellite Constellations, Logan, Utah, USA, August 2013. AIAA/USU.

[24] Bryan Johnston-Lemke. *Arc-Minute Attitude Stability on a Nanosatellite: Enabling Stellar Photometry on the Smallest Scale.* 2011.

[25] Simon J. Julier and Jeffrey K. Uhlmann. *New extension of the Kalman filter to nonlinear systems*, 1997.

[26] John Leif JÃÿrgensen, Troelz Denver, Maurizio Betto, Peter SiegbjÃÿrn JÃÿrgensen, Hans-Peter RÃűser, Rainer Sandau, and Arnoldo Valenzuela. *The Micro ASC, a Miniature Star Tracker*, pages 157–162. 2003.

[27] Zee R.E. Pranajaya F.M. Kekez, D.D. *Launches and On-Orbit Performance - An Update on Nanosatellite Missions at the UTIAS Space Flight Laboratory.* Presentation at the CalPoly CubeSat Summer Workshop, San Luis Obispo, CA, 2011.

[28] Ryan W. Kingsbury. *Optical Communications for Small Satellites.* PhD thesis, Massachusetts Institute of Technology, Department of Aeronautics and Astronautics, September 2015.

[29] Ryan W. Kingsbury, Kathleen Riesing, Tam N. Nguyen, and Kerri Cahoy. *Two-Stage Control for CubeSat Optical Communications.* Presentation at the CalPoly CubeSat Developers' Workshop, San Luis Obispo, CA, 2014.

[30] NASA Jet Propulsion Laboratory. *Arcsecond Space Telescope Enabling Research in Astrophysics (ASTERIA)*, 2016.

[31] Junquan Li, Mark A Post, and Razak Lee. *A novel adaptive unscented Kalman filter attitude estimation and control systems for 3U nanosatellite.* In *Control Conference (ECC), 2013 European*, pages 2128–2133. IEEE, 2013.

[32] Junquan Li, Mark A Post, and Razak Lee. *A novel adaptive unscented Kalman filter attitude estimation and control systems for 3U nanosatellite.* In *Control Conference (ECC), 2013 European*, pages 2128–2133. IEEE, 2013.

[33] Defense Industry Daily LLC. *Small Is Beautiful: US Military Explores Use of Microsatellites.* `http://www.defenseindustrydaily.com/Small-Is-Beautiful-US-Military-Explores-Use-of-Microsatellites-06720/`, May 2016.

[34] Maryland Aerospace Inc., *MAI-400 Datasheet.*

[35] Weston Marlow, Ashley Carlton, Hyosang Yoon, Jared Males, Christian Haughwout, and Kerri Cahoy. *Laser Guidestar Satellite for Ground-based Adaptive Optics Imaging of Geosynchronous Satellites.* Manuscript in preparation.

[36] Weston Marlow et al. *Attitude Determination and Control Approach to Achieve Co-located Microwave Radiometer and GPS Radio Occultation Measurements on a Nanosatellite.* In *Proceedings of the 2015 AAS Guidance, Navigation, and Control (GNC) Conference*, Guidance, Navigation, and Control Conference, Breckenridge, CO, USA, February 2015. AAS.

[37] Paul D McCall. *Modeling, simulation, and characterization of space debris in low-Earth orbit.* 2013.

[38] Henrique M Menegaz, João Y Ishihara, and Geovany A Borges. *A new smallest sigma set for the Unscented Transform and its applications on SLAM.* In *Decision and Control and European Control Conference (CDC-ECC), 2011 50th IEEE Conference on*, pages 3172–3177. IEEE, 2011.

[39] Tam Nguyen and Kerri Cahoy. *Attitude Determination Using Infrared Earth Horizon Sensors.* In *Proceedings of the 28th AIAA/USU Conference on Small Satellites*, Frank J. Redd Student Competition, Logan, Utah, USA, August 2014. AIAA/USU.

[40] Shin-Ichiro Nishida and Satomi Kawamoto. *Strategy for capturing of a tumbling space debris. Acta Astronautica*, 68(1):113–120, 2011.

[41] *NOAA/IAGA, International Geomagnetic Reference Field - 12.*

[42] New Space Systems, *Fine (Digital) Sun Sensor.*

[43] University of Illinois. *University of Illinois Tiny Satellite Initiative: ION Attitude Control System.* `http://cubesat.ece.illinois.edu/Attitude_Control.html`, May 2016.

[44] Massachusetts Institute of Technology. *Exoplanet Space Missions*, 2016.

[45] Massachusetts Institute of Technology. *MIT team selected to participate in AFOSR University Nanosatellite Program 9*, 2016.

[46] Chris Peat. *Heavens Above: ISS Orbit*, 2016.

[47] S Perez, S Jarrix, NJ-H Roche, J Boch, JR Vaillé, A Pénarier, M Saleman, and L Dusseau. *ROBUSTA, a Student Satellite to Serve the Radiation Effects Community.* 2009.

[48] Christopher M. Pong. *High-Precision Pointing and Attitude Estimation and Control Algorithms for Hardware-Constrained Spacecraft.* PhD thesis, Massachusetts Institute of Technology, Department of Aeronautics and Astronautics, June 2014.

[49] Meghan K. Quadrino. *Testing the Attitude Determination and Control of a CubeSat with Hardware-in-the-Loop.* Master's thesis, Massachusetts Institute of Technology, Department of Aeronautics and Astronautics, June 2014.

[50] Samir A Rawashdeh and James E Lumpp Jr. *Aerodynamic Stability for CubeSats at ISS Orbit. Rawashdeh, S., et al*, pages 85–104, 2013.

[51] NASA Press Release. *International Space Station: NanoRacks-Planet Labs-Dove*, 2016.

[52] PNI Sensor Corporation, *RM3000 Geomagnetic Sensor Suite Datasheet.*

[53] Niels Henrik Roth. *Navigation and control design for the CanX-4/-5 satellite formation flying mission.* PhD thesis, 2011.

[54] Nicholas Roy. Classroom notes and lecture handouts. *MIT 16.322 Stochastic Estimation and Control*, 2015.

[55] Francesco Sanfedino, Marco Scardino, Jérémie Chaix, and Stéphanie Lizy-Destrez. Cubesat attitude estimation via aukf using magnetometer measurements and mrps. In *Advances in Aerospace Guidance, Navigation and Control*, pages 343–361. Springer, 2015.

[56] H. Schaub and J. Junkins. *Analytical Mechanics of Space Systems (AIAA Education Series)*. AIAA, 2009.

[57] Sara Seager. *Exoplanets Research.* `http://seagerexoplanets.mit.edu/research.htm`, May 2016.

[58] Advanced Photonics Inc., *Silonex SLSD-71N800 Datasheet.*

[59] D. Simon. *Optimal State Estimation: Kalman, H Infinity, and Nonlinear Approaches.* Wiley, 2006.

[60] Sinclair Interplanetary, *ST-16 Datasheet.*

[61] Sinclair Interplanetary, *Picosatellite Reaction Wheel (RW-0.01) Datasheet.*

[62] J. C. Springmann, A. Bertino-Reibstein, and J. W. Cutler. *Investigation of the on-orbit conjunction between the MCubed and HRBE CubeSats.* In *Aerospace Conference, 2013 IEEE*, pages 1–8, March 2013.

[63] A. Craig Stickler and K.T. Alfriend. *Elementary Magnetic Attitude Control System. Journal of Spacecraft and Rockets*, 13(5):282–287, 1976.

[64] Michael Swartwout. *Saint Louis University CubeSat Database.* `https://sites.google.com/a/slu.edu/swartwout/home/cubesat-database`, March 2016.

[65] California Polytechnic State University. *Dnepr EgyptSat Launch 2006 – CubeSat.* `http://www.cubesat.org/past-launches/2015/6/22/dnepr-launch-1-2006`, May 2016.

[66] *NASA/NOAA. U. S. Standard Atmosphere, 1976.*

[67] Matthew C VanDyke, Jana L Schwartz, and Christopher D Hall. *Unscented Kalman filtering for spacecraft attitude state and parameter estimation. Department of Aerospace & Ocean Engineering, Virginia Polytechnic Institute & State University, Blacksburg, Virginia*, 2004.

[68] Kasper Vinther, Kasper Fuglsang Jensen, Jesper Abildgaard Larsen, and Rafal Wisniewski. *Inexpensive CubeSat attitude estimation using quaternions and unscented Kalman filtering. Automatic Control in Aerospace*, 4(1), 2011.

[69] Ronny Votel and Doug Sinclair. *Comparison of Control Moment Gyros and Reaction Wheels for Small Earth-observing satellites.* In *Proceedings of the 26th AIAA/USU Conference on Small Satellites*, Advanced Technologies III, Logan, Utah, USA, August 2012. AIAA/USU.

[70] James Wells, Luke Stras, and Tiger Jeans. *CanadaâĂŹs smallest satellite: The canadian advanced nanospace experiment (CanX-1).* 2002.

[71] J. R. Wertz. *Spacecraft Attitude Determination and Control.* Astrophysics and Space Science Library. D. Reidel, 1978.

[72] J. R. Wertz and W. J. Larson. *Space Mission Analysis and Design, Third Edition.* Microcosm Press, October 1999.

[73] Evan Wise. *Design, Analysis, and Testing of a Precision Guidance, Navigation, and Control System for a Dual-Spinning CubeSat.* Master's thesis, Massachusetts Institute of Technology, Department of Aeronautics and Astronautics, May 2013.

[74] Evan Wise, Christopher M. Pong, David W. Miller, Tam N. Nguyen, and Kerri Cahoy. *A Dual-Spinning, Three-Axis Stabilized CubeSat for Earth Observations.* In *Proceedings of the 2013 AIAA Guidance, Navigation, and Control (GNC) Conference*, Guidance, Navigation, and Control and Co-located Conferences, Boston, Massachusetts, USA, August 2013. AIAA.

[75] Xuebing Yuan, Shuai Yu, Shengzhi Zhang, Guoping Wang, and Sheng Liu. *Quaternion-based unscented Kalman filter for accurate indoor heading estimation using wearable multi-sensor system. Sensors*, 15(5):10872–10890, 2015.